ICARUS 103, 1–42 (1993)

Near-Infrared Light from Venus' Nightside: A Spectroscopic Analysis

JAMES B. POLLACK,[1] J. BRAD DALTON,[1,3] DAVID GRINSPOON,[1,3] RICHARD B. WATTSON,[4] RICHARD FREEDMAN,[1,5] DAVID CRISP,[6] DAVID A. ALLEN,[7] BRUNO BEZARD,[8] CATHERINE DEBERGH,[8] LAWRENCE P. GIVER,[1] Q. MA,[9] AND RICHARD TIPPING[10]

[1]*NASA Ames Research Center, Moffett Field, California 94035;* [2]*Synernet, Fremont, California 94538;* [3]*University of Colorado, Boulder, Colorado 80309;* [4]*Visidyne, Inc., Burlington, Massachusetts 01803;* [5]*Sterling Inc., Palo Alto, California;* [6]*Jet Propulsion Laboratory, Pasadena, California 91109;* [7]*Anglo-Australian Observatory, Epping, NSW 2121, Australia;* [8]*Observatoire de Paris, 92195, Meudon, France;* [9]*NASA GISS, New York, New York 10025;* [10]*University of Alabama, Tuscaloosa, Alabama 35487*

Received July 27, 1992; revised January 29, 1993

We have simulated near-infrared spectra of the emission from Venus' nightside with a radiative transfer program that allows for emission, absorption, and scattering by atmospheric gases and particles. Except for an O_2 airglow emission band near 1.27 μm, the emission is produced in the hot, lower atmosphere of Venus. Its intensity at the top of the atmosphere is substantially decreased by scattering and absorption within the main clouds and is concentrated within spectral "window" regions where the lower atmosphere is most transparent. The twin goals of this paper are to assess the adequacy of current gas databases for simulating Venus' nightside near-IR spectra and, within these limitations, to derive information on gas abundances below the main clouds and the optical thickness of the main clouds. We used the moderate resolution spectra of Crisp *et al.* (1991) for both these objectives and the very high resolution spectra of Bezard *et al.* (1990) for the first.

The HITRAN database for the permitted transitions of CO_2 is found to be totally inadequate for simulating the near-infrared emission from Venus' nightside. However, much improved simulations can be made when Wattson's high-temperature ("high-T") database of CO_2 is used instead. A major weakness of the current gas databases is the lack of accurate information on CO_2 and H_2O continuum opacity.

Even bright spots on the nightside have substantial cloud-scattering optical depths. We derive cloud optical depths of about 25 at a reference wavelength of 0.63 μm by fitting spectra of three different spots. We find that the H_2O mixing ratio has a constant value of 30 ± 10 ppm in the altitude range from 10 to 40 km. We also infer mixing ratios for SO_2 of 180 ± 70 ppm at 42 km, HCl of 0.48 ± 0.12 ppm at 23.5 km, HF of 1–5 ppb at 33.5 km, and upper limits on the mixing ratio of CH_4 of 0.1 ppm at 30 km and 2 ppm at 24 km.

We show that it is possible to infer both the mixing ratios of some gas species and their vertical gradients at the centroid of emission in a given spectral window. In particular, we find that OCS has a mixing ratio, α, of 4.4 ± 1.0 ppm and a gradient, $d\alpha/dz$, of −1.58 ± 0.30 ppm/km at an altitude of 33 km; i.e., the OCS mixing ratio strongly increases with decreasing altitude. In addition, we find that the corresponding values for CO are 23 ± 5 ppm and +1.20 ± 0.45 ppm/km at an altitude of 36 km. Therefore, within a factor of 2 CO is decreasing toward the surface at the same rate as that at which OCS is increasing. These results are in good agreement with theories of lithospheric buffering and gas thermodynamic equilibrium at the surface that predict a substantial abundance of OCS (several 10s of ppm) at the surface due to reactions in which CO is one of the reactants.

I. INTRODUCTION

Near-infrared observations of the nightside of Venus by Allen and Crawford (1984) opened a new window into Venus' atmosphere. They detected a surprising amount of radiation in two spectral regions: a narrow band centered at 1.74 μm and a broad band centered at 2.3 μm. Furthermore, this nightside radiation was found to be spatially variable, with the nightside features rotating somewhat more slowly than the UV markings seen on the dayside (Allen and Crawford 1984).

It was quickly realized that these near-infrared emissions were due to thermal radiation, rather than sunlight scattered from the dayside. In particular, Allen (1987) showed that the lack of a systematic variation of the nightside emission with distance from the terminator and the absence of polarization strongly favored a thermal source for this radiation. Furthermore, the ability of radiative transfer models of nightside thermal emission to reproduce approximately the observed spectra provides nearly conclusive evidence in favor of this mechanism (Kamp *et al.* 1988, Kamp and Taylor 1990, Bezard *et al.* 1990, Bell *et al.* 1991, Crisp *et al.* 1991a, Carlson *et al.* 1991). However, there is one interesting exception to the dominance of thermal emission from the hot, lower atmo-

0019-1035/93 $5.00

sphere of Venus: A high-altitude O_2 airglow emission band that strangely varies with time and location contributes to the radiation seen in the newly discovered 1.27-μm window (Crisp *et al.* 1991a, Allen *et al.* 1992, B. Bezard *et al.*, in preparation).

Kamp *et al.* (1988) were the first to point out that the spatial variability of the nightside thermal emission was due to spatial variations in the optical depth of the ubiquitous sulfuric acid clouds. This conclusion was based on the observation of Allen (1987) that the spectra of bright and dark regions in the 2.3-μm band differed by an almost wavelength-independent scale factor. By way of contrast, horizontal variations in the abundances of gases, such as H_2O, would produce sizable spectral variations in the contrast of features in this window (Kamp *et al.* 1988, Bell *et al.* 1991). A much larger body of data, including observations conducted by the NIMS instrument on the Galileo spacecraft (Carlson *et al.* 1991) shows essentially the same lack of spectral dependence of feature contrasts within a given window region, with one notable exception. Bell *et al.* (1991) detected a sharp change in the contrast of two features near a wavelength of 2.3 μm. They showed that the observed spectral variation of contrast closely matched that expected from models in which both the cloud optical depth and the water abundance varied between the two locales. Water vapor mixing ratios that differed by about a factor of 5 at altitudes below 40 km were required to match these singular observations. Confirmation of this finding is highly desirable.

There is good evidence that the spatial modulations in cloud optical depth are occurring only in the bottom portion of the main cloud deck. First, the zonal wind speeds of the near-IR features, when compared to the zonal wind profile derived from probe data, imply that the centroid of the changes is located in the middle (50–57 km) or lower (48–50 km) cloud regions (Crisp *et al.* 1989, 1991b, Carlson *et al.* 1991). Second, the almost total absence of spatial variability at wavelengths longward of 2.5 μm strongly indicates that the variability is confined to the bottom few kilometers of the main cloud deck (Carlson *et al.* 1991): At wavelengths longward of 2.5 μm, the single scattering albedo of the cloud particles is low and hence radiation emitted to space originates near the cloud tops.

Kamp *et al.* (1988) showed that two conditions must be fulfilled to produce a window region in which a detectable amount of radiation from the lower atmosphere is emitted to space from Venus' nightside: First, the atmospheric gases must absorb sufficiently weakly so that unit optical depth occurs at an altitude below the base of the main cloud deck (48 km). This condition becomes increasingly stringent (a lower altitude for unit optical depth) with decreasing wavelength in the near-infrared, since these wavelengths are on the Wein side of the blackbody function. Fortunately, absorption by atmospheric gases becomes progressively weaker toward shorter wavelengths in the near-infrared. This opacity constraint applies primarily to CO_2, the dominant constituent of Venus' lower atmosphere. Thus, windows can exist only between the stronger bands of CO_2. To a more limited extent, this constraint is also on H_2O, which has a number of relatively strong bands in the near-infrared.

The second condition for the occurrence of a near-infrared window is that the cloud particles be very poor absorbers of the thermal radiation incident at the base of the main cloud deck. Thus, the cloud particles must have a single scattering albedo close to unity. Scattering is far less effective than absorption in reducing the transmission of an optically thick cloud. This condition is met at all wavelengths shortward of 2.5 μm, but is not realized at any longer wavelength. The clouds do not become partially transparent again until millimeter wavelengths. Transparency at millimeter wavelengths is due primarily to the optical depth of the clouds becoming much smaller than their value at visible and near-infrared wavelengths because the particle size is much smaller than millimeter wavelengths.

In addition to the two window regions discovered by Allen and Crawford (1984), a number of other windows, at shorter wavelengths, are now known to exist. Allen (1990) detected narrow windows at 1.10, 1.18, 1.27, and 1.31 μm, and the Galileo NIMS experiment detected these new windows as well as one at 1.01 μm (Carlson *et al.* 1991). Below, we often refer to these new windows as the "1.2-μm window complex" or simply the "1.2-μm windows."

Much can be learned about the composition of the lower atmosphere of Venus, the radiative properties of its clouds, and winds near the bottom portion of the main cloud deck from spectral and spatial observations of the near infrared nightside thermal radiation and their analyses. In particular, absorption features due to CO, H_2O, HDO, HCl, HF, and OCS have been detected in nightside near-infrared spectra and estimates of their mixing ratios have been derived from these data (Kamp and Taylor 1990, Bezard *et al.* 1990, deBergh *et al.* 1991, Crisp *et al.* 1991a, Carlson *et al.* 1991). The magnitude of the observed continuum intensity and its spatial variability in the window regions has been used to estimate the cloud optical depth and its spatial variability (Kamp and Taylor 1990, Crisp *et al.* 1991a, Carlson *et al.* 1991). Finally, zonal and meridional wind speeds have been estimated by tracking near-infrared features (Crisp *et al.* 1989, 1991b, Carlson *et al.* 1991).

Radiative transfer models provide the basic means for analyzing near-infrared spectra of Venus' nightside and deriving estimates of gas abundances and cloud properties. Unfortunately, the accuracy of these retrievals have

been greatly limited by the lack of information about the absorption properties of gases at the high temperature and pressure conditions in Venus' lower atmosphere. In their pioneering simulations of these spectra, Kamp *et al.* (1988) and Kamp and Taylor (1990) used the HITRAN gas line database, which was designed for simulating the comparatively low-temperature and -pressure environment of the Earth's atmosphere (Rothman *et al.* 1987). They were able to achieve only crude agreement with Allen's (1987) spectra of the 1.7- and 2.3-μm windows and only then by making ad hoc assumptions about the strengths of weak CO_2 bands and the shape of the far wings of lines in strong CO_2 bands.

A much better fit to very high resolution ($\approx$0.3 cm^{-1}) spectra of the 1.7- and 2.3-μm windows was achieved by Bezard *et al.* (1990) and deBergh *et al.* (1991). They did so by supplementing the HITRAN database with information about a limited number of hotbands given by Rothman (1986), by extending the bands in the augmented compilation to higher rotational quantum numbers and by postulating the presence of continuum opacity in both spectral regions that had a simple dependence on wavenumber. However, recent laboratory measurements by Giver *et al.* (1991a,b) show that there are significant errors in the strengths of at least two of the bands contained in Rothman (1986) and used by Bezard *et al.* (1990), including a prominent band in the Venus spectra centered at 4416 cm^{-1}. Finally, approximate fits to the newly discovered features near 1.2 μm have been achieved only by using the properties of numerous CO_2 hot bands derived from the DND (direct numerical diagonalization) theory of Wattson (Crisp *et al.* 1991a, Carlson *et al.* 1991).

A key goal of this paper is to define the major sources of opacity in Venus' lower atmosphere that control the location and shape of the major near-infrared windows. Our focus is on various types of gaseous opacity, but we also investigate the way in which the main cloud deck affects the radiation reaching the top of the atmosphere. We approach this problem in several different ways. First, we assess the maturity and importance of various databases that define the absorption properties of gases. In so doing, we introduce an improved database for the permitted transitions of CO_2, a preliminary database for the permitted transitions of H_2O at high temperatures, and a calculation of the water vapor continuum at the high wavenumbers of interest. Second, we use these databases to identify features seen in near-infrared spectra of Venus' nightside and bands that help to control the spectral appearance of the windows. Finally, we use the best available opacity information to simulate two sets of groundbased observations, both to assess the adequacy of the opacity information and to derive estimates of gas abundances in the lowest several 10s of kilometers of Venus' atmosphere and radiative properties of the clouds.

2. GAS OPACITY

2.1. Overview

In this section, we discuss various types of gaseous opacity that are potentially relevant to the near-infrared windows of Venus' nightside. In so doing, we assess the adequacy and accuracy of currently available information provided by laboratory measurements and theory. In some cases, we also determine the importance of particular sources of opacity for the problem of interest.

It is useful to subdivide gaseous opacity into two basic categories: permitted transitions and continuum opacity. Permitted transitions are ones in which the dipole moment (or higher moment) of an isolated molecule changes between the lower and upper energy levels characterizing a given transition. This permits an isolated molecule to absorb or emit electromagnetic radiation having an energy equal to the difference in the energies of the upper and lower levels. For example, the asymmetric stretch and bending vibrational fundamentals of CO_2 meet this criterion, but the symmetric stretch fundamental of its main isotope does not. At the near-infrared wavenumbers of interest, all the permitted transitions result from overtone and combination vibrational bands that also include numerous rotational transitions.

Continuum opacity refers to transitions that occur as a result of a dipole (or higher) moment induced in an absorbing molecule as a result of the interaction between it and a nearby second molecule. In contrast to the large amplitude variations in absorption coefficient with wavenumber that characterize permitted transitions close to line centers, continuum absorption varies smoothly with wavenumbers. Continuum opacity is proportional to the product of the densities of the absorbing and colliding molecules at the densities of interest; i.e., only binary collisions need to be considered. For reasons to be discussed shortly, we also include the opacity arising from the far wings of strong bands in the category of continuum opacity. Here, we simply note that far wing opacity has the same dependence on density that collision-induced opacity does and, so, it is often difficult to separate these two types of continuum opacity in laboratory experiments.

Line compendia or databases, such as HITRAN, contain lists of the positions, strengths, energies of the initial states, pressure half-widths at standard conditions (296 K, 1 bar), and the temperature dependences of the half-widths of permitted transitions of various gases. For the vibrational/rotational transitions of interest, the databases often contain all of the individual lines instead of the band properties. Monochromatic opacities produced by each line may be derived from this information once the strengths have been adjusted to the temperatures of interest (by use of Boltzmann factors and partition func-

tions), the pressure half-widths have been adjusted to the temperatures and pressures of interest (see below), and an expression has been chosen for the line shape.

Close to line centers (usually within a few cm^{-1}), a Voigt line profile provides an excellent approximation to the true line profile (Goody and Yung 1989). This profile allows for both doppler and pressure broadening. In the lower atmosphere of Venus, pressure broadening dominates the line profiles and, in this case, the Voigt profile reduces to a Lorentz profile. However, far from the line center, essentially all line profiles display marked deviations from a Lorentzian behavior. Typically, CO_2 displays a sub-Lorentzian behavior (the opacity far from the line center is less than that predicted by a Lorentz profile), whereas H_2O shows a super-Lorentzian behavior (Goody and Yung 1989). In the far wings, it has been common practice to model the line shape as consisting of the product of the Lorentz profile and a function (χ) of the difference between the wavenumbers of the line center and position of interest (Burch *et al.* 1969). This function can be expected to vary with temperature and be different for different pairs of colliding molecules. In addition, it apparently varies with vibrational quantum number, at least for CO_2 (Burch *et al.* 1969). Unfortunately, χ has been measured only for a limited number of bands (usually some of the fundamentals) of a limited number of molecules.

In our calculations, we use a sub-Lorentzian profile for CO_2 that was derived by one of us (B.B.) by fitting analytic functions to the χ factor derived by Burch *et al.* (1969) for the high-wavenumber wing of the 2.7-μm band at room temperature. In particular, we used the following formulae for χ for an absorbing CO_2 molecule being pressure broadened by a second CO_2 molecule,

$$\chi = 1, \quad \delta\nu < 3\ \mathrm{cm}^{-1} \tag{1}$$

$$\chi = 1.35\exp(-\delta\nu/10), \quad 3\ \mathrm{cm}^{-1} \le \delta\nu < 10\ \mathrm{cm}^{-1} \tag{2}$$

$$\chi = 0.614\exp(-\delta\nu/47), \quad 10\ \mathrm{cm}^{-1} \le \delta\nu < 120\ \mathrm{cm}^{-1} \tag{3}$$

$$\chi = 0, \quad 120\ \mathrm{cm}^{-1} \le \delta\nu, \tag{4}$$

where $\delta\nu$ is the absolute value of the distance in wavenumbers from the line center. χ is set equal to 0 at wavenumbers in excess of 120 cm^{-1} because weak transitions of CO_2 interfere with the ability to measure the shape of the far wings of the strong band at 2.7 μm and because the use of this cutoff has little practical effect on our synthetic spectra at almost all wavenumbers of interest. An exception to this latter statement occurs in the 1.18-μm window. As discussed later in this paper, we both extended the wavenumber domain for the third of the χ expressions and used a different constant in the exponent to obtain a satisfactory fit to the data here. This adjustment illustrates an important unresolved problem for the χ factors associated with CO_2: How do they vary with the wavenumber of the band?

The data of Burch *et al.* (1969) suggest that the far wings of CO_2 lines become progressively less sub-Lorentzian with increasing wavenumber of the band. In the calculations below, we used the χ factor derived from the 2.7-μm region for the 1.7- and 2.3-μm windows and an adjusted, less sub-Lorentzian one for the 1.2-μm window complex. We did not allow for a possible variation of χ with temperature. Fortunately, the uncertainty in the choice of the χ factor has little influence on our results, except in a few isolated spectral positions, where a strong band lies adjacent to a region where the bands are several orders of magnitude weaker. This general insensitivity is indicated by our obtaining essentially the same monochromatic absorption coefficients for CO_2 in almost all locations when the cutoff was altered from 120 to 25 cm^{-1}. However, far-wing opacity beyond 120 cm^{-1} from lines of strong CO_2 bands that are adjacent to window regions can still be an important source of absorption. It is treated here as "continuum" opacity (see Section 2.3). Finally, we note that the χ factor for CO_2 that is contained in the Air Force Geophysical Laboratory's (AFGL) FASCODE program is one relevant for CO_2 being broadened by N_2 and it differs substantially from the factor appropriate for CO_2 being broadened by CO_2.

For all other molecules, we use a Lorentz line profile with a 25-cm^{-1} cutoff. We do this both because there is a lack of information on the shape of the far wings of lines other than CO_2 when CO_2 is the broadening gas and because these molecules have an abundance in Venus' atmosphere that is much less than that of CO_2.

There is another spectroscopy issue, that of line mixing, that we ignore in the calculations of this paper for lack of pertinent information. Line mixing refers to the tendency of rotational lines that lie sufficiently close together to have wave functions at elevated pressures that are linear combinations of those of its nearest neighbors and its own wave function at much lower pressures (Levy *et al.* 1992). The practical effect of line mixing is to alter line intensities from the values that hold at much lower pressure. At ambient pressure, line mixing is important only in Q branches. However, it could also become important in the R and P branches at the substantially elevated pressures of the lower atmosphere of Venus. Based on our ability to obtain fairly exact fits to moderate and high-resolution spectra of the 2.3- and 1.7-μm windows, we suspect that line mixing is not a serious problem for these windows. Whether it is for the 1.2-μm window complex is still very much an open issue.

The half-width of a line depends on pressure, temperature, the identity of both members of the colliding pair of molecules, and the quantum numbers of the transition.

At a fixed temperature, it varies linearly with pressure. Its dependence on temperature, at a fixed pressure, is often represented as a power law. In practice, the power law exponent varies somewhat with quantum number. In the case of linear molecules, such as CO_2 and CO, the half-width depends mainly on a single rotational quantum number, J. But, in the case of nonlinear molecules, such as H_2O, it depends on several rotational quantum numbers. In our calculations, we allowed for this dependence for linear molecules only. The identity of the broadening molecule has an influence on the half-width. For example, the half-widths of lines being broadened by CO_2 are typically several 10s of percent larger than the half-widths due to broadening by terrestrial air (Howard *et al.* 1956). In our calculations, we allow for this effect by either incorporating laboratory measurements of half-widths for CO_2 broadening (CO_2, CO, HCl, HF) (Nakazawa and Tanaka 1982, Toth and Darnton 1974, Howard *et al.* 1956, Shaw and Lovell 1969) or multiplying the half-widths of air broadening by an appropriate constant factor (1.3 for H_2O; Howard *et al.* 1956).

In the remainder of this section, we discuss the status and appropriateness for Venus of several databases of permitted transitions and several sources of continuum opacity. At this point, we simply note that both laboratory and theoretical approaches have proved to be useful for our purposes.

2.2. Databases for Permitted Transitions

Below, we briefly describe various databases, including HITRAN and a number of high-temperature ones. In all cases, they have been derived from a combination of laboratory measurements and quantum mechanical calculations. The latter have focused on determining line positions, strengths, and energy levels. Information about pressure half-widths is still best derived from laboratory data alone.

HITRAN. The HITRAN database is an excellent compendium of line information for a large number of molecules (Rothman *et al.* 1987, 1992). This database was constructed from a judicious blend of laboratory data and theory. As mentioned in the introduction, it was designed for conditions in the Earth's atmosphere and, so, needs to be used with caution when applying its results to another planet, especially Venus. Its customization for the Earth's atmosphere affects its contents in several ways. First, a line strength cutoff criterion is used to exclude lines of a given gas species that would not produce measurable opacity in the Earth's atmosphere. Thus, the HITRAN database may not include high rotational lines, hot bands, and even weak ground-state transitions that could produce substantial opacity for the gas abundances and high-pressure and -temperature conditions in Venus' atmosphere. Second, line half-widths are given for foreign broadening by terrestrial air and, in some cases, for self-broadening, but not for broadening by CO_2 (except for bands of CO_2).

The 1986 version of HITRAN (Rothman *et al.*, 1987) was supplemented in the case of CO_2 by a more complete listing of bands in Rothman (1986). Unfortunately, the information given for some of the weaker bands that were not included in HITRAN 1986 was based on inaccurate, theoretical extrapolations of stronger bands that were measured in the laboratory. For example, Giver and Chackerian (1991a) have obtained the first accurate laboratory measurement of the 4416-cm^{-1} band of CO_2 and find that the band strength is about 35% smaller than the value given in Rothman (1986). This band is very prominent in spectra of Venus' nightside emission (Bezard *et al.*, 1990). Giver and Chackerian (1991b) also measured the strength of the 4591-cm^{-1} band and found that it was about 50% larger than the value given in Rothman (1986).

For the Venus problem of interest, there is not a significant difference in the CO_2 line information contained on the 1991 and 1986 versions of HITRAN; i.e., the monochromatic opacities of CO_2 near optical depth unity in the various window regions are essentially the same for these two versions. As shown below, these opacities are totally inadequate for simulating well the observed spectra of the window regions. However, the 1991 HITRAN database contains a number of improvements over the earlier version, including a better definition of the line properties of H_2O, which is based on recent laboratory measurements. We use the new H_2O values in our "standard" database for modeling the Venus spectra. We also use the 1991 HITRAN database to obtain line information for CH_4 in the 1.7- and 2.3-μm windows. Unfortunately, neither this database nor any other that we are aware of contains line information for CH_4 in the 1.2-μm window complex, where it also has strong bands.

High-temperature CO_2 database. A high-temperature CO_2 database has been constructed by using DND theory (Wattson and Rothman 1986, 1992, Esplin *et al.* 1989). The basic functions of this theory are constrained to agree, in a least squares sense, with accurate laboratory measurements of the line positions and strengths of ground-state transitions of the main isotope. Following the procedure described Appendix A, it is then possible to predict the line properties of hotbands, bands of the other isotopes, and weak, ground-state transitions of the main isotope.

The current version of the high-temperature CO_2 database, which we use here, contains line information for the three most abundant isotopes of CO_2, as well as for the 638 isotope. The terminology 638 refers to CO_2 molecules containing oxygen 16 and 18 and carbon 13. The lines of

these four isotopes encompass essentially all the lines that produce significant opacity in Venus' near-IR window regions. This "high-T" database includes all lines of these isotopes that satisfy a very conservative line cutoff criterion for Venus. The line cutoff occurs at a strength of 1×10^{-30} cm^{-1}/(molecule-cm^{-2}) at 750 K, which is equivalent to an optical depth of about 10^{-3} for a vertical path from the top to the bottom of Venus' atmosphere.

The high-T database covers the 500–12,500-cm^{-1} domain. It contains approximately 7.2×10^6 lines that are members of about 6×10^4 vibrational bands. By way of contrast, HITRAN '86 and '91 include only about 6×10^4 lines of CO_2 that belong to about 6×10^2 bands. More precisely, HITRAN includes only two bands in the 2.3-μm window (626 bands at 4005.9 and 4416.1 cm^{-1}, where 626 refers to the main CO_2 isotope), only two bands in the 1.7-μm window (a 626 hot band at 5687.1 cm^{-1} and a 628 band at 5858.0 cm^{-1}), and nine bands in the multiple window region from 1.05 to 1.35 μm. However the high-T database lists many dozens of bands in each of these spectral intervals. Also, Giver and Chackerian's (1991a) measurement of the 4416.1-cm^{-1} band was included in the DND fitting procedure. Thus, the intensities of the lines of this band on the high-T database are much more accurate than their counterparts on HITRAN '86 and '91. The strength of the 4591-cm^{-1} band on the high-T database lies much closer to Giver and Chackerian's (1991b) lab result than that contained on HITRAN. Thus, the associated hotbands of 4591 cm^{-1}, many of which lie within the 2.3-μm window, should be fairly accurate on the high-T database.

Extensive comparisons have been made between the line positions and line intensities given by the high-temperature database and all the values given by laboratory measurements that were *not* used in the fitting protocol. In virtually every case, the predicted and measured line positions were found to agree to better than 0.1 cm^{-1} (typically, they agreed to within a few hundredths of a wavenumber). The predicted and measured line intensities agreed to about 10% for ground-state transitions and to about 20% for hot bands. The positional accuracy is on the order of 10^{-2} to 10^{-1} line half-widths at optical depth unity in the various window regions and, thus, will lead to negligible errors in spectral syntheses of the window regions. The intensity errors are somewhat larger than one would like. They can be reduced substantially in the near future, as discussed near the end of Appendix A.

Figures 1a, 1b, and 1c show comparisons between monochromatic absorption coefficients of CO_2 derived from the high-T and HITRAN databases in the various near-IR window regions of Venus' atmosphere. In each case, these coefficients have been evaluated at a temperature and pressure that lies close to optical depth unity in the window. The horizontal line shows the approximate value of the absorption coefficient, k, needed to produce unit optical depth at the selected pressure/temperature level. This coefficient was found from the following equation

$$k = [\mu g]/[10^6 \mathrm{Av} \alpha_c P] \quad (5)$$

where μ is the mean molecular weight, g is the acceleration of gravity, Av is Avogadro's number, α_c is the CO_2 mixing ratio, and P is the pressure at the effective emitting level. Here, as elsewhere, we set P equal to 10, 20, and 40 atm, respectively, for the 2.3-, 1.7-, and 1.2-μm windows (e.g., Crisp *et al.* 1991a). In deriving the above equation, we used the perfect gas law and the hydrostatic equilibrium equation. All variables have cgs units, except for pressure, which has units of bars. We measure k in units of cm^2/molecule.

Quite clearly, the two sets of coefficients differ very substantially in all the window regions. Therefore, it is essential to use the more complete high-T database of CO_2 for accurate simulations of Venus' nightside thermal emission. Comparing the horizontal lines with the absorption coefficients from the high-T database, we see that the permitted transitions of CO_2 produce significant opacity throughout each of the window regions.

In Figs. 2a, 2b, and 2c, we compare the monochromatic absorption coefficients derived from the high-T database at room temperature and the elevated temperatures near optical depth unity in the various window regions. In both cases, pressures near optical depth unity were employed. The difference between the two sets of curves provides a measure of the importance of hot bands. According to Figs. 2a–2c, substantial differences in spectral shape and absolute level exist between the two sets of curves, and, hence, hotbands of CO_2 play an important role in shaping the windows.

High-temperature H_2O database. Wattson (1991) used DND theory to construct a preliminary high-temperature database for H_2O. Some details of his procedure are given in Appendix A. The resulting hot-water database consists of approximately 150,000 lines for the principal isotopic species. It augments the approximately 50,000 H_2O lines contained on HITRAN by including those with higher rotational quantum numbers (up to $J = 23$), those originating from hot bands that are weak at room temperature, and those from weak ground state transitions. The intensity cutoff criterion was 10^{-25} cm^{-1}/(molecule-cm^{-2}) at 750 K, which is equivalent to an optical depth of about 10^{-2} from the top to the bottom of Venus' atmosphere.

Comparison of water lines present on both the hot-water and HITRAN databases indicated that line positions on the former had errors on the order of several

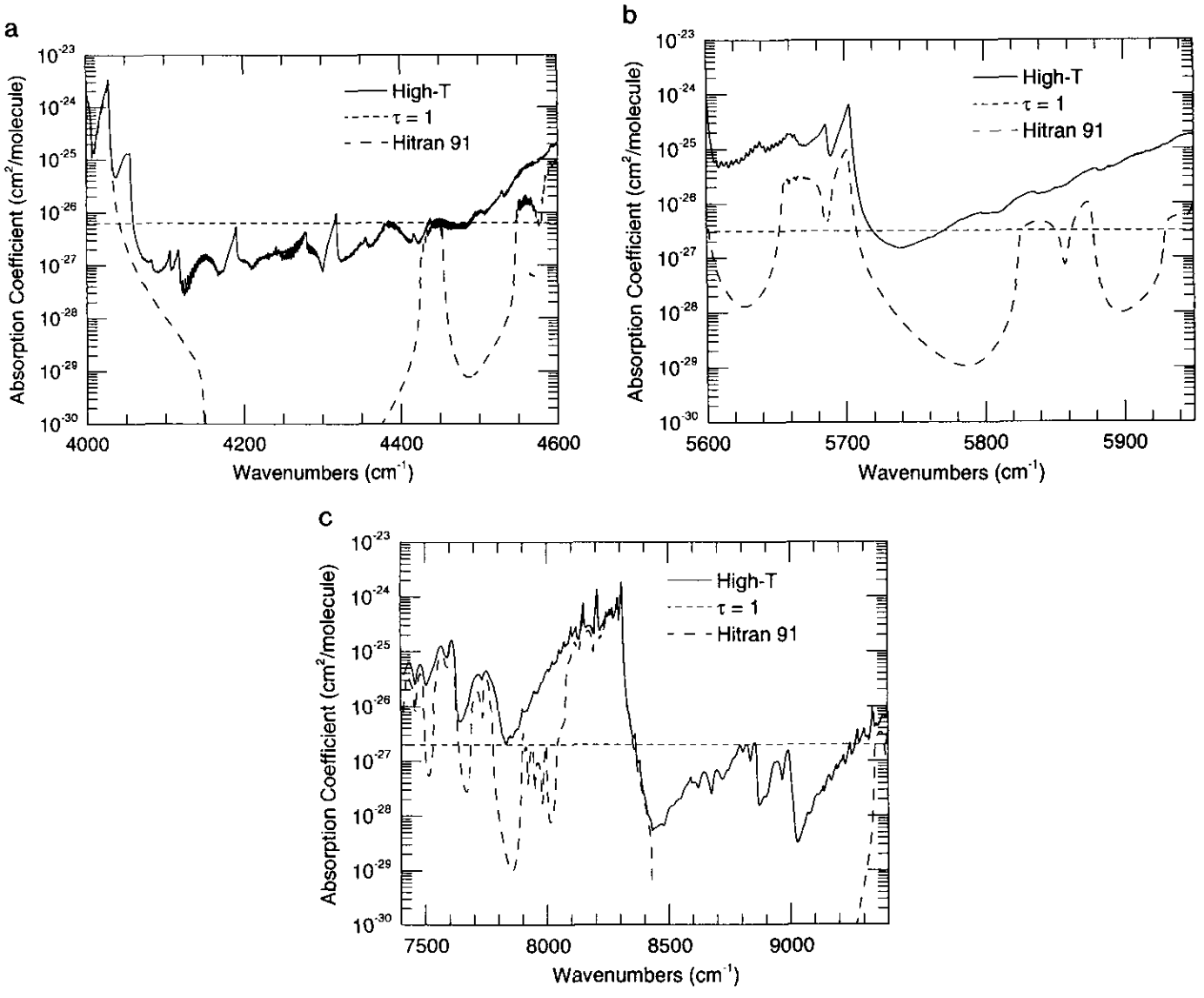

FIG. 1. A comparison of the monochromatic absorption coefficients of CO_2 generated from the HITRAN '91 database (dashed curve) and the high-T database of Wattson (thin solid line) for pressure (P) and temperature (T) conditions appropriate to the various window regions. The horizontal, thick solid line shows the absorption coefficient needed to produce unit opacity above the mean effective emission level for the various windows. (a) 2.3-μm window: P = 10 bars; T = 500 K. (b) 1.7-μm window: P = 20 bars; T = 575 K. (c) 1.2-μm window complex: P = 40 bars; T = 640 K.

wavenumbers. Similarly, intensity errors were found to be generally in the range of 20% for symmetric top-allowed lines and to be as large as a factor of 2 or more for the weaker, symmetric top-forbidden lines. In view of the preliminary nature of this database, we do not use it in our standard Venus database; we use it only to assess in which window regions the hot bands of water have an important impact on the Venus spectra.

CO and halide high-T database. Tipping (1990) has constructed a high-temperature database for CO and the hydrogen halides (HF, HCl, HBr, and HI) by using quantum mechanical theory for diatomic molecules and constraining his basic functions to agree with relevant laboratory data. The details of his procedure are summarized in Appendix B. Line positions are accurate to about 0.001 cm^{-1} in Tipping's databases. Line strengths are accurate to about 5% for fundamental transitions and about 10% for the overtone and hot band transitions. These latter transitions fall within the spectral domain of interest.

For CO, the high-T database contains information for

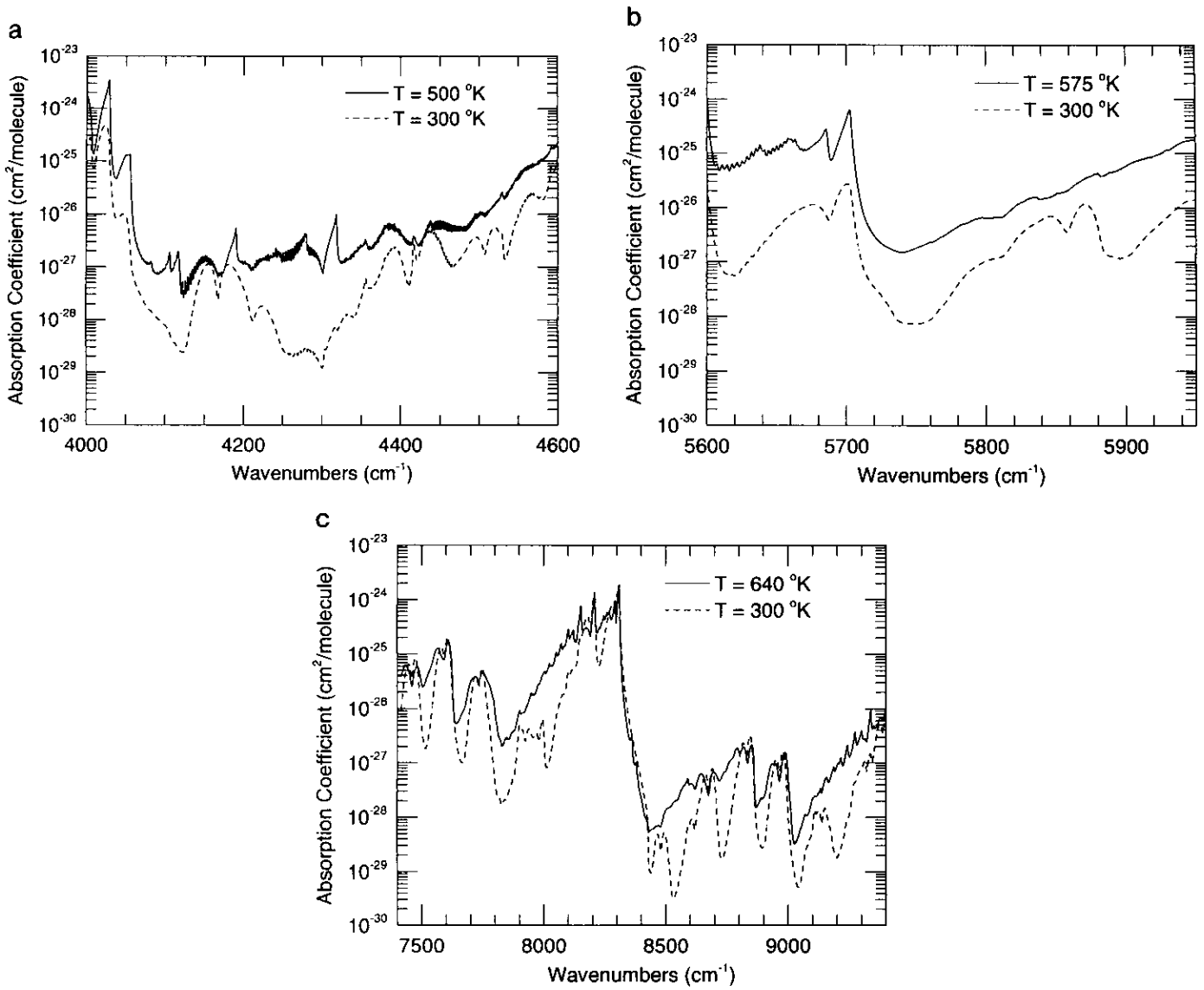

FIG. 2. A comparison of the monochromatic opacities of CO_2 generated with the high-T database for pressure conditions appropriate to the various window regions and alternately room temperature (dashed curve) and a temperature appropriate to the windows (see Fig. 1). (a) 2.3-μm window; (b) 1.7-μm window; (c) 1.2-μm window complex.

the five most abundant isotopes for rotational quantum numbers, J, from 0 to 50 and initial and final vibrational quantum numbers, v, up to 1 and 4, respectively. In addition, a more extensive set of rotational and vibrational quantum numbers is included for the two most abundant isotopes (Tipping, 1990). For the hydrogen halides, an intensity cutoff of 1×10^{-26} cm^{-1}/(molecule-cm^2) at room temperature was used to define the J and v values of the transitions included in the database. Only the main isotope of HF and HI is included, whereas the two most abundant isotopes of HCl and HBr are included in the high-T database.

OCS and SO_2. The $2\nu_3$ overtone band of OCS appears to be responsible for a feature centered near 4095 cm^{-1} (2.44 μm) in the high-resolution spectrum of Bezard *et al.* (1990), whereas the $3\nu_3$ overtone band of SO_2 is a candidate for producing a feature near 4055 cm^{-1} (2.46 μm) in the same spectrum. Neither of these bands is contained on the HITRAN '91 database. Here, we make use of laboratory measurements to define the line parameters of these bands for use in our simulations. We note that, unfortunately, no measurements have been made so far at higher wavenumbers for either of these molecules.

We followed the approach of Bezard *et al.* (1990) to obtain the relevant line parameters of OCS. In particular, we used the calculations of Fayt (1970) and Fayt *et al.*

(1986) to derive line positions and lower state energies, and we used the measurement by Kagann (1982) of the combined band strength of the $2\nu_3$ overtone and its closely situated hot bands to derive line intensities. We derived line parameters for the overtone band at 4101.4 cm^{-1} and the hot bands at 4072.1, 4073.9, 4086.7, and 4094.9 cm^{-1}.

In deriving band strengths for the bands of interest from the measurements of Kagann (1982), we assumed that the ratio of their strengths simply equalled the ratio of the Boltzmann factors of the vibrational energies of their lower states. In this way, we obtained band strengths at a temperature of 296 K. Using this information, in conjunction with appropriate Boltzmann factors, statistical weights, and partition functions, we derived line strengths for the above five bands of OCS for lines whose strength exceeded 5×10^{-23} cm^{-1}/(molecule-cm^{-2}) at 500 K. Lines of this strength produce unit optical depth within a half-width of their centers above the 500 K, 10-bar level when the OCS mixing ratio equals approximately 6.5×10^{-5}.

Line parameters for the $3\nu_3$ overtone band of SO_2 at 4054 cm^{-1} were derived from the analysis of recent laboratory measurements by Lafferty *et al.* (1992). High-resolution spectra (3×10^{-5} cm^{-1}) of this band were made by A. Pine at the National Institute of Standards and Technology with a tunable difference-frequency laser. A standard symmetric top formalism (Watson 1967) was used to derive line strengths and positions. The weak-line cufoff was set to 3×10^{-27} cm^{-1}/(molecule-cm^{-2}).

2.3. Continuum Opacity

H_2O continuum. It has been known for a long time from observations of the Earth's atmosphere (e.g., Elsasser 1938) and laboratory measurements (e.g., Burch and Gryvnak, 1978) that water vapor has continuum opacity in the 300–1100-cm^{-1} spectral region. It is characterized by a quadratic dependence on density and a strongly negative dependence on temperature. Possible mechanisms for producing this continuum have included water dimers, collision-induced transitions, and the superposition of the far wings of collisionally broadened lines, especially those of the pure rotational transitions. Very likely, all three mechanisms contribute to continuum opacity; however, many spectroscopists consider the third mechanism to be the dominant one.

Strong support for the above conclusion is given by the ability of recent quantum mechanical calculations of the opacity due to the far wings of pressure-broadened lines to reproduce the measured magnitude, spectral shape, and temperature dependence of the water vapor continuum in the 300–1100-cm^{-1} region (Rosenkranz 1985, 1987, Ma and Tipping 1990, 1991). In the latest set of calculations, the maximum difference between the measured and theoretical water vapor continuum is less than 30% (Ma and Tipping, 1991).

The current formulation of this theory by Ma and Tipping (1992a,b) makes it possible to estimate the water vapor continuum at the high wavenumbers of interest to this paper. This continuum results from the far wings of rotational lines that belong to strong H_2O vibrational bands situated close to the window regions of Venus. Unfortunately, the calculated continuum opacities may be in error by as much as one order of magnitude in the spectral region of interest. Therefore, we did not include them in the standard opacity database, but rather we performed sensitivity studies of their impact on our results.

Figures 3a and 3b show estimates of the water vapor continuum in the 4000–10,000-cm^{-1} region, as obtained from the formalism of Ma and Tipping (1992a,b). Figure 3a shows results for continuum opacity that arises from collisions of the absorbing H_2O molecule with another H_2O molecule, whereas Fig. 3b shows that due to collisions of the H_2O absorber with a CO_2 molecule. Appendix C summarizes aspects of the calculations used to produce Figs. 3a and 3b, including the key assumptions and certain parameter choices. According to these figures, only H_2O–CO_2 continuum opacity needs to be considered for Venus' lower atmosphere, given the low H_2O mixing ratios (10–100 ppm) there.

CO_2 continuum. Laboratory measurements of CO_2 absorption at pressures of several 10s of bars show that it exhibits cointinuum absorption in the 4100–4500-cm^{-1} region (Moore 1971, Moskalenko *et al.* 1979, Brodbeck *et al.* 1991). This conclusion is based on the absorption coefficient, a, being proportional to the square of the CO_2 density, ρ_c. This continuum opacity is produced by both the far wings of strong CO_2 bands located near 3700 and 5000 cm^{-1} and pressure-induced bands that occur within the 4100–4500-cm^{-1} region. Collectively, these two sources of continuum opacity produce a fairly flat binary absorption coefficient, α_{11}, throughout the 4100–4500-cm^{-1} region, where $\alpha_{11} = a/\rho^2$ (Moore 1971, Moskalenko *et al.* 1979, Brodbeck *et al.* 1991).

Unfortunately, measurements of CO_2 continuum absorption within the 4100–4500-cm^{-1} region have been made almost exclusively at room temperature. Furthermore, there is a puzzling factor of 7 discrepancy between the values of α_{11} obtained by Moore (1971) on the one hand and those found by Brodbeck *et al.* (1991) and Moskalenko *et al.* (1979) on the other hand at room temperature. Therefore, we assume in our simulations that α_{11} has a wavenumber-independent value within the 2.3-μm window and determine its value from the Venus spectra. The same assumption and approach was used by Bezard *et al.* (1990). Lacking measurements of the CO_2 continuum within the shorter wavelength windows, we introduced a wavenumber-independent continuum coef-

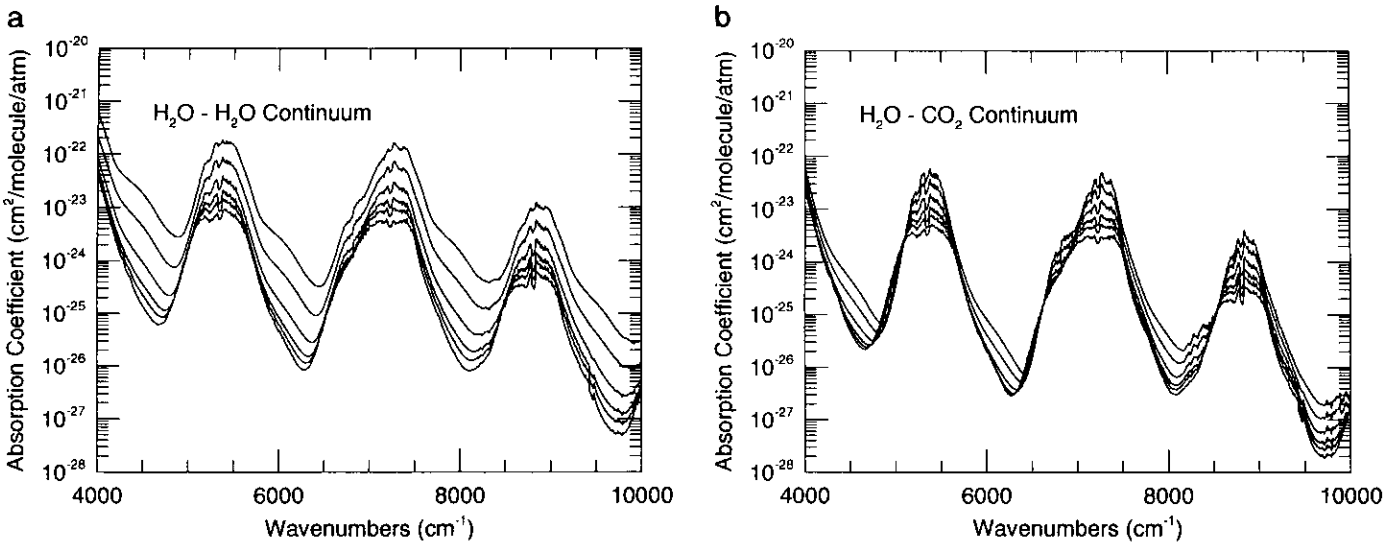

FIG. 3. Absorption coefficient for H_2O continuum opacity (cm^2/molecule/atmosphere) as a function of wavenumber in the 1–2.5-μm region. The various curves show coefficients at a variety of temperatures. From top to bottom, the temperatures are 230, 296, 430, 600, 750, and 1000 K. (a) H_2O being broadened by H_2O; (b) H_2O being broadened by CO_2.

ficient when necessary to achieve an acceptable fit to the data, in the spirit of Bezard *et al.* (1990). Future laboratory and theoretical work are needed to remove the ad hoc flavor of such a procedure.

2.4. *Summary of Spectral Databases*

Based on the above discussion, we formed a standard database of gaseous opacities as follows. We used the HITRAN '91 database for H_2O and CH_4, the high-T databases for CO_2, CO, and the hydrogen halides, and the recently assembled databases for OCS and SO_2. Where necessary, we introduced a wavenumber-independent CO_2 continuum opacity. We also explored the sensitivity of our results to substituting the currently immature high-T database for H_2O in place of the HITRAN one and to including the currently inaccurate estimates of the H_2O continuum opacity. In the latter case, we considered only H_2O–CO_2 opacity for reasons given above.

3. OBSERVATIONS

In this paper, we analyze two sets of recent groundbased spectra of Venus' nightside thermal emission. These sets are moderate-resolution spectra obtained by David Allen and reported in Crisp *et al.* (1991a) and high-resolution spectra obtained by Catherine deBergh and Bruno Bezard and reported in Bezard *et al.* (1990). The spectra of Crisp *et al.* (1991a) represent the first observations of four window regions in the 1.05- to 1.35-μm spectral domain and include near-simultaneous observations of these windows and the ones at 1.7 and 2.3 μm. The spectra of Bezard *et al.* (1990) represent the highest spectral resolution observations that have been published of the two long wavelength window regions.

In this paper, we use the high-resolution spectra as a means of assessing the importance and adequacy of the high-temperature CO_2 database. The implications of these data for gas abundances in Venus' lower atmosphere have been discussed by Bezard *et al.* (1990) and deBergh *et al.* (1991). We analyze the moderate resolution spectra of Crisp *et al.* (1991a) both to further test the high-temperature CO_2 database and to derive cloud optical depths and gas abundances. Below, we briefly summarize the salient properties of these two key sets of spectra of Venus. Toward the end of this section, we show that a number of previously unidentified features in the high-resolution data are due to CO_2 hot bands.

3.1. *Moderate Resolution Spectra*

David Allen obtained spectra of Venus' nightside during February 1990 at the 3.9-m Anglo-Australian Telescope. These data were taken with the FIGS spectrometer at effective spectral resolutions (wavelength/full width at half maximum) of about 450 (lower resolution spectra) and 1800 (higher resolution spectra). Lower resolution spectra of a small region of the planet were obtained in all six window regions on the same occasion, whereas higher resolution spectra were taken in the four longest wavelength windows. There is no commonality in place or time in these latter spectra.

Scattered light from the dayside of Venus was removed from all the nightside spectra by subtracting scaled spectra of the dayside that were taken on the same night (see Allen 1987). The scaling constant was picked so that the

corrected nightside spectra had zero intensity, on the average, at wavelengths outside of the windows. Telluric absorption features were removed and absolute and relative flux calibrations were obtained by dividing the Venus spectra by those of calibration stars that were obtained at very similar airmasses and times (Allen 1987). The absolute and relative fluxes of the resulting nightside Venus spectra have errors of approximately 15 and 5%, respectively.

Figures 4a–d summarize the moderate resolution spectra of Crisp *et al.* (1991a) that is modeled in a later section of this paper. Table I summarizes the cosine of the emission angle, μ, and the effective resolving power, R, of these spectra. We estimated R in two ways. First, we derived its value from the instrumental characteristics, with an approximate allowance for the degradation ($\approx$25%) of R due to the finite size of the entrance aperture of the spectrometer. Second, we found R by comparing synthetic spectra with the observed ones. Certain fine-scale structure in the synthetic spectra depend sensitively on R, but not on the values of gas mixing ratios. In general, these two estimates of R are in good agreement. In our modeling, we used the value of R found from the comparisons with the synthetic spectra, since this value ensures a maximum comparability of observed and theoretical spectra.

3.2. *High-Resolution Spectra*

High-resolution spectra of the nightside of Venus were recorded in the 1.7- and 2.3-μm windows by using the Cassegrain Fourier Transform Spectrometer at the 3.6-m Canada–France–Hawaii telescope on Mauna Kea, Hawaii, on November 10 UT, 1989 (Bezard *et al.* 1990). In this paper, we focus on the short-wavelength portion of the 2.3-μm region that is dominated by CO_2 opacity. A circular aperture with a 5-arcsec diameter was used and was centered on the region of the nightside where the flux was highest: near 30° north latitude and 240°solar fixed longitude.

Three scans, each of 9 min duration, were recorded in the 2.3-μm region and were subsequently coadded to provide a single spectrum with a peak signal to noise ratio of 50. This final spectrum was apodized to a resolution of 0.28 cm^{-1} (full width at half maximum).

Contamination by reflected sunlight from the dayside of the planet was removed by using a concurrent spectrum of the dayside. The dayside contamination amounted to 10% of the peak nightside flux. The 2.3-μm spectrum of the dark side of Venus was divided by a spectrum of the dayside recorded at a similar zenith angle to correct for telluric opacity and for the filter spectral response function. Absolute calibration of the final spectra was performed by comparing the Venus flux with that of standard stars, whose spectra were recorded during the same observing run.

Figure 5 shows the higher wavenumber portion of the 2.3-μm region, which is dominated by CO_2 opacity. In particular, the region from about 4360 to 4470 cm^{-1} is dominated by the 31104–00001 band of the main isotope, whose P and R branch lines and Q branch are clearly visible in Fig. 5. Here, as well as elsewhere, we use standard spectroscopic nomenclature to describe the upper (five numbers to the left) and lower vibrational energy levels of the transition: (v_1, v_2, l, v_3, r), where the v's represent the vibrational quantum numbers associated with the three normal modes of the CO_2 molecule, l represents the vibrational angular momentum, and r represents the order of the Fermi multiplet component, arranged so that $r = 1$ corresponds to the highest energy. This band is centered at 4416.15 cm^{-1}. As discussed in an earlier section, the laboratory measurements of Giver and Chackerian (1991a) have provided a much improved value for the strength of this band, as compared to the value given in Rothman (1986), and this new result has been incorporated into the high-T database.

In analyzing their high-resolution spectra of the 2.3-μm region, Bezard *et al.* (1990) were not able to identify a number of features that appeared in the vicinity of the 4416-cm^{-1} band. These unidentified features are designated by vertical lines in Fig. 5. Comparing the positions and intensities of these features with lines on the high-T database, we find that they can be attributed to components of the 40005–01101 and 32204–01101 hot bands of the main isotope of CO_2 centered at 4355.00 and 4379.89 cm^{-1}, respectively. The lines and branches of these bands that are responsible for the features in question are shown in Fig. 5. These identifications are further supported by the laboratory measurements and the analyses by Giver and Chackerian (1991b). The influence of the 4355- and 4379-cm^{-1} hot bands can also be seen in the more irregular appearance of lines in the region of the P branch of the 4416-cm^{-1} band as compared to lines in the region of its R branch.

4. SYNTHETIC SPECTRA: PROCEDURE

In this section, we describe how we have generated synthetic spectra of the near-infrared window regions. Comparison of these spectra with the observed spectra of Bezard *et al.* (1990) and Crisp *et al.* (1991a) will be discussed in the subsequent section of this paper. Below, we first describe how opacities were calculated and then describe the radiative transfer program that used these opacities to generate synthetic spectra.

4.1. *Opacity*

As a first step in generating synthetic spectra, we must define all the major sources of opacity at altitudes below 80 km in Venus' atmosphere. Both gases and particles

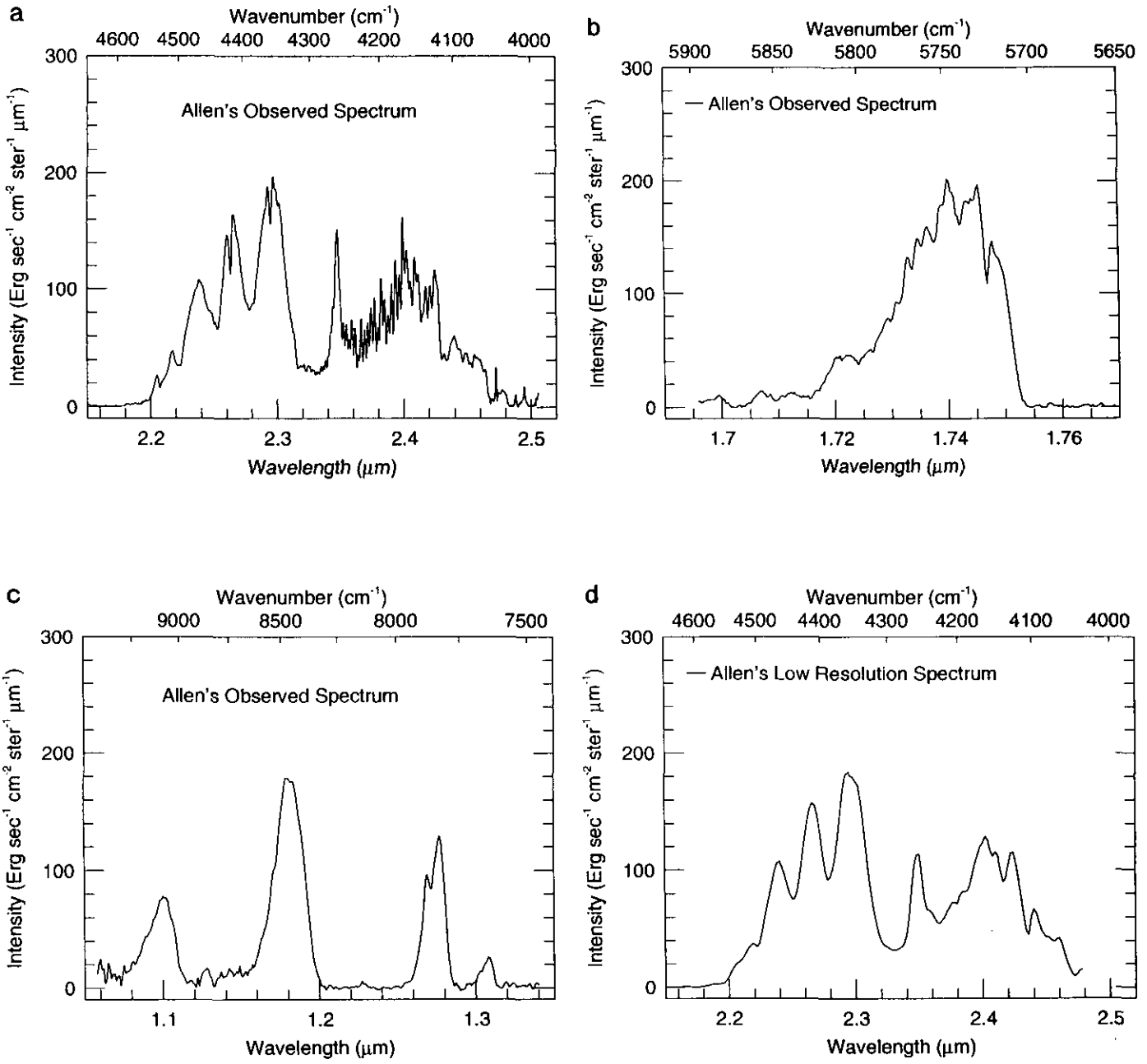

FIG. 4. Spectra obtained by David Allen in 1990 for various window regions and spectral resolutions, R. (a) 2.3-μm window, R = 1600; (b) 1.7-μm window, R = 2100; (c) 1.2-μm window complex, R = 450; (d) 2.3-μm window, R = 450. The spectra shown in (c) and (d) were obtained on the same night of the same spot.

provide significant opacity in this region, although primarily in separate altitude regions, with gases dominating in the region below 48 km and particles dominating at higher altitudes.

For gases, we included opacity due to the permitted transitions of all relevant gas species, the continuum opacity of CO_2 and H_2O, and Rayleigh scattering. (The latter is nontrivial in the shortest wavelength windows). The 1991 version of the AFGL SELECT program and our own verison of the AFGL FASCODE program were used to evaluate the monochromatic opacity of each gas species from the line databases of permitted transitions described in an earlier section of this paper (see Clough *et al.* 1986 for a discussion of the AFGL codes). Our version of FASCODE employed a Lorentz line shape, a very good approximation to the Voigt profile at the high pressures of interest. It also cut off the line profile at a specified distance from the line centers (25 cm^{-1}, except for CO_2)

TABLE I
Properties of the Spectra of Crisp *et al.* (1991)

Date	Wavelength range[a] (μm)	Resolving power[b] Instrument[d]	Resolving power[b] Spectral fit[e]	μ[c]
Feb. 10, 1990	2.120–2.506 (HR)	1725 ± 115	1600 ± 50	0.93
Feb. 9, 1990	1.696–1.769 (HR)	2175 ± 145	2100 ± 50	0.84
Feb. 10, 1990	1.058–1.340 (LR)	450 ± 30	450 ± 25	0.82
Feb. 10, 1990	2.072–2.490 (LR)	430 ± 30	450 ± 25	0.82

[a] The letters HR and LR in parentheses after the spectral range refer to higher resolution and lower resolution, as used in the text.
[b] Resolving power is defined as the ratio of wavelength to the full width at half maximum.
[c] μ is the cosine of the emission angle or, equivalently, the cosine of the viewing angle, as measured from the sub-Earth point on Venus.
[d] Value of the resolving power estimated from a combination of the spectrometer's grating and the finite slit width.
[e] Value of the resolving power estimated from synthetic spectra. See text.

and it incorporated a χ factor for CO_2–CO_2 collisional broadening that was discussed above. By using monochromatic opacities, we formulated the radiative transfer problem in a rigorous fashion and were easily able to vary gas mixing ratios.

These opacities were evaluated every 0.05 cm^{-1} for the 1.7- and 2.3-μm windows and every 0.1 cm^{-1} for the 1.2-μm window complex. These choices were based on numerical tests that ensured an accuracy of better than a few percent in the computed intensities. On the one hand, these choices of the wavenumber spacing are sufficiently fine that they are factors of 5 to 20 smaller than the pressure half-widths of lines in the regions of the lower atmosphere, where almost all of the radiation originates (the pressure at optical depth unity is about 10, 20, and 40 bars in the 2.3-, 1.7-, and 1.2-μm windows, respectively). On the other hand, they are sufficiently coarse that spectra of each window region could be generated in only about several 10s of seconds on a CRAY YMP computer. (Hence, many spectra could be generated to optimize the fit to the observed spectra.)

As discussed in a previous section, we included in our standard set of opacities a highly simplified form of CO_2 continuum opacity in window regions where it was needed. This opacity was assumed to be independent of wavenumber throughout a given window region, with the value of the opacity coefficient being determined from the Venus spectrum itself. (Existing laboratory measurements in the 2.3-μm region display approximately this type of spectral behavior and provide approximate values of its absolute value at room temperature.) We also investigated the sensitivity of our results to the H_2O–CO_2 continuum opacity of Ma and Tipping (1992a,b).

The Rayleigh scattering optical depths were derived from formulae given in Hansen and Travis (1974). The Rayleigh scattering optical depth equals approximately 1.5 at a wavelength of 1 μm for a vertical path from the top of the atmosphere to the surface. Thus, this opacity is most important for the 1.2-μm window complex.

We assumed that the Venus clouds were confined primarily to altitudes between 48 and 70 km and were composed entirely of concentrated liquid sulfuric acid (75% H_2SO_4 by weight). Some justification for these assumptions are provided by data that were analyzed by Crisp (1986), Young (1973),. Pollack *et al.* (1978), and Esposito *et al.* (1983). Thus, we used Mie scattering theory to determine the single scattering albedo and scattering asymmetry parameter of the cloud particles at the wavenumbers of interest. In performing these calculations, we used the measured optical constants of 75% H_2SO_4 solutions at room temperature (Palmer and Williams 1975) and we employed a trimodal size distribution for the cloud particles, based on Pioneer Venus data (Knollenberg and Hunten 1980, Kawabata *et al.* 1980). In particular, we employed a log normal size distribution function for each mode, with mode 1, 2, and 3 particles having modal radii of 0.30, 1.0 (above 57 km) and 1.40 (below 57 km), and 3.65 μm, respectively, and unitless variances of 1.56, 1.29 (above 57 km) and 1.23 (below 57 km), and 1.28, respectively. The functional form of the size distribution is given in a footnote to Table 1 of Pollack *et al.* (1980).

Table IIa summarizes our baseline cloud model. It divides the cloud region into a number of altitude intervals

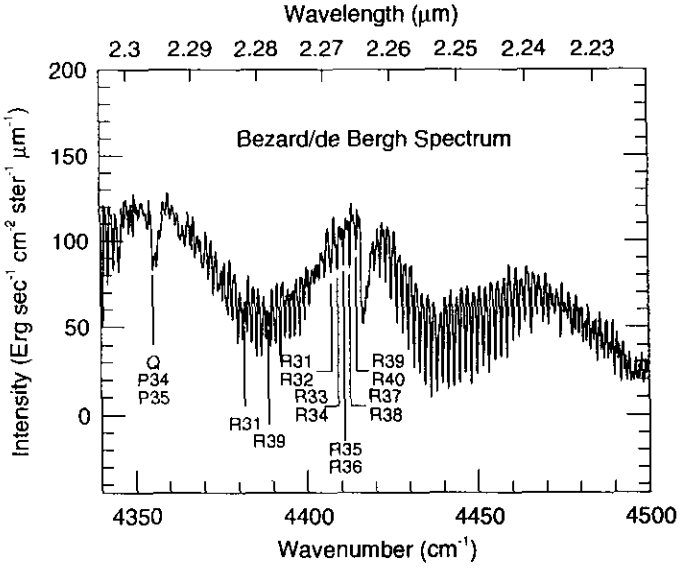

FIG. 5. High-resolution spectra of Bruno Bezard and Catherine de Bergh for a portion of the 2.3-μm window that is dominated by CO_2 opacity. The vertical lines show the location of previously unidentified features. Based on Wattson's high-temperature database for CO_2, we have identified these features as rotational lines associated with two hot bands of CO_2. The leftmost three features are rotational lines of the 40005–01101 band, whereas the remaining features are rotational lines of the 32204–01101 band. See text for convention used for the quantum numbers associated with these bands.

TABLE IIa
Baseline Cloud Model

Layer	Altitude[a] (km)	Pressure (mbar)	Temperature (K)	Optical depth[b] Mode 1[c]	Mode 2	Mode 2'	Mode 3
1	Top–84	0–1.7	183.8–183.8	0	0	0	0
2	84–64	1.7–115.6	183.8–245.4	2.17	7.92	0	0.4
3	64–57	115.6–389	245.4–282.5	1.0	0.2	0	0
4	57–54	389–600	282.5–312.8	0.23	0	0.5	0.2
5	54–50	600–1000	312.8–350.5	0.5	0	2.5	2.4
6	50–48	1000–1400	350.5–366.4	1.6	0	2.31	5.44

[a] The two numbers give the altitudes at the top (left) and bottom (right) of the layer. There is a similar meaning for the pair of numbers given for pressure and temperature.
[b] Optical depth refers to the value from the top to the bottom of the layer and is evaluated at a wavelength of 0.63 μm.
[c] Modes are distinguished by their size distribution and are defined in the text.

and specifies the extinction optical depth at a reference wavelength of 0.63 μm and the contribution of each size mode to that opacity for each altitude interval. This table is based on the cloud model of Crisp (1986), which was derived from an excellent syntheses of available spacecraft data, chiefly the information gathered in 1978 by the Pioneer Venus probes and orbiter. However, we have modified Crisp's model somewhat, especially the opacity profile, to bring it into better accord with the near-infrared spectral/spatial maps obtained by the NIMS experiment during the Galileo spacecraft's flyby of Venus in 1990 (Carlson *et al.* 1991). These data constrain both the optical depth profile near the cloud top and the total cloud optical depth. When applying this model to a specific area on the dark side of Venus, we modified the cloud opacity only in the bottom few kilometers of the main cloud deck (Carlson *et al.* 1991).

The cloud particles have a single scattering albedo, ω, of essentially unity at the reference wavelength; i.e., they just scatter radiation and do not absorb it at a wavelength of 0.63 μm. However, the absorption coefficient of sulfuric acid increases rapidly with increasing wavelength in the near-infrared (Palmer and Williams 1975), so that absorption by the cloud particles becomes progressively more important in determining the amount of radiation transmitted through the clouds with increasing wavelength. Table IIb provides a quantitative definition of the wavelength dependence of the clouds' radiative properties by showing the extinction optical depth, τ_{ext}, and $(1-\omega)$ at the reference wavelength and wavelengths near the centers of the major window regions of interest to this paper. These values were obtained by applying Mie theory to each of the particle size modes and appropriately weighting their contributions to the total cloud radiative properties in accordance with the information of Table IIb.

According to Table IIb, the extinction optical depth of the clouds in the near-infrared is quite similar to its value at the reference wavelength. The value of $(1-\omega)$ at a wavelength of 1.10 μm is too small to noticeably alter the transmission of the clouds from that for pure scattering. However, $(1-\omega)$ is large enough in the two longer wavelength windows for the transmission through the clouds to be significantly smaller than that for pure transmission, with the reduction being greatest at the longest wavelength. This conclusion, as verified by sample radiative transfer calculations, is due to the large amount of multiple scattering that takes place in these optically thick clouds.

4.2. *Radiative Transfer*

We wish to calculate the thermal emission spectrum at the top of Venus' atmosphere in the various window regions between 1 and 2.5 μm. Our methods explicitly account for thermal emission, absorption, and scattering by both gases and particles. For this purpose we use a simple, yet accurate, radiative transfer model. The key inputs to this model are the atmospheric opacity, which has been described above, and the vertical temperature structure, which will be described below.

TABLE IIb
Radiative Properties of the Venus Clouds

Wavelength (μm)	τ_{ext}[a]	$(1-\omega)$[b]
0.63	27.37	0
1.10	28.29	3.68×10^{-5}
1.74	30.84	4.81×10^{-3}
2.30	24.17	2.14×10^{-2}

[a] τ_{ext} is the extinction optical depth.
[b] ω is the single scattering albedo.

The radiative transfer model is based on the two-stream/source function approximation to the equation of radiative transfer for a vertically inhomogeneous, plane-parallel atmosphere that emits, scatters, and absorbs thermal radiation (Toon *et al.*, 1989). In this approach, the two-stream approximation to the angular dependence of the radiation field is used to determine the source function. The intensity at the top of the atmosphere is found by using the source function in the formal solution to the equation of radiative transfer. In this way, the angular dependence of the radiation at the top of the atmosphere, the "observable quantity," is evaluated in an approximate fashion. In particular, this approach leads to exactly the correct result for purely absorbing atmospheres (single scattering albedo = 0) and it produces errors as large as 10% for highly scattering atmospheres (Toon *et al.* 1989).

The near-infrared emission from Venus' nightside is produced in a two-step process. The highly absorbing and emitting region of the atmosphere below the main cloud deck produces almost all the thermal radiation that reaches the top of the atmosphere. The main cloud deck is too cold at wavelengths below 2.5 μm to contribute significantly to the total thermal emission. Instead, its most important function is to attenuate the amount of radiation originating from below it that reaches the top of the atmosphere. Furthermore, this attenuation varies only slowly with wavelength and by rather modest amounts across a given window, since the cloud's optical depth and the particles' single scattering albedo vary only slowly with wavelength (e.g., Crisp 1986). We note that we include in the calculations the slowly changing radiative properties of the cloud particles across each window. Thus, the radiative transfer model should produce little aliasing of the spectral shape of the nightside thermal emission in a given window (perhaps at most on the order of a few percent), but the absolute value may be in error by about 10%. Such errors are comparable to the absolute radiometric accuracy in the observed spectra and should therefore not seriously compromise our efforts to simulate them.

The monochromatic intensity spectra generated by the radiative transfer model was convolved over the spectral response function of the spectrometer used to take the observation of interest to produce a theoretical spectrum that could be directly compared with the observed one. In the case of the moderate resolution spectra of Crisp *et al.* (1991a), we used a triangular slit function, whose effective resolving power, R, was found in two ways, as discussed in Section 3.2, and is given in Table I. For reasons already indicated, we used the value of R derived by matching fine scale structure in the observed spectra to create the synthetic spectra of this paper. In the case of the high-resolution spectra of Bezard *et al.* (1990), we used the spectral response function appropriate to the apodized spectra.

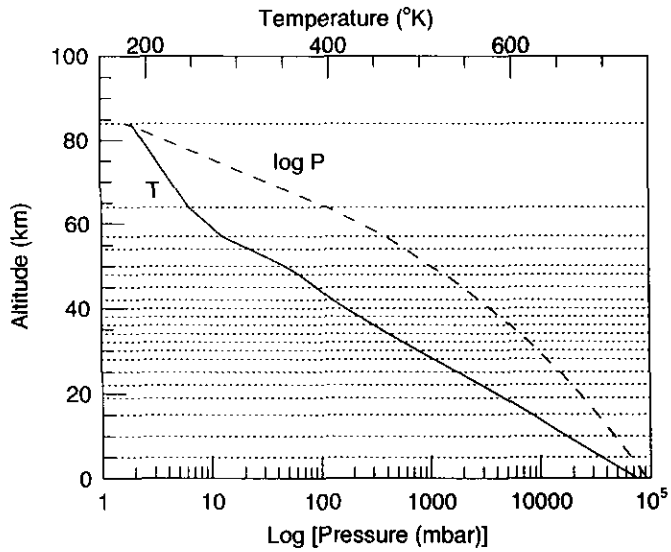

FIG. 6. Pressure and temperature as a function of altitude at low latitudes in Venus' atmosphere. The dashed horizontal lines show the manner in which the atmosphere was subdivided into homogeneous layers for simulations of the 1.7- and 2.3-μm windows. For simulations of the 1.2-μm window complex, we added two layers to the bottom of the atmosphere so that the bottom five layers had thicknesses of 3 km.

We used the equatorial vertical temperature profile of the COSPAR Venus international reference atmosphere in all our simulations, since the observations of interest were obtained at low latitudes (Seiff 1983, Seiff *et al.* 1986). This profile, which is shown in Fig. 6, is based on a synthesis of spacecraft data, primarily that of the Pioneer Venus and Venera probes at the altitudes of greatest interest (below 48 km). These data furthermore indicate that there is not a readily measurable spatial variation of temperature at altitudes below 30 km and only a modest variation of temperature with latitude between 30 and 48 km—at most a few degrees. Thus, we are in a very fortunate position with regard to the near-infrared thermal emission from Venus in that the temperature structure is well known a priori. As a result, a maximum amount of information about gas mixing ratios in Venus' lower atmosphere can be derived by modeling the observed nightside spectra. In particular, it is possible to determine not only the vertically averaged mixing ratio in the altitude range sensed, but also, in several cases, to learn something about the vertical gradient of the mixing ratio, as we discuss in detail in the next two sections of this paper.

5. SYNTHETIC SPECTRA: RESULTS

In this section, we use the radiative transfer algorithm of the previous section, in conjunction with the particulate and gaseous opacities described above to produce synthetic spectra for comparison with the Venus spectra of

Bezard *et al.* (1990) and Crisp *et al.* (1991a). Our primary goals are to assess the adequacy of the current spectroscopic databases and to derive information on the mixing ratios of various gases in the region below the main cloud layers. Aside from the mixing ratios themselves, the free parameters of our model include: (1) the cloud optical depth, τ_{ref}, at a reference wavelength of 0.63 μm and (2) the strength of the CO_2 continuum absorption coefficient, k_{con}, in the various window regions.

With regard to the first of these free parameters, we alter the nominal cloud model of Table I by removing or adding opacity to only the bottom two layers (Carlson *et al.*, 1991). The bottom two layers of our cloud model span the altitude range from 48 to 54 km. We first remove cloud material only from the bottom cloud layer and then remove additional material from the next layer up only if the bottom layer has been entirely depleted and further removal is needed. The same fractional depletion or addition is made for all size modes. We adjust the total cloud opacity to yield predicted intensities, whose absolute values agree, on the average, with the observed ones in portions of a given window region that are dominated by CO_2 opacity. We use these parts of a spectral window so as to have a clean separation between this adjustment and that of the mixing ratios of other gases.

The optical depth determination is done separately for spectra taken at different times (different nights) and/or at different locations on Venus' disk. We refer to this type of adjustment as a DC adjustment. It is important to note that, in a given spectral region, a change of cloud opacity affects only the absolute intensity of the spectrum and very little its spectral shape. Thus, the retrieval of gas abundances is very insensitive to uncertainties in the cloud model and absolute calibration errors in the observed spectrum.

The strength of the CO_2 continuum opacity is adjusted so that the model spectra reproduce the observed amplitudes of variation between local maxima and minima in parts of the spectra dominated by CO_2 opacity or in places dominated by other gases, but where physically "reasonable" mixing-ratio profiles provide the constraint. We refer to this type of an adjustment as an AC adjustment. Based partly on laboratory measurements (see above), we assume that the CO_2 continuum opacity is constant with wavelength in a given window region. The terms DC and AC are drawn by analogy to direct and alternating current in the sense that the DC adjustment affects the absolute values of the overall envelope of the intensities in a given window region, whereas the AC adjustment affects the amplitude of the high-frequency variations of intensity in the window region.

5.1. *Window Spectral and Vertical Locations*

Here, we examine the factors that determine the spectral positions of the major window regions and estimate

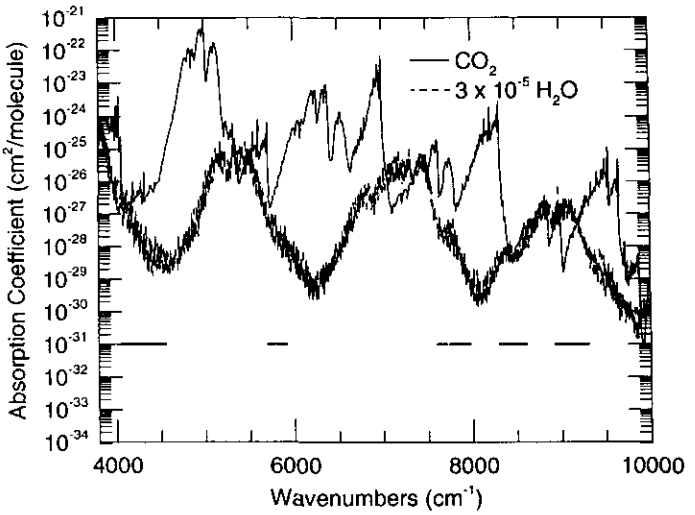

FIG. 7. Monochromatic absorption coefficients of CO_2 (solid curve) and H_2O (dashed curve) at 20 bar and 575 K as a function of wavenumber. The coefficients for H_2O have been multiplied by 3×10^{-5}, its approximate mixing ratio in the lower atmosphere, so that the plotted coefficients are referenced to a Venus "air molecule." The horizontal, thick solid lines show the locations of the various near infrared windows.

the temperature/pressure/altitude locations of the effective emitting levels in these windows. Figure 7 compares the wavenumber positions of the windows studied by Bezard *et al.*(1990) and Crisp *et al.* (1991a) (thick horizontal lines) with the monochromatic absorption coefficients of CO_2 and H_2O, expressed in units of cm^2/Venus "air" molecule. In constructing this figure, we used a value of 3×10^{-5} for the volume mixing ratio of H_2O.

According to Fig. 7, the positions and widths of some windows are determined solely by CO_2 opacity. Examples of these windows include the 1.27-, 1.31-, and 2.3-μm windows. However, the positions and widths of the 1.10-, 1.18-, and 1.74-μm windows are sculptured by a combination of CO_2 and H_2O opacity. For example, the 1.74-μm window would be much broader (it would extend to about 5350 cm^{-1}) were it not for the opacity supplied by the 1.87-μm H_2O band. Also, in the absence of H_2O opacity, there would be additional window regions, such as one centered near 7200 cm^{-1}. According to Fig. 7, an additional window should occur between about 9700 and 10,100 cm^{-1}, in approximate accord with a window centered near 1.01 μm that was detected by the NIMS experiment (Carlson *et al.* 1991). The excellent correspondence of the known window positions with the joint opacity of CO_2 and H_2O means that there are no other major sources of gaseous opacity, although other molecules certainly provide significant amounts of opacity in limited portions of some of the window regions.

The brightness temperature spectra of models having no cloud opacity provide a convenient means for defining

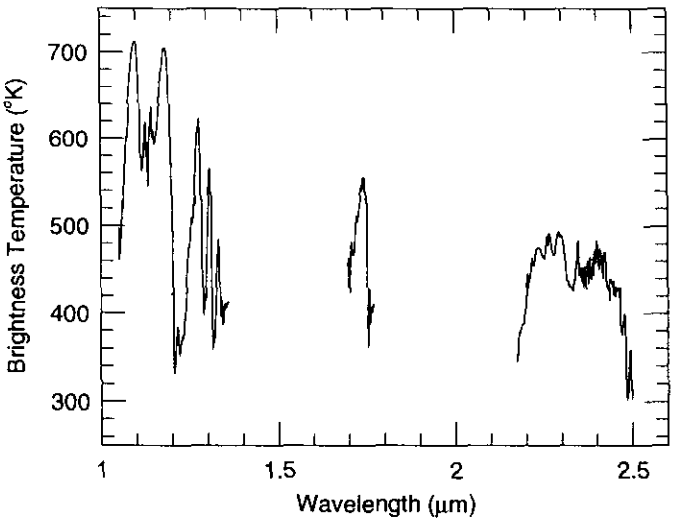

FIG. 8. Brightness temperature for the various window regions as a function of wavenumber.

the effective emitting levels in the atmosphere across each of the window regions. To define these, we eliminate cloud opacity since the clouds significantly reduce the amount of thermal radiation from the atmosphere beneath them that reaches space without adding significant amounts of thermal radiation of their own. In a similar vein, we set the Rayleigh scattering optical depth to zero. (This is important only in the 1.2-μm window complex.) Finally, we set the cosine of the viewing angle, μ, equal to 0.5. This choice is appropriate, since thermal radiation from the lower atmosphere is scattered many times by the cloud particles before it exits the atmosphere and since our radiative transfer program employs a hemispheric mean, two-stream approximation to define the source function of light that reaches the top of the atmosphere (Toon *et al.*, 1989).

Figure 8 displays a brightness temperature spectrum for cloudless Venus models of the 2.3-, 1.74-, and 1.2-μm multiwindows. This spectrum was produced from our best compositional and opacity models, which are detailed later in this section. Thus, for each portion of a spectral window, we can estimate the temperature at the effective emitting level. The observed thermal emission at the top of the atmosphere originates chiefly from a limited vertical extent of the atmosphere, centered around the effective emitting level and covering about half an atmospheric scale height in either vertical direction. This concept was helpful for deciding in what vertical positions to vary gas mixing ratios to obtain a match between observed and synthetic spectra. For example, radiation from the central portions of the 2.3-μm window originate near the 500 K–10-bar–30-km altitude level (cf., Figs. 6 and 8).

We have also evaluated sensitivity functions, $S(\alpha_i)_{jl}$, to define more precisely the altitude range over which the spectral observations in a given window region are sensitive to the mixing ratio α of gas species i. Indices j and l refer to wavelength and model layer, respectively. The sensitivity functions were evaluated by varying α_i in each model layer, one at a time, by a fixed percentage from its optimum value. We evaluated S at two wavelengths in each window that corresponded to maximum and minimum intensity points at which the observed spectra are especially sensitive to the presence of gas species i (cf., Fig. 12 and the discussion below). As in the case of the brightness temperatures of Fig. 8, we performed these calculations for cloudless model atmospheres and a cosine of the emission angle = 0.5 (although equally valid and almost exactly the same shaped functions would have been found for cloudy atmospheres and the emission angle set equal to that of observations).

Figures 9a–9c display the sensitivity functions for the maximum intensity points for all the gas species of interest and all the relevant window regions. In general, the sensitivity function approaches a constant value at the highest and lowest altitudes, corresponding to the intensity value obtained with the optimum mixing ratio used throughout the atmosphere; i.e., this asymptotic value corresponds to the case of no sensitivity. The difference between the asymptotic value and the intensity at intermediate altitudes is a measure of the sensitivity of the computed intensity to α_i in model layer l. We refer to this difference in intensities as the "sensitivity." For example, the sensitivity at a wavelength of 2.40 μm is largest for the layer centered at 34 km and, therefore, the computed intensity is most sensitive to the mixing ratio of H_2O in this layer (with a nearly comparable sensitivity for the layer centered at 32 km) (cf., Fig. 9a).

Figures 9a–9c also provide an accurate measure of the width of the sensing region from the altitude span of layers having a sensitivity that is at least half of the peak sensitivity (e.g., 24 to 46 km for H_2O at 2.40 μm—cf., Fig. 9a). In most cases, the sensitivity function is narrower on the low-altitude side of the layer showing peak sensitivity than on the high-altitude side. This is due to the onset of optical depths in excess of unity on the low-altitude side, which leads to exponential attenuation of the signal from the deeper layers. The sensitivity function for OCS is particularly narrow due to a combination of exponential attenuation at low altitudes and a rapidly diminishing mixing ratio at high altitudes (see below). The sensitivity functions for the minimum-intensity points have an appearance very similar to their maximum intensity counterparts, except that they are displaced upward in altitude by a few kilometers.

The sensitivity functions of Fig. 9 are superior to the conventional contribution functions in several regards (a contribution function provides a measure of the fraction

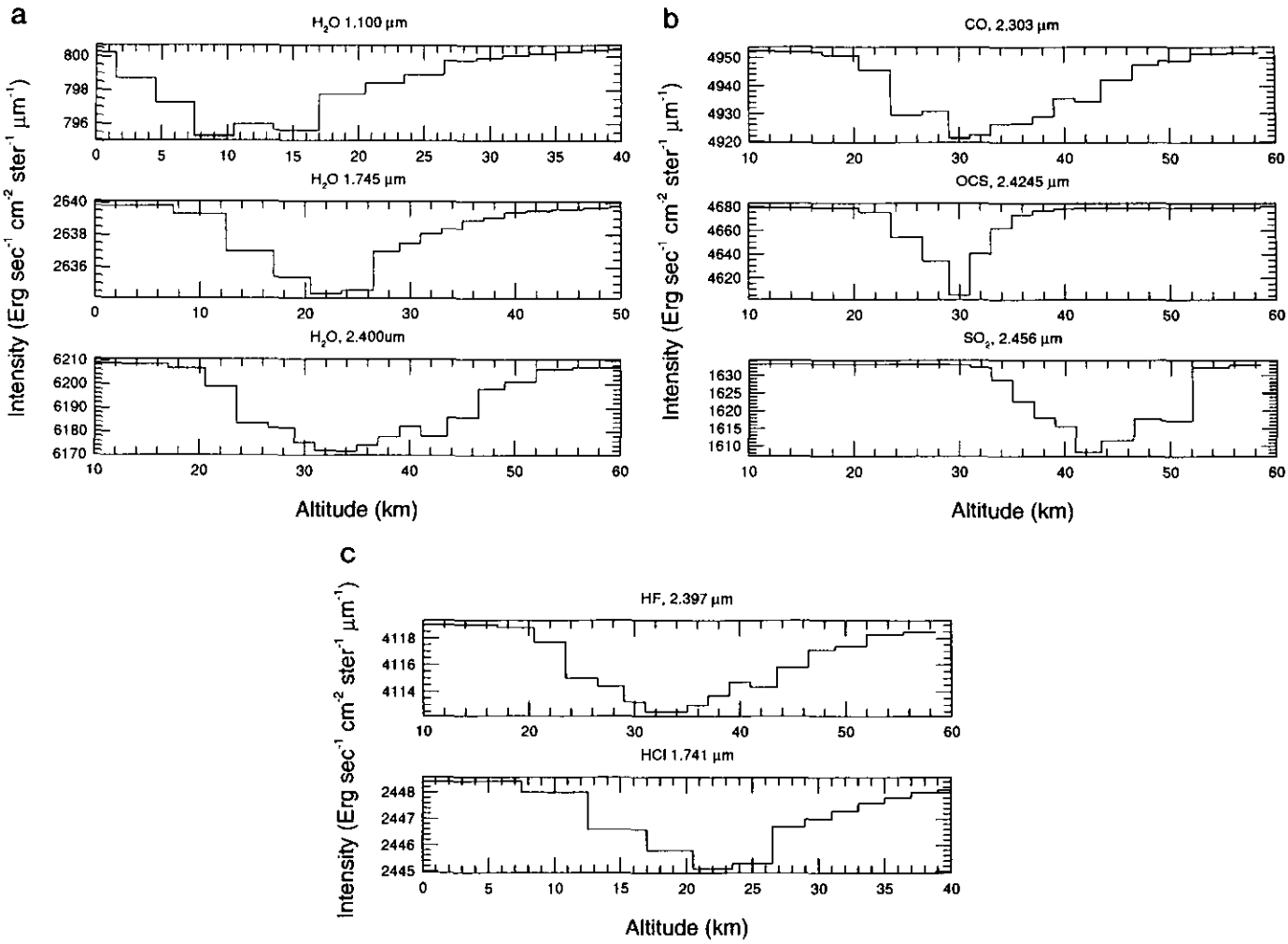

FIG. 9. Sensitivity functions showing the variation of the computed intensity at the top of a cloudless model atmosphere produced by constant ±15% changes to the optimum mixing ratio of a given gas species in each model layer. The horizontal axis shows the altitudes spanned by the various model layers. All calculations shown here are for maximum intensity points (see text). The legends just above the figures show the gas species and the wavelength of the calculations. (a) H_2O for the 2.3-, 1.7-, and 1.10-μm windows. Note that the altitude scales differ among these three windows; (b) CO, OCS, and SO_2 for the 2.3-μm window; (c) HF for the 2.3-μm window and HCl for the 1.7-μm window.

of the intensity at the top of the atmosphere that is produced in each atmospheric layer). First, the sensitivity function accurately reflects the impact of gradients in the mixing ratio on the span of altitudes where the mixing ratio may be constrained by the observed intensities. For example, a broader and somewhat displaced span of altitudes would have been found had contribution functions been used instead of sensitivity functions for OCS. Second, the sensitivity functions reflect much better the loss of information content as the surface is approached due to a diminishing thermal contrast between the atmosphere and surface (see the later discussion of the water vapor profiles inferred from the 1.2-μm window complex).

5.2. *Simulations of the 2.3-μm Window*

Here, and in the subsequent two subsections, we present simulations of the various window regions, for which we use the "standard" set of gas opacities. In a still later subsection, we will consider the impact on our results of other choices of gas opacities. We have simulated the higher resolution spectrum (R = 1600) of Crisp *et al.* (1991) of the 2.3-μm window to derive estimates of the mixing ratio profiles of H_2O, CO, OCS, SO_2, and HF in the vicinity of the 10-bar pressure level.

The first step is to estimate the strength of the wavelength-independent CO_2 continuum absorption coefficient, k_{con}. We do so by matching the AC amplitudes of rotational lines in the vicinity of the 4416-cm^{-1} band of CO_2. For this purpose, we use the very high spectral resolution observations of Bezard *et al.* (1990), which are shown in Fig. 10a. We generated a series of synthetic spectra for comparison with the spectrum of Fig. 10a by systematically varying the value of k_{con}. In each case, we adjusted the DC level to agree with the observed mean

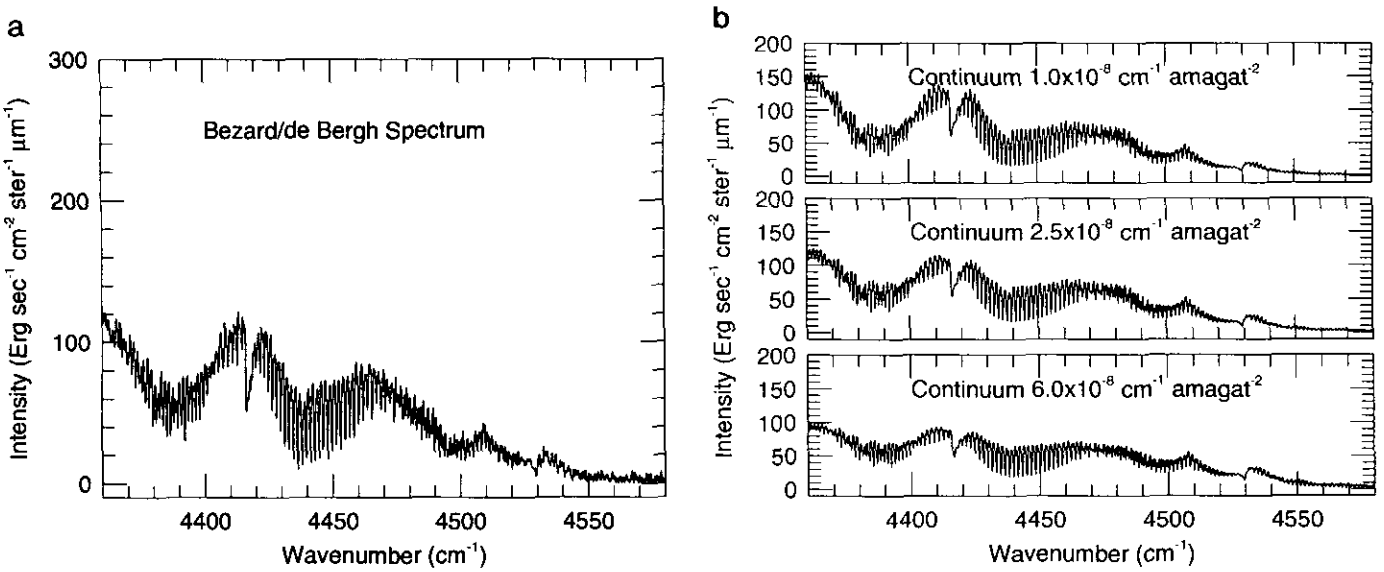

FIG. 10. Observed and synthetic spectra having various values of a wavelength-independent continuum coefficient, k_{con} for the region near the 4416-cm^{-1} band of CO_2. (a) Observed spectrum of Bezard and deBergh; (b) synthetic spectra for k_{con} = 1.0 × 10^{-8}, 2.5 × 10^{-8}, and 6.0 × 10^{-8} cm^{-1} amagat^{-2}.

intensity between 4380 and 4400 cm^{-1}: The mean intensity in this wavenumber interval is close to the average for the entire interval. Examples of synthetic spectra are shown in Fig. 10b.

In deriving a best fit value of k_{con}, we found it particularly useful to use the AC amplitudes of the Q branch of the 4416 cm^{-1} band, individual lines of the R branch of this band, and the variation of the mean intensity between 4420 and 4440 cm^{-1}: There is little interference from other CO_2 bands in this region and the high-T database incorporates accurate laboratory measurements of the 4416 cm^{-1} band by Giver and Chackerian (1991a). Comparing Fig. 10b with Fig. 10a, we see that the AC amplitudes of the synthetic spectra for k_{con} = 1 × 10^{-8}, 2.5 × 10^{-8}, and 6 × 10^{-8} cm^{-1} amagat^{-2} are too large, about right, and too small, respectively, relative to the observed amplitudes. From careful scrutiny of a larger number of synthetic spectra, we conclude that the best fit value for k_{con} is (2.5 ± 0.5) × 10^{-8} cm^{-1} amagat^{-2}.

The second step in the analysis of the 2.3-μm window is to estimate the value of the cloud optical depth, τ_{ref}, by fitting the DC level of the spectrum of Crisp *et al.* (1991) in the 2.15–2.30-μm region, where CO_2 is the dominant source of opacity. The observed spectrum is shown in Fig. 4a. Figure 11a illustrates the enormous sensitivity of the DC level to very modest changes in cloud optical depth. The two curves of this figure correspond to τ_{ref} changing by ±10% from its best fit value. Clearly, it is possible to determine τ to a formal accuracy of a few percent, with this accuracy being limited by the 10% uncertainty in the absolute values of the observed intensities. We obtain a best fit value for τ_{ref} of 25.8 at the reference wavelength of 0.63 μm.

The next step in our analysis is to determine the portions of the 2.3-μm window within which a given gas species makes a noticeable contribution to the total opacity. In this way, we can separate, to some extent, the determinations of the gas abundances of the five species of interest, although, ultimately, this determination becomes an iterative process. We use our best fit mixing ratio profiles as a standard here (see below) and determine the effect on the model spectra of alternately increasing and decreasing the standard profile of each gas species, one at a time, by a factor of two at all altitudes. (Naturally, we do not know the best fit profiles at the start of the calculation, but essentially the same set of sensitivities characterizes almost any reasonable set of profiles.) Figures 12a–12e show the results of such a sensitivity analysis for CO, H_2O, OCS, SO_2, and HF, respectively. Figure 12f summarizes the portions of the 2.3-μm window that show sensitivity to the presence of each of the gas species.

In constructing Figs. 12a–12f and in all our analysis below, we lump together all the isotopes of a given gas species. In almost all cases, we use terrestrial isotopic abundances, an assumption that agrees well with available measurements of gases in Venus' atmosphere (Von Zahn *et al.*, 1983). A very important exception is the D/H ratio, which is elevated by about a factor of 100 in the water vapor of Venus' atmosphere as compared to the ratio for terrestrial ocean water. In our analyses, we use a D/H ratio of 0.019 based on spacecraft and groundbased measurements of water vapor in Venus' atmosphere

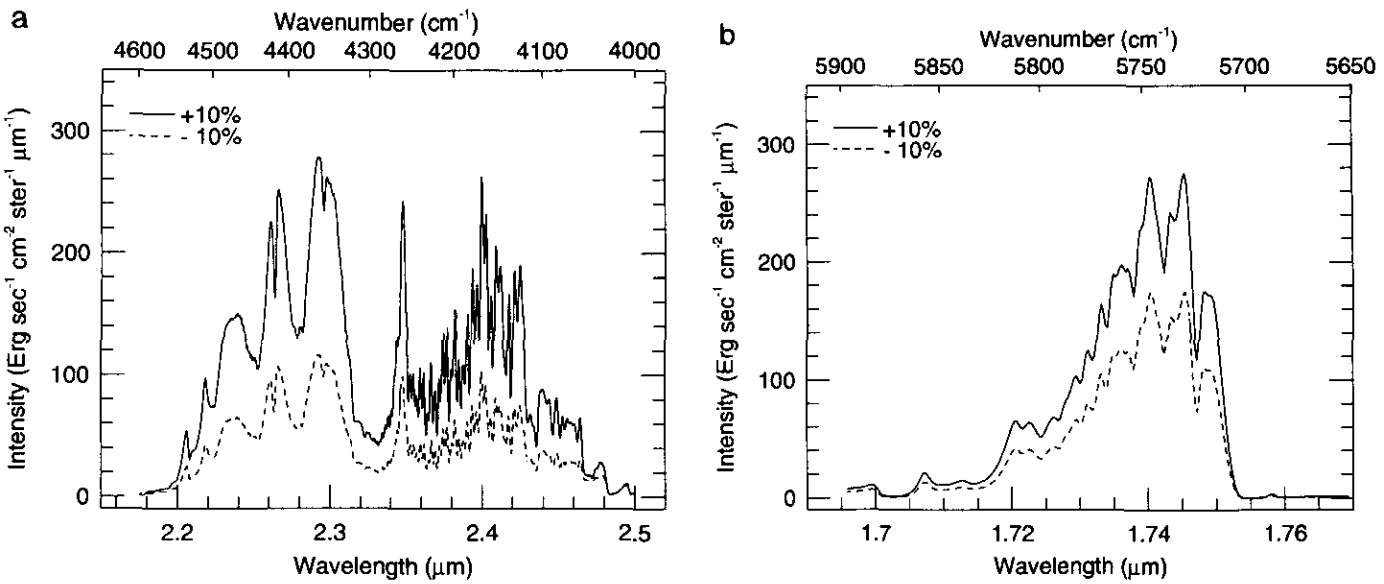

FIG. 11. Sensitivity of the synthetic spectra to the cloud optical depth, τ. τ is varied by $\pm 10\%$ from the best fit value to the observed spectra. Best fit values for the other parameters have been used. (a) 2.3-μm window; (b) 1.7-μm window.

(Donahue *et al.* 1982, deBergh *et al.* 1991). Thus, the HDO/H_2O ratio is set equal to 0.038. HDO opacity plays a major role in the 2.3-μm window, comparable in magnitude to that of H_2O. Consequently, the H_2O abundance derived from this window depends sensitively on the choice of the D/H ratio, which, fortunately, is well determined. However, the HITRAN database lacks information about HDO bands in all the shorter wavelength windows. The term "H_2O" below includes the HDO isotope.

According to Figs. 12a–12f, none of the trace gas species of interest affects the spectrum in a noticeable way at wavelengths shortward of 2.3 μm; i.e., CO_2 is the dominant source of opacity in this spectral domain. Thus, the short wavelength portion of the 2.3-μm region can be used to determine the values of k_{con} and τ_{ref}, even before the mixing ratios of the other gas species have been determined. H_2O and CO affect the spectrum over a broad range of wavelengths; however, the 2.3–2.35-μm region exhibits a much greater sensitivity to CO than to H_2O and the converse is true at wavelengths between 2.40 and 2.43 μm. Thus, it is possible to separately evaluate the CO and H_2O mixing ratios from the observed spectrum for the 2.3 μm window. Once these ratios have been determined, then it is possible to estimate the mixing ratios of OCS, SO_2, and HF, which affect much more limited portions of the window region than do CO and H_2O. In this regard, it is best to estimate the mixing ratio of OCS first and that of SO_2 second, since they have some overlap in the domains where the spectrum shows sensitivity to their presence and since OCS affects a broader portion of the spectrum. We can anticipate that the mixing ratio profiles of CO and H_2O will be best constrained by the observed spectrum for the 2.3-μm window, the profile for OCS will be somewhat less well constrained, the profile for SO_2 will be still less well constrained, and the profile for HF will be least well constrained.

Once we have defined the range of wavelengths that are sensitive to the abundance of a given gas species, we examine the brightness temperature spectrum of "cloudless Venus" (cf., Fig. 8) to determine the atmospheric temperatures and hence the pressures at the effective emitting levels (cf., Fig. 6). We consider effective emitting levels for both local maxima and local minima in the spectrum where there is sensitivity to the presence of the gas species of interest. We focus on altering the gas mixing ratios that lie within half a scale height in either direction of these effective emitting levels in trying to derive mixing ratios that produce good fits to the spectrum in the sensitive range of wavelengths. When the gas abundances change significantly, we reevaluate the brightness temper-

FIG. 12. Sensitivity of the synthetic spectra to variations in the profiles of gas mixing ratios. In each case, the profile for one species has been varied by scale factors of 0.5 and 2.0 from their best fit values. Otherwise, best fit parameters have been used. Sensitivity to: (a) CO; (b). H_2O; (c) OCS; (d) SO_2; (e) HF. (f) Summary of the portions of the 2.3-μm window that show sensitivities to the various gas species.

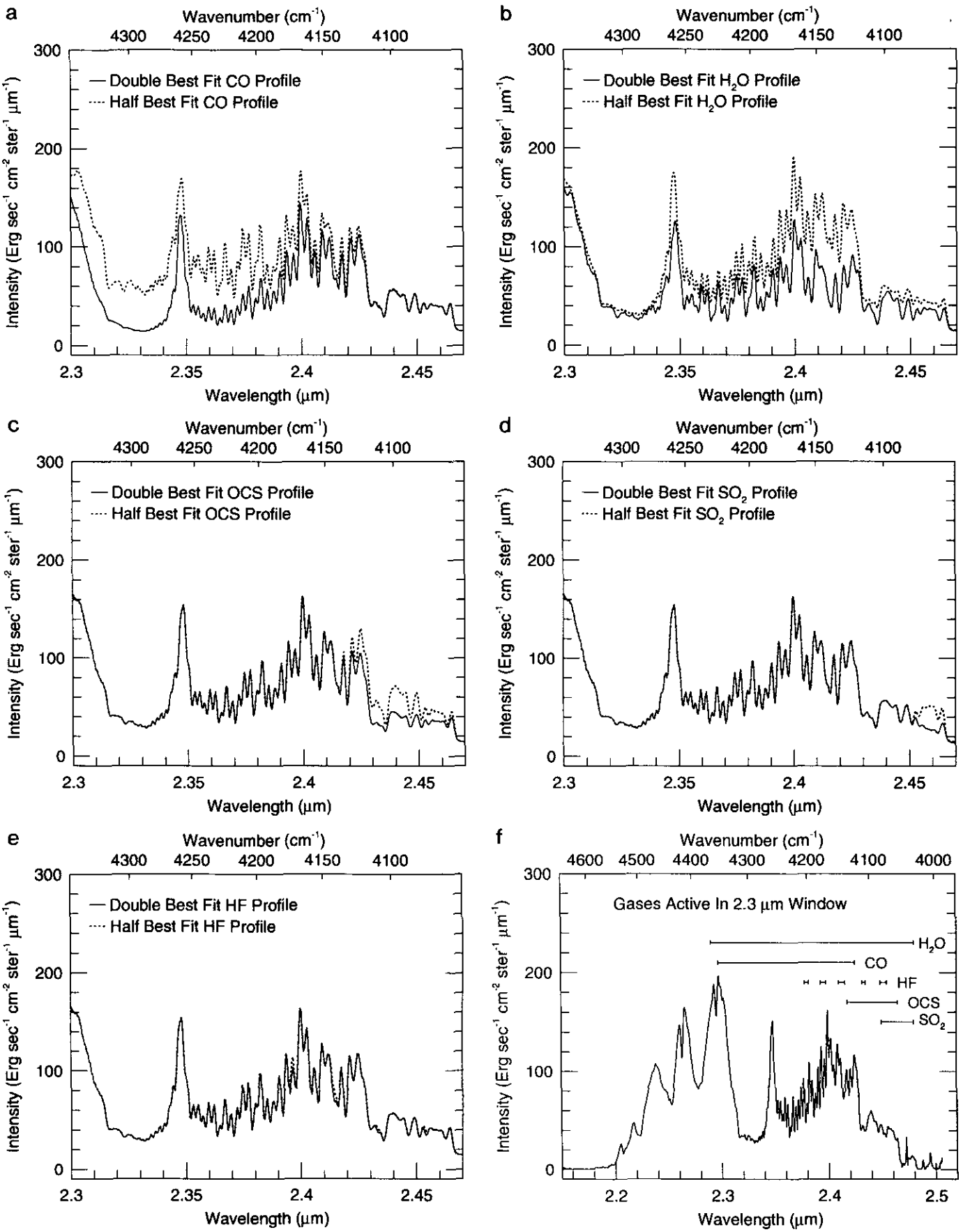
a
Wavenumber (cm^{-1})
4300 4250 4200 4150 4100
— Double Best Fit CO Profile
···· Half Best Fit CO Profile
Intensity (Erg sec^{-1} cm^{-2} ster^{-1} μm^{-1})
300 200 100 0
2.3 2.35 2.4 2.45
Wavelength (μm)
b
Wavenumber (cm^{-1})
4300 4250 4200 4150 4100
— Double Best Fit H_2O Profile
···· Half Best Fit H_2O Profile
Intensity (Erg sec^{-1} cm^{-2} ster^{-1} μm^{-1})
300 200 100 0
2.3 2.35 2.4 2.45
Wavelength (μm)
c
Wavenumber (cm^{-1})
4300 4250 4200 4150 4100
— Double Best Fit OCS Profile
···· Half Best Fit OCS Profile
Intensity (Erg sec^{-1} cm^{-2} ster^{-1} μm^{-1})
300 200 100 0
2.3 2.35 2.4 2.45
Wavelength (μm)
d
Wavenumber (cm^{-1})
4300 4250 4200 4150 4100
— Double Best Fit SO_2 Profile
···· Half Best Fit SO_2 Profile
Intensity (Erg sec^{-1} cm^{-2} ster^{-1} μm^{-1})
300 200 100 0
2.3 2.35 2.4 2.45
Wavelength (μm)
e
Wavenumber (cm^{-1})
4300 4250 4200 4150 4100
— Double Best Fit HF Profile
···· Half Best Fit HF Profile
Intensity (Erg sec^{-1} cm^{-2} ster^{-1} μm^{-1})
300 200 100 0
2.3 2.35 2.4 2.45
Wavelength (μm)
f
Wavenumber (cm^{-1})
4600 4500 4400 4300 4200 4100 4000
Gases Active In 2.3 μm Window
H_2O
CO
HF
OCS
SO_2
Intensity (Erg sec^{-1} cm^{-2} ster^{-1} μm^{-1})
300 200 100 0
2.2 2.3 2.4 2.5
Wavelength (μm)

TABLE III
Gas Mixing Ratios from Other Investigations

Gas	Mixing ratio (ppm)	Altitude (km)	Reference
SO_2	0.05	69	Von Zahn *et al.* 1983
	4.0	58	Von Zahn *et al.* 1983
	185 ± 43	22	Oyama *et al.* 1980
	130 ± 35	≤42	Gel'man *et al.* 1979
	(30–50)	25–40	Berto *et al.* 1987
OCS	≤0.01	≥65	Von Zahn *et al.* 1983
HCl	0.6 ± 0.12	65	Connes *et al.* 1967
	0.4	65	Young (1972)
HF	$5^{+5}_{-2.5}$	65	Connes *et al.* 1967
	10	65	Young 1972
CO	10	80	Clancy and Muhleman 1985
	45 ± 10	65	Connes *et al.* 1968
	51	65	Young 1972
	30 ± 18	42	Oyama *et al.* 1980
	20 ± 3	22	Oyama *et al.* 1980
	28 ± 7	36–42	Gel'man *et al.* 1979
	17 ± 1	12	Marov *et al.* 1989
H_2O	1[a]	65	Von Zahn *et al.* 1983
	10	55.5	Donahue and Hodges 1992
	15	51.3	Donahue and Hodges 1992
	150	42	Moroz *et al.* 1979
	60	22	Moroz *et al.* 1979
	20	0	Moroz *et al.* 1979

[a] Near the cloud tops, the H_2O mixing ratio is highly variable.

ature spectrum of cloudless Venus. In the final iterations, we employ the sensitivity functions of Figs. 9a–9c and their minimum intensity counterparts to refine the definition of the sensing regions. This was particularly important to do in the case of gas mixing ratios that varied over their sensing region (e.g., OCS).

We also constrain the mixing ratio profile to be consistent with measurements outside the near IR sensing regions. Table III summarizes these constraints. At altitudes below the sensing region for a given window region, we simply set the gas mixing ratio equal to its value at the bottom of the sensing region to avoid giving the appearance that we have derived the profile over a larger range of altitudes than we actually have.

Numerical experiments show that it is possible to derive more than simply the mixing ratio at the average effective emitting level. In some cases, it is possible to derive both the mixing ratio and its gradient at the average effective emitting level. The physical reasons that this is possible are discussed in the next section of the paper. Here, we simply point out that the mean mixing ratio is found by fitting the DC level of the sensitive wavelengths (the average intensity in the spectral region from 2.42 to 2.46 μm), while the gradient is obtained from the AC information (the variation of intensity in this spectral region).

Figure 13a illustrates the inability of models having a constant mixing ratio of OCS in the sensing region (26–39 km) to fit the observed spectrum. In constructing this figure, we used our best fit mixing ratio profiles for the other gas species. When the OCS mixing ratio is set equal to 0.1 ppm in the sensing region, the synthetic spectrum lies systematically above the observed spectrum from 2.42 to 2.46 μm. When the OCS mixing ratio is increased by an order of magnitude, the computed spectrum is still too high between about 2.42 and 2.43 μm, but it is now too low between about 2.43 and 2.46 μm. Clearly, there is no choice of a constant OCS mixing ratio that will adequately fit the observations in this spectral domain.

A much better fit to the spectral region from 2.42 to 2.46 μm can be achieved when the OCS mixing ratio, α, is allowed to increase sharply with decreasing altitude across the sensing region, as illustrated in Fig. 13a. The mixing ratio profile that yields the optimum fit is shown by the middle OCS profile in Fig. 13b. Within the sensing region, we assumed that $\ln(\alpha)$ was a linear function of altitude. Below the sensing region, α was arbitrarily set equal to a constant, its value at the base of the sensing region, since we have no constraints on its values at low altitudes.

Noticeably worse fits to the observed spectrum were obtained when the slope of the OCS profile in the sensing region was altered to one of the extreme cases of Fig. 13b. The extreme cases correspond to varying the slope by ±25%. For the optimum OCS profile, the OCS mixing ratio, α, equals 4.4 ± 1.0 ppm and its slope, $d\alpha/dz$, equals −1.58 ± 0.30 ppm/km at an altitude of 33 km, the midpoint of the sensing region. Here, as elsewhere, we operationally define the midpoint of the sensing region to be the average of the altitudes of the sensitivity functions for the maximum and minimum intensities, where the sensitivity is greatest to variations in the mixing ratio of the gas species of interest (cf., Figs. 9a–9c and their minimum-intensity counterparts). The error bars quoted here, as well as ones below, are based on a combination of the sensitivity tests shown in Fig. 12 and additional, more detailed comparisons. We have tried to be conservative in estimating the error bars.

In a similar vein, we found that we could better fit the spectrum when we allowed the CO mixing ratio to decrease with decreasing altitude across the sensing region. Figures 14a and 14b show the best fits to the observed spectrum for two choices of a constant CO mixing ratio. The synthetic spectrum with a CO mixing ratio of 25 ppm fits the region between 2.35 and 2.40 μm fairly well, but it has intensities that are systematically too high between 2.31 and 2.34 μm (cf., Fig. 14a). Conversely, the

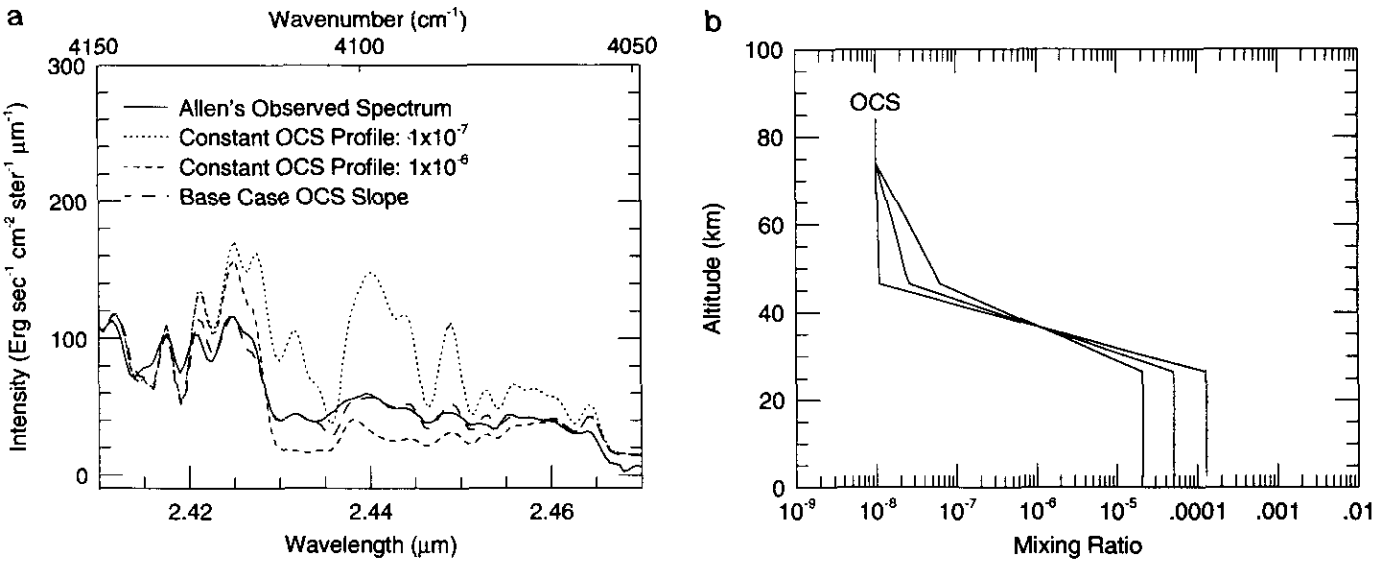

FIG. 13. (a) Comparison of synthetic spectra for various OCS mixing ratio profiles (see legend) with the observed spectra in the 2.3-μm window. Otherwise, best fit values of the other parameters have been used. (b) OCS mixing ratio profiles that increase steeply toward lower altitudes in the sensing region. The middle curve yields an optimum fit to the observed spectrum and it was employed to generate the curve labeled "base case OCS slope" in (a). The other two curves represent large enough variations from this base case that synthetic spectra employing them provide noticeably poorer fits to the observed spectrum.

synthetic spectrum with a CO mixing ratio of 30 ppm gives a good fit between 2.31 and 2.34 μm, but it has intensities that are too low between 2.35 and 2.40 μm (cf., Fig. 14b). A better fit than either of these cases can be achieved by introducing a slope to the CO mixing ratio, as illustrated in Fig. 14c. As for OCS, we assumed that $\ln(\alpha)$ was a linear function of altitude within the sensing region and had a constant value below it. This best fit case is characterized by a CO mixing ratio equal to 23 $\pm$ 5 ppm and a gradient, $d\alpha/dz$, equal to $+1.20 \pm 0.45$ ppm/km at 36 km, the midpoint of the CO sensing region.

We find that good fits can be achieved with constant mixing ratios of H_2O, SO_2, and HF across their sensing regions. These best fit values equal 30 $\pm$ 6 ppm for H_2O at 33 km, 180 $\pm$ 70 ppm for SO_2 at 42 km, and 0.001–0.005 ppm for HF at 33.5 km, where these altitudes refer to the midpoints of the sensing region for a given gas species. We found that it was possible to estimate crudely the HF abundance by matching a feature near 2.39 μm (cf., Fig. 12e) once the H_2O and CO abundances had been determined. However, more precise estimates of the HF abundance require the use of higher resolution spectra (e.g., Bezard *et al.* 1990).

Donahue and Hodges (1993) have found evidence for anomalously high amounts of methane in the bottom 60 km of Venus' atmosphere from a reanalysis of the measurements made by the Pioneer Venus mass spectrometer. In particular, they derive methane mixing ratios of about 1000 ppm at altitudes above 20 km and even larger values at lower altitudes, including a peak of about 6000 parts per million at 12 km. Since methane has strong bands that lie within the 1.7- and 2.3-μm window regions, we have carried out simulations of model atmospheres that contain constant mixing ratios of CH_4 throughout the sensing regions in an attempt to detect the presence of CH_4 in the nightside spectra or to set an upper limit on its abundance. Figure 15 shows an example of such a simulation for a model that incorporates the best fit mixing ratio profiles of other gases. In this example, the presence of 0.35 ppm CH_4 introduces marked features in the region from 2.23 to 2.31 μm that is otherwise dominated by CO_2 opacity. Quite clearly, this synthetic spectrum provides an unacceptable fit to the observed spectrum.

From a careful analysis of other synthetic spectra having varying methane mixing ratios, we set a conservative upper bound of 0.1 ppm on the CH_4 mixing ratio in the sensing region of the 2.3-μm window. This region has a peak sensitivity at 30 km and covers approximately the altitude region from 24 to 44 km. In a similar vein, we find that significant amounts of CH_4 in the 1.7-μm region result in obvious distortions of the observed spectrum. For this region, we obtain a conservative upper limit of 2 ppm for the sensing region that is centered at 24 km and that spans the altitude region from 17 to 27 km. We conclude that the amounts of methane present in the PV mass spectrometer data are not representative of the lower part of Venus' atmosphere, at least the part above about 20 km.

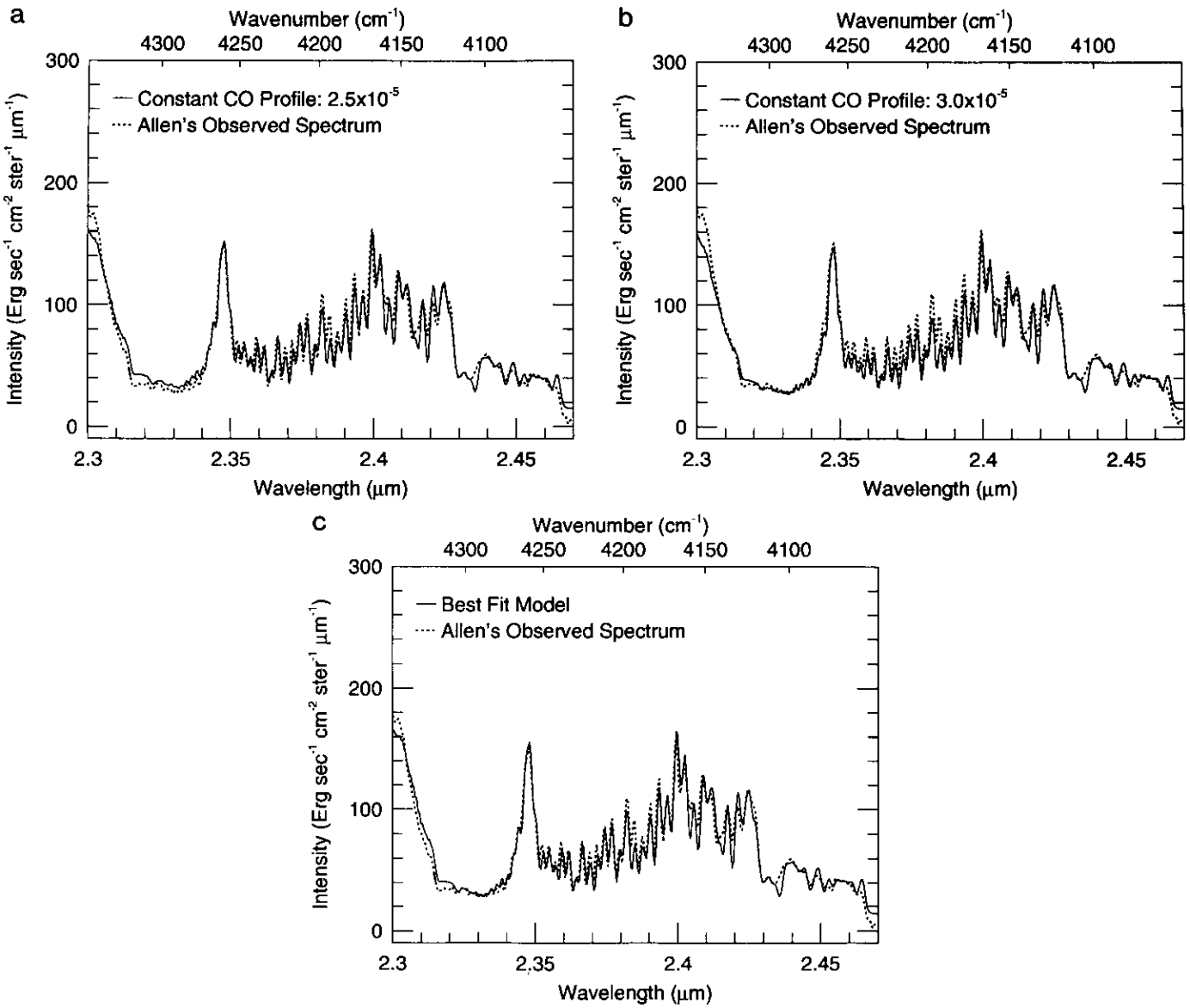

FIG. 14. Comparisons between synthetic spectra constructed with various mixing ratio profiles of CO in the sensing region of the 2.3-μm window and the observed spectrum. The best fit values of other parameters have been used. The CO mixing ratio equals: (a) a constant 25 ppm; (b) a constant 30 ppm; (c) a mixing ratio that decreases with decreasing altitude in the sensing region (see text).

Figure 16a shows the fit of our optimum model to the observed spectrum for the 2.3-μm window, whereas Fig. 16b summarizes the inferred mixing ratio profiles for CO, OCS, H_2O, SO_2, and HF. These profiles were derived by combining our results in the sensing region with values determined from other observations at altitudes above the sensing region (cf., Table III) and by setting the mixing ratios at altitudes below the sensing region equal to the values at the base of the sensing regions. The HCl profile was derived from spectra in the 1.7-μm region and is discussed below. Water mixing ratios retrieved from other window regions will also be discussed below. Finally, the HDO profile in Fig. 16b was derived by multiplying the H_2O profile by 0.038, in accord with the discussion above.

5.3. *Simulations of the 1.7-μm Window*

Figure 4b shows the spectrum of the 1.7-μm window that we simulate in this subsection to derive estimates of the mixing ratios of H_2O and HCl at altitudes whose midpoint lies about 10 km below the sensing regions for the 2.3-μm window (cf., Figs. 6 and 8). First, we adjusted the DC level of the simulated spectrum to match the observed mean intensities at wavelengths between 1.715 and

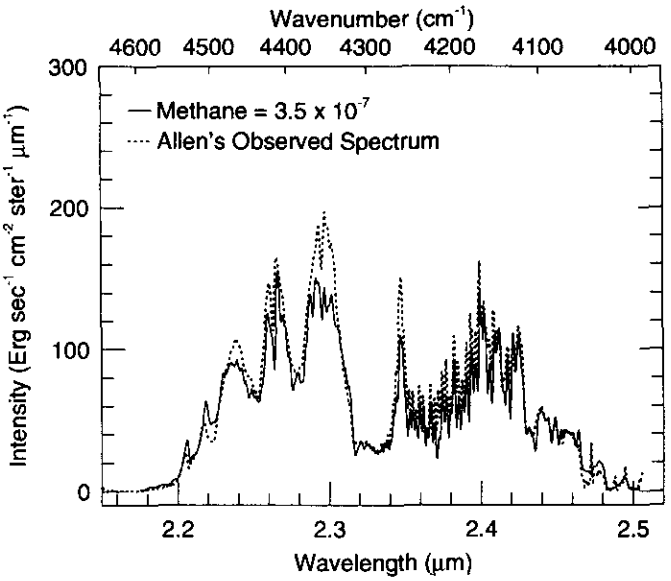

FIG. 15. A comparison of a synthetic spectrum containing 0.35 ppm CH_4 and the observed spectrum for the 2.3-μm window.

1.73 μm, where CO_2 is the dominant source of gaseous opacity. In this manner, we obtained a value of 25.0 for τ_{ref}. (This value is our final value that was obtained by tweaking slightly the initial value to take into account the small effect of the continuum opacity on the mean intensities between 1.715 and 1.73 μm.) Figure 11b shows the sensitivity of our optimized model for the 1.7-μm window to variations of $\pm 10\%$ in this value for τ. Based on this figure and the estimated uncertainty in the absolute intensities of the measurements, we assign a formal error of $\pm 5\%$ to the inferred value for τ.

Next, we iteratively fitted the remainder of the spectrum to derive values for the continuum coefficient and the mixing ratios of H_2O and HCl. Unfortunately, the CO_2-dominated portions of this window lie in a more opaque part of the window, making it difficult to infer the continuum coefficient from this region. We found that it was not possible to fit the observed spectrum between 1.73 and 1.75 μm without invoking continuum opacity. More precisely, it was not possible to fit simultaneously both the DC and the AC components of this portion of the spectrum with any physically plausible pair of mixing ratio profiles for HCl and H_2O when $k_{con} = 0$. Our best fit value for the wavelength-independent continuum coefficient is 7×10^{-9} cm^{-1} amagat^{-2}.

Figures 17a and 17b show the sensitivity of the computed spectra to variations of a factor of 2 in the best fit values of the H_2O and HCl mixing ratios in the sensing regions, respectively. To first order, the spectral domain, which is sensitive to these two gases, is quite similar. However, on close inspection of these figures, it is clear that there is some separability. For example, the intensity peak located at 1.746 μm and its long wavelength wing are much more sensitive to H_2O than to HCl. Conversely, the AC amplitudes between 1.734 and 1.746 μm are much more sensitive to HCl than to H_2O. Figure 17c shows a comparison between the observed spectrum and that for our best fit model. This model is characterized by constant mixing ratios of H_2O and HCl in the sensing regions. The best fit value for H_2O is 30 ± 7.5 ppm at an altitude of 23.5 km and this value for HCl is 0.48 ± 0.12 ppm at an altitude of 23.5 km. These error bars were conservatively estimated from a combination of measurement uncertainties, the sensitivity of the spectrum to each of these two gases separately, the degree of overlap of the spectral regions that are sensitive to them, and errors in the spectral databases.

5.4. *Simulations of the 1.2-μm Window Complex*

As illustrated in Fig. 4c, the observed low-resolution spectra of the 1.2-μm region show four narrow windows centered at approximately 1.10, 1.18, 1.275, and 1.31 μm. The subpeak on the short-wavelength side of the 1.275-μm feature is dominated by an O_2 airglow emission band (Crisp *et al.* 1991a). The airglow contributes much of the observed emission on the short-wavelength side of the main peak, whereas thermal emission is the dominant source of emission at the main peak and on its long-wavelength side. According to Fig. 7, CO_2 is the controlling source of opacity for the thermal emission in the 1.27- and 1.31-μm windows, as well as the key source of opacity on the long-wavelength side of the 1.18-μm feature and the short-wavelength side of the 1.10-μm feature, whereas H_2O is the major source of opacity on the other sides of these last two features.

Our first step in the fitting process is to determine the value of the cloud optical depth. Normally, we would do this by matching the DC levels of the 1.275- and 1.31-μm features, with appropriate allowance for the airglow contribution. (It is about 10% at the main peak of the 1.275-μm feature of Fig. 4c, as found by using the slightly shorter wavelength subpeak that is almost entirely due to airglow to scale unpublished airglow spectra by Bezard and deBergh). However, we found that when we did this we got unreasonable results: The cloud optical depth at the reference wavelength was found to be extremely small—$\tau_{ref} = 9.4$; the H_2O mixing ratio in the bottom 25 km of the atmosphere, which was derived by fitting the 1.10-μm window, was found to be extremely large—$\alpha = 180$ ppm—in comparison to the values we obtained from the longer wavelength windows; and, of greatest importance, the spectral shapes of the 1.10- and 1.18-μm features were very poorly simulated (cf., Fig. 18a).

We, therefore, have derived τ_{ref} instead by matching

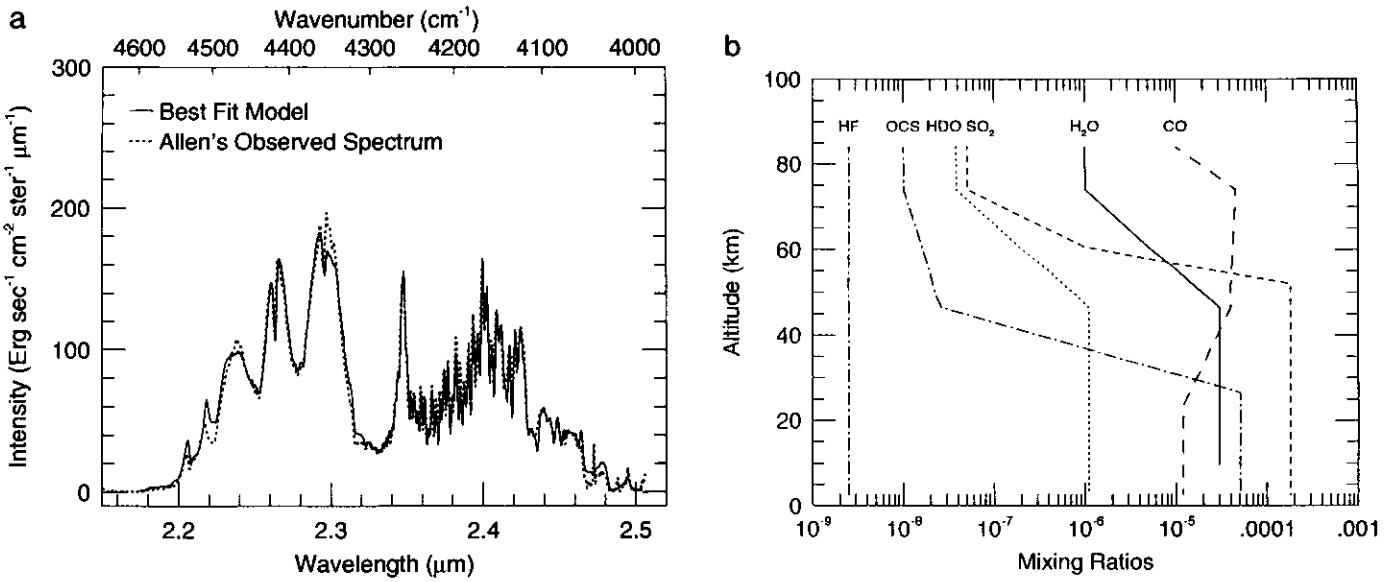

FIG. 16. (a) A comparison of the best fit model for the 2.3-μm window and the observed spectrum; (b) gas mixing ratio profiles used to construct the best fit models for all the windows.

the DC amplitude of the low-wavelength portion of spectrum of the 2.3-μm window that was obtained on the same night and at the same place as the spectrum of the 1.2-μm window complex (cf., Fig. 4d). We obtained a value for τ_{ref} equal to 25.0. Now, however, the computed intensities in the 1.27- and 1.31-μm windows are too low by about a factor of two (cf., Fig. 18b and the discussion in the next section of the paper).

To obtain a consistent fit to the 1.10- and 1.18-μm features, it was necessary to make several adjustments to the opacity in the vicinity of the 1.18-μm feature. First, we needed to increase the χ factor to match well the long-wavelength portion of this window that is controlled by the far wings of lines in the 8294-cm^{-1} band of CO_2 that lies just outside this window. We found that altering the constant in the exponent of the equation for χ beyond 10 cm^{-1} from 47 to 90 cm^{-1} and increasing the cutoff from 120 to 160 cm^{-1} led to a good fit to the long-wavelength side of the 1.18-μm window. This same χ factor was used throughout the 1.2-μm window complex, although it was important only at this one location. (cf., Fig. 7—only at this location does the CO_2 opacity decline very steeply in a place where H_2O opacity is unimportant.) We also needed to introduce a wavelength-independent continuum to match the peak intensity of the 1.18-μm feature at the same time that we were matching the peak intensity of the 1.10-μm feature. We found that $k_{con} = 1.7 \times 10^{-10}$ cm^{-1} amagat^{-2}. We note, however, that this determination of k_{con} is weak in that only the peak intensity at 1.18 μm was used to find it, rather than employing the more desirable procedure of fitting the shape of a CO_2 dominated region, as was done for the spectrum of the 2.3-μm window.

We constrained the H_2O profile in the bottom portion of Venus' atmosphere (0–20 km) by matching the 1.10-μm feature. First, we tried a constant H_2O mixing ratio of 30 ppm, based on the value derived at higher altitudes from the spectra for the 1.7- and 2.3-μm windows. The synthetic spectrum provided a close match to the observed spectrum, but its peak intensity was slightly too low (cf., Fig. 18b). This result suggested that we consider profiles in which the H_2O mixing ratio declines with decreasing altitude below some reference altitude, above which it has a constant value of 30 ppm. As illustrated in Figs. 18c and 18d, slightly better fits to the 1.10-μm window can be achieved alternatively by choosing the reference altitude as 20.5 km and setting the H_2O mixing ratio equal to 20 ppm at the surface (with a linear decline with altitude between the reference altitude and the surface) or by choicing the reference altitude as 10.5 km and setting the H_2O mixing ratio equal to 5 ppm at the surface. Clearly, there is a whole family of possible solutions.

This result prompted us to examine the ability of the H_2O profile derived from the Pioneer Venus mass spectrometer experiment to match the 1.10-μm feature (Donahue and Hodges, 1992). This profile is characterized by a constant H_2O mixing ratio of 67 ppm from 24 km (where the mass spectrometer became unplugged) to 10 km, below which α declined by a factor of 4 to the surface. The solid curve in Fig. 18e shows this profile. We assumed that the H_2O mixing ratio remains constant above 24 km to 48 km, above which it declines in accord

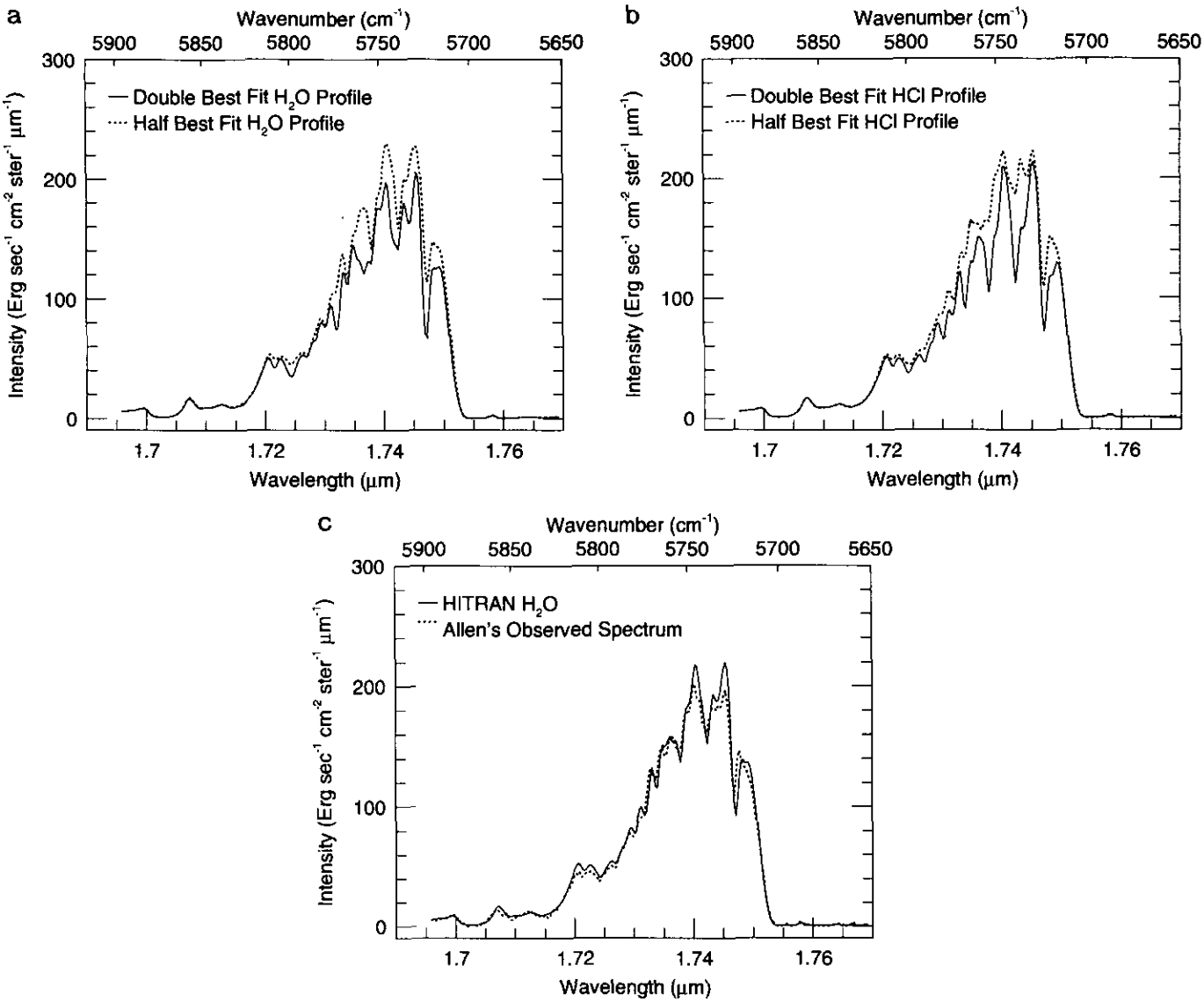

FIG. 17. Sensitivity of the synthetic spectra for the 1.7-μm window to multiplying the best fit mixing ratio profiles of two gas species alternately by factors of 0.5 and 2.0. (a) H_2O; (b) HCl; (c) a comparison of the best fit model for the 1.7-μm window and the observed spectrum.

with mass spectrometer data within the clouds. (The extension of the H_2O profile above 24 km has very little impact on our simulations). Figure 18f shows the result of using this "profile A" in our simulations. The predicted intensities are systematically too low within the 1.10-μm window. However, a much more satisfactory fit can be achieved by scaling the mass spectrometer profile by a constant factor so that α = 30 ppm above 10 km, as suggested by our fits to the longer wavelength windows. The scaled profile is profile B in Fig. 18e and the resulting synthetic spectrum is shown in Fig. 18f. This scaled profile provides a very good fit to the observed 1.10-μm feature. Donahue and Hodges (1992) state that the shape of their derived H_2O profile is much less uncertain than the absolute abundances, since the latter is adversely affected by calibration uncertainties and uncertainties in the abundance of argon.

According to the simulations shown in Fig. 18, optimum fits to the 1.10-μm window are obtained with water vapor mixing ratios that decrease toward the surface in the lowest portion of the atmosphere. This result is very fragile since the simulation with a constant water vapor mixing ratio of 30 ppm only slightly underestimates the peak intensity in this window. Indeed, this difference is well within the uncertainties of our modeling, as well as those of the observations. Furthermore, this constant profile gives the best fit when the emission angle is altered from its nominal value of 35° to a value of 25°, which lies at

the extreme end of likely viewing angles. (Unfortunately, in contrast to the higher resolution spectra taken in the longer wavelength windows, the observing geometry of the lower resolution spectra of Crisp *et al.* (1991) was not well determined at the time of the observations.) We, therefore, conclude that the H_2O mixing ratio has a value of 30 ppm between 10 and 25 km, whereas its value at altitudes below about 10 km is not well-constrained by the spectra of the 1.2-μm window complex analyzed in this paper.

Our difficulty in constraining the water vapor mixing ratio below an altitude of 10 km may stem from an intrinsic limitation of the information content of the nightside thermal emission spectra, rather than our use of this particular dataset. The sensitivity function for H_2O at the peak of the 1.10-μm window displays a peak sensitivity at an altitude of 12 km and a marked falloff toward the surface below 7.5 km (cf., Fig. 9a). The physical reason for the falloff is that the atmospheric temperature approaches that of the surface as the altitude decreases to 0 and hence the thermal contrast between a given atmospheric layer and the surface tends to become progressively smaller as the surface is approached. Conceivably, somewhat greater sensitivities close to the surface may be realized when allowance is made for the emissivity of the surface being less than unity (the smaller, the better).

Finally, we comment on the marked difference in fits to the spectral shapes of the 1.10- and 1.18-μm windows that were obtained when we alternately used the 1.27/1.31-μm features and the shorter wavelength portion of the 2.3-μm window to determine τ_{ref} (cf., Fig. 18a with Figs. 18b–18d). As noted earlier, the short-wavelength portion of the 1.10-μm and the long-wavelength portion of the 1.18-μm windows are controlled by CO_2 opacity, whereas their opposite sides are controlled by H_2O opacity. Thus, adjusting the H_2O abundance and k_{con} to match the observed peak intensities of the 1.10- and 1.18-μm features provides no guarantee that the spectral shapes of these features will be well simulated. The much improved fits to these shapes that result when the 2.3-μm spectrum is used to find τ_{ref} lends added credence to this choice and the approximate validity of the H_2O abundances obtained with this choice.

5.5. *Simulations with Other Databases*

In this subsection, we examine the ability of synthetic spectra generated with databases that were not used in our standard opacity database to match the observed spectra and, in the more successful cases, their impact on the derived gas mixing ratios. Below, we successively evaluate the HITRAN '91 databases for CO_2, the high-T database for H_2O, and the H_2O–CO_2 continuum database.

Figures 19a–19c show synthetic spectra generated for the 2.3-, 1.7-, and 1.2-μm windows by substituting the HITRAN '91 database for CO_2 in place of the high-T CO_2 database, but otherwise retaining the other databases of our standard opacity database and by using the optimum set of k_{con}, τ, and α that were derived in the previous subsection. The synthetic spectra grossly disagree with the observed spectra (cf., Figs. 4a–4c) between 2.15 and 2.30 μm in the 2.3-μm window and throughout almost the entire extent of the 1.7- and 1.2-μm windows. These discrepancies cannot be repaired in any obvious manner by picking alternative sets of parameters. We conclude that the high-T database for CO_2 represents a major and essential improvement over the HITRAN '91 database. This conclusion is not meant in any way to denigrate the HITRAN '91 database: it simply was not constructed for application to Venus' atmosphere.

We next consider what happens when the very preliminary high-T database for H_2O is substituted for the HITRAN '91 database for H_2O. We found that there was little change to the synthetic spectra for the 1.2- and 2.3-μm windows, but that a nontrivial change did occur for the 1.7-μm window. We, therefore, refit the 1.7-μm region to achieve a new optimum match to the data. Figure 20 shows this fit. The values of τ and the H_2O abundance remain unchanged from the values obtained with the standard database, but the HCl mixing ratio is reduced by 25% to a value of 0.36 ppm and the continuum coefficient is increased by slightly less than 10% to 7.5×10^{-9} cm^{-1} amagat^{-2}.

Comparing Fig. 20 with Fig. 17, we see that the AC amplitudes between 1.70 and 1.76 μm are somewhat better fit with the high-T H_2O opacities, but that there is a noticeable wavelength shift in the positions of local minima and maxima in the new synthetic spectra relative to their

FIG. 18. Synthetic spectra and H_2O mixing ratios for the 1.2-μm window complex. Comparisons between synthetic spectra and the observed spectrum: (a) The cloud optical depth at the reference wavelength, τ_{ref}, was derived by matching the peak of the 1.27-μm window, with allowance for the small contribution from O_2 airglow. A constant value of 180 ppm has been used for the water vapor mixing ratio, α, from the just below the clouds to the surface. In all the remaining figures, τ_{ref} was found by fitting the short-wavelength portion of a spectrum of the 2.3-μm window obtained on the same night and for the same spot as that of the 1.2-μm spectrum. (b) α = 30 ppm from just below the clouds to the surface; (c) α = 30 ppm above 20.5 km, whereas below this reference altitude α linearly decreases to 20 ppm at the surface; (d) α = 30 ppm above 10.5 km, and linearly decreases to 5 ppm at the surface; (e) two alternative profiles derived from the Pioneer mass spectrometer experiment. See the text: (f) a comparison of synthetic spectra and the observed spectrum for the profiles of (e).

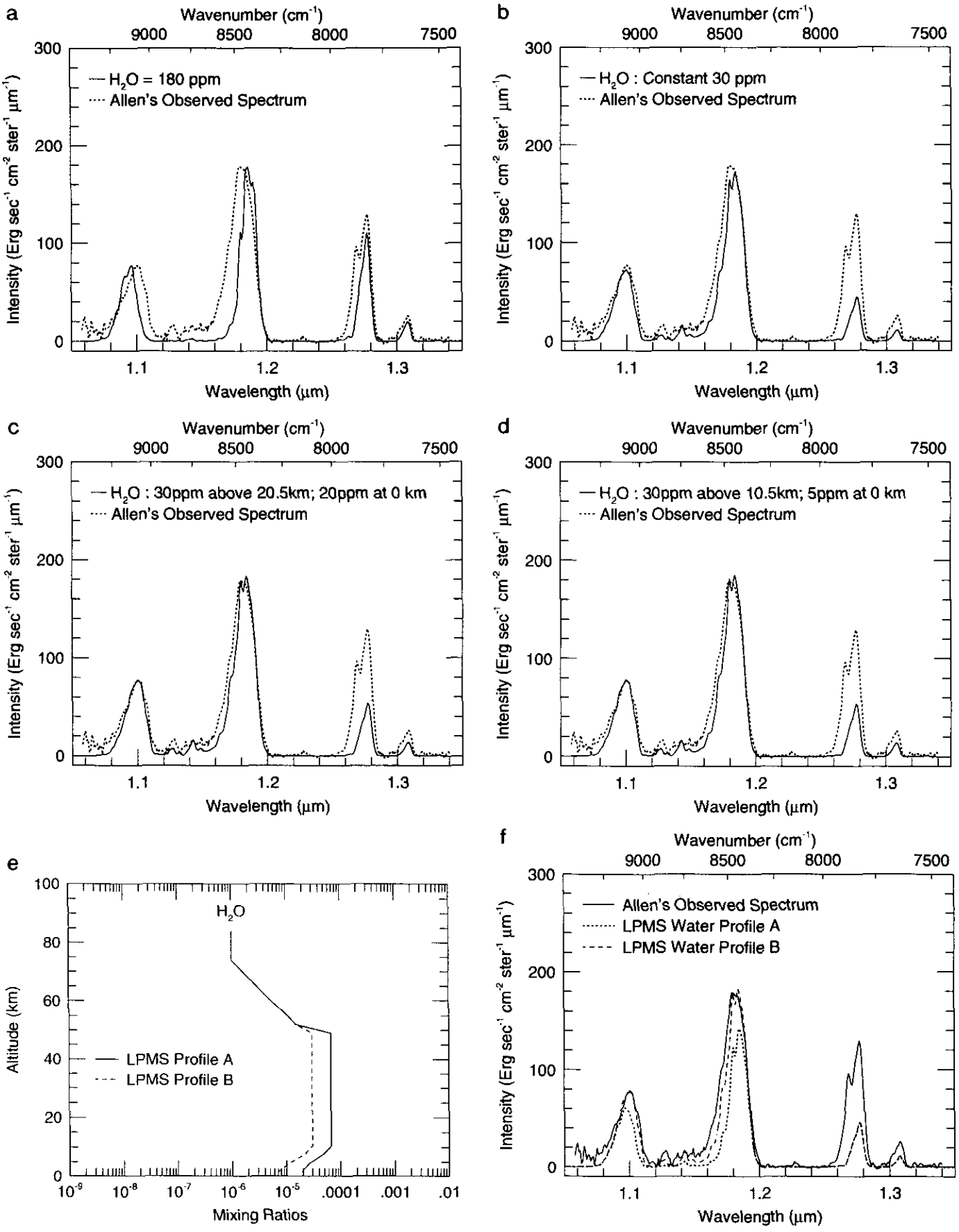
a
Wavenumber (cm^{-1})
9000 8500 8000 7500
H_2O = 180 ppm
Allen's Observed Spectrum
Intensity (Erg sec^{-1} cm^{-2} ster^{-1} μm^{-1})
Wavelength (μm)
b
H_2O : Constant 30 ppm
Allen's Observed Spectrum
c
H_2O : 30ppm above 20.5km; 20ppm at 0 km
Allen's Observed Spectrum
d
H_2O : 30ppm above 10.5km; 5ppm at 0 km
Allen's Observed Spectrum
e
H_2O
LPMS Profile A
LPMS Profile B
Altitude (km)
Mixing Ratios
f
Allen's Observed Spectrum
LPMS Water Profile A
LPMS Water Profile B

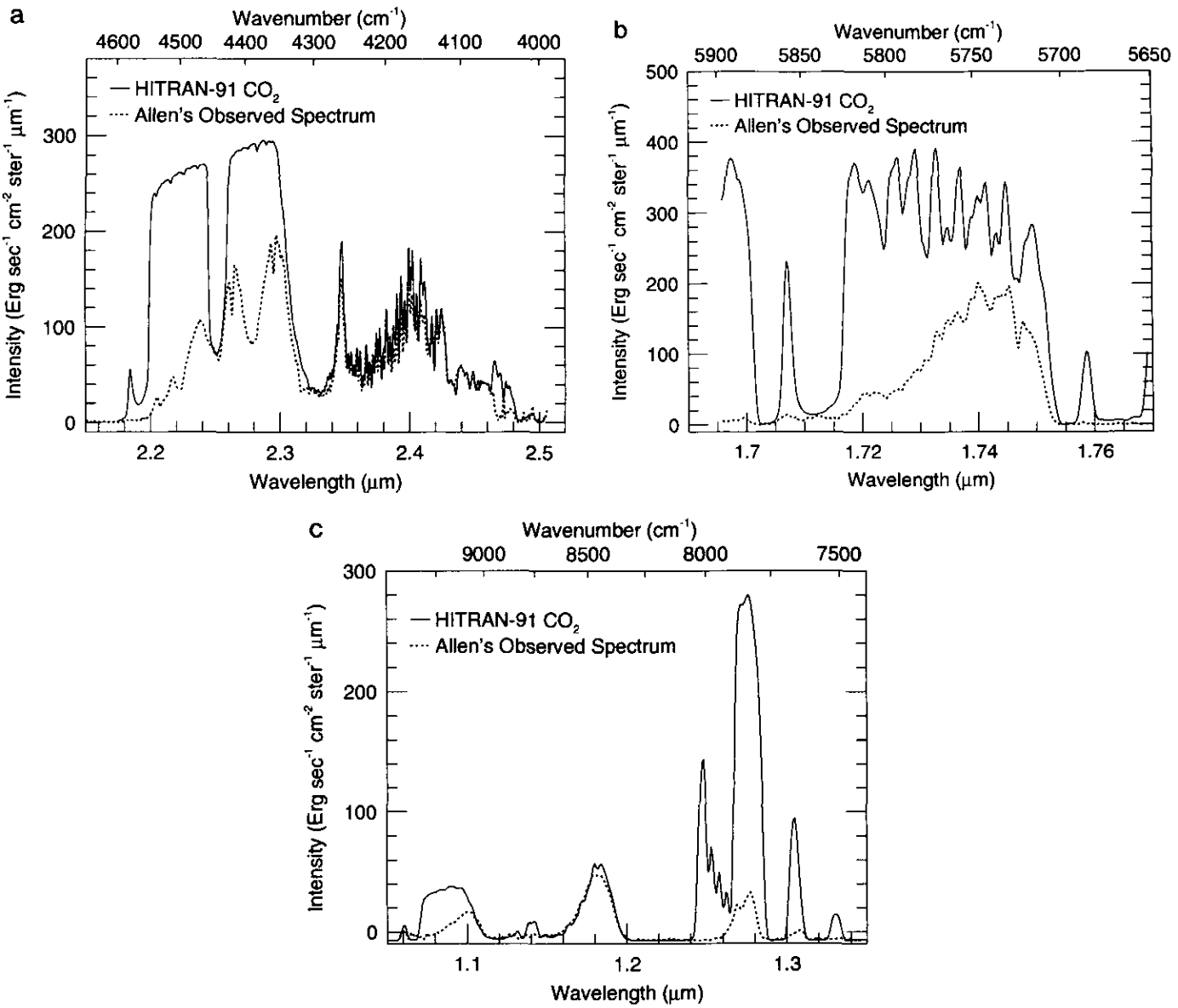

FIG. 19. Comparisons between synthetic spectra produced with the HITRAN line parameters for CO_2 and the observed spectra in the various window regions. Best fit parameters derived from the comparisons with the high-temperature CO_2 database have been used in calculating the synthetic spectra; i.e., no attempt has been made to optimize the match. (a) 2.3-μm window; (b) 1.7-μm window; (c) 1.2-μm window complex.

locations in both the observations and the synthetic spectra generated with the HITRAN '91 H_2O opacities. This shift illustrates the preliminary nature of the high-T database for H_2O and is the reason that we did not include it in the standard set of opacities.

We next consider the impact on our simulations of including H_2O–CO_2 continuum opacity together with our standard opacity database. Figure 21a shows what happens to our best fit model for the 2.3-μm window when this continuum opacity is turned on. Quite clearly, it has a major impact across almost the entire window region. We have varied the values of k_{con}, τ, and α to obtain as good a fit as possible. In fact, we were able to obtain quite a good fit to the observations, as is illustrated in Fig. 21b. The mixing ratios that produced this good fit are shown in Fig. 21c.

The good fit to the observed 2.3-μm spectrum was achieved principally by substantially decreasing the water vapor mixing ratio in the sensing region and introducing a slope to it. In particular, the water vapor mixing ratio has a value of 6 ppm and a gradient, $d\alpha/dz$, of -0.40 ppm/km at an altitude of 33 km. This water vapor profile may be contrasted with a constant water vapor mixing ratio of 30 ppm that was derived when the H_2O–CO_2

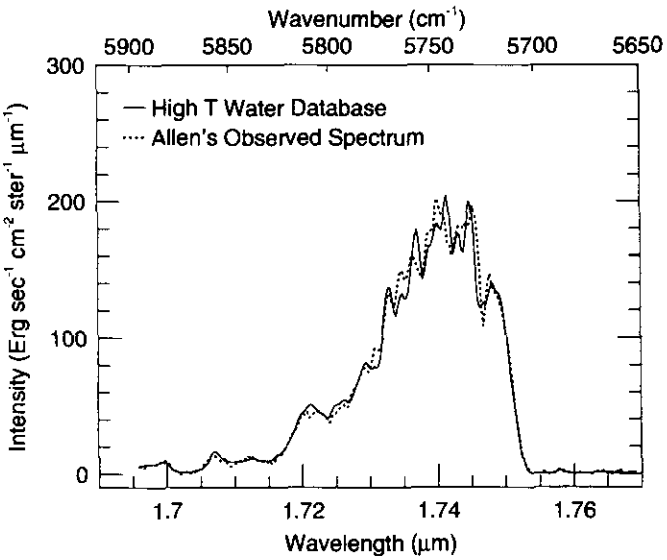

FIG. 20. A comparison between a best fit synthetic spectrum calculated with the high-temperature database for H_2O and the observed spectrum for the 1.7-μm window.

continuum was ignored. By decreasing substantially the H_2O mixing ratio from the baseline value, we greatly reduce its impact at wavelengths shortward of 2.3 μm. Thus, the new, best fit value of k_{con}, 2.3×10^{-8} cm^{-1} amagat^{-2}, is only slightly smaller than the baseline value of 2.5×10^{-8} cm^{-1} amagat^{-2} and the new best fit value of τ_{ref}, 25.8, is the same as that for the baseline model. The large decrease in the H_2O abundance also lessens the impact of the H_2O–CO_2 continuum at wavelengths longward of 2.3 μm, making it easier to match the AC and DC levels here. By introducing a positive slope to the water vapor mixing ratio across the sensing region (α decreases with decreasing altitude), we were able to enhance somewhat the AC level of the H_2O dominated portion of the window, thereby simultaneously fitting the AC and DC levels there.

In obtaining the new best fit of Fig. 21b, we did not need to change the mixing ratio profiles of OCS and SO_2, we needed to slightly modify the profile of CO, and we substantially altered α for HF. In particular, α and $d\alpha/dz$ for CO now have values of 29 and 0.90 ppm/km, respectively, at an altitude of 36 km, rather than values of 23 and 1.20 ppm/km. For HF, α is now 0.0075 rather than 0.0025 ppm.

The H_2O–CO_2 continuum opacity also had a significant impact on the theoretical spectra for the 1.7-μm window. Figure 22a shows an optimum fit that was achieved when the water vapor mixing ratio was assumed to be constant across the sensing region. We used an α of 35 ppm for H_2O to generate this spectrum, which may be compared with a value of 30 ppm for the baseline model. In addition, α for HCl, k_{con}, and τ_{ref} now have values of 0.36 ppm, 3.0×10^{-9} cm^{-1} amagat^{-2}, and 25.8, respectively. The corresponding values for the baseline model are 0.48 ppm, 7×10^{-9}, and 25.0.

We also examined the ability of the H_2O mixing ratio profile derived from the 2.3-μm spectrum (cf., Fig. 21c) to produce an acceptable fit to the 1.7-μm data. Figure 22b shows the results of these efforts. For this model, the HCl mixing ratio remains at 0.36 ppm, τ remains at 25.8, and k_{con} increases to 7.0×10^{-9} cm^{-1} amagat^{-2}, the same value as was found in the fit without the H_2O–CO_2 continuum.

Finally, we found that the H_2O–CO_2 continuum had little effect in the 1.2-μm window complex.

The above analysis shows that the H_2O–CO_2 continuum has a major impact on the 1.7- and 2.3-μm windows. Its use results in a major alteration to the H_2O vapor mixing ratio in the sensing regions (cf., Figs. 16b and 21c). Its use also produces negligible to minor changes in the abundances of most other gases and a major change in the HF abundance. We did not include this opacity in our standard set of opacities because of the sizeable uncertainty in the continuum coefficients.

Is it possible to distinguish between the two limiting cases of no H_2O–CO_2 continuum and the nominal set of coefficients for this continuum? At first glance, it seems difficult to do so on the basis of the best fits to the observed spectra: compare Figs. 14 and 21b and 17c and 22b. However, upon careful examination, we find that the baseline model produces a better fit to the 1.7-μm spectrum than does the model with the H_2O–CO_2 continuum opacity. In the latter fit, the synthetic spectrum fails to show some of the detail that the observed spectrum and the synthetic spectrum for the no-H_2O–CO_2 continuum fit do. For example, the 1.732-μm absorption feature in the observed spectrum is almost totally missing in the synthetic spectrum with the continuum turned on. Similarly, this synthetic spectrum seems more washed out than the observed spectrum between 1.734 and 1.746 μm. In addition, it is difficult to understand why the water vapor mixing ratio should decrease in the altitude range from 47 to 30 km. Finally, the H_2O profile inferred for the case with H_2O–CO_2 continuum appears to be incompatible with other estimates of the H_2O mixing ratio (e.g., Donahue and Hodges 1992a,b; cf., Table III). We conclude that the baseline model is the more realistic one. However, it will be important to derive more accurate values for the H_2O–CO_2 continuum in the future.

6. DISCUSSION

6.1. *Implications for Databases*

There is no question that the HITRAN database for the permitted transitions of CO_2 is inadequate for application to the near-infrared nightside emission spectra of Venus.

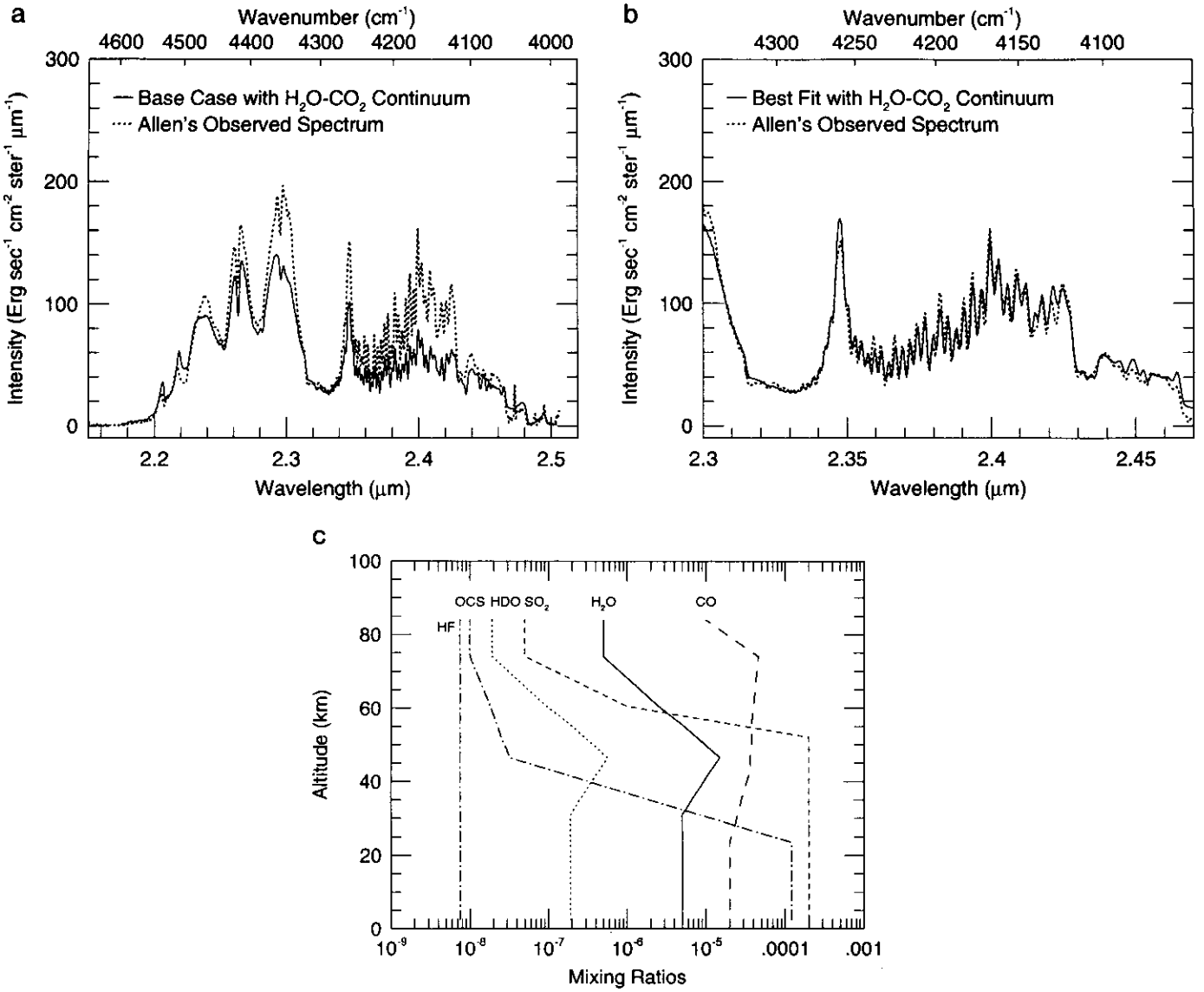

FIG. 21. Synthetic spectra for the 2.3-μm window and optimized mixing ratio profiles when the H_2O–CO_2 continuum opacity of Ma and Tipping (1992b) is used. (a) A comparison of the synthetic spectrum calculated with the best fit parameters obtained with no H_2O–CO_2 continuum and the observed spectrum; (b) a similar comparison to (a) when the parameters are reoptimized; (c) gas mixing ratio profiles for the best fit case of (b).

The employment of the high-T database of CO_2 that has been developed by Wattson represents an indispensible step toward obtaining quantitative fits to the observed spectra, thereby making it possible to derive information about gas mixing ratios and cloud radiative properties from these observations. As shown in Figs. 16a and 17c, very good, if not perfect, fits can be obtained to spectra of the 2.3- and 1.7-μm windows when the high-T database for CO_2 is used in conjunction with databases for other gases that absorb in these regions. However, even this database has problems in the 1.2-μm window complex: More specifically, it produces too much opacity for the 1.27- and 1.31-μm features, resulting in the synthetic spectrum having too low a peak intensity at the position of these features. We suspect that this problem arises chiefly from the lack of adequate laboratory constraints on the potential energy surface and dipole moment function for bands in this wavelength region. This problem could be resolved by laboratory measurements of several CO_2 bands in the 1.20–1.35-μm domain.

Because all other gas species that absorb in the near-infrared window regions have mixing ratios that are several to many orders of magnitude smaller than that of CO_2, there is less of a need to develop high-temperature

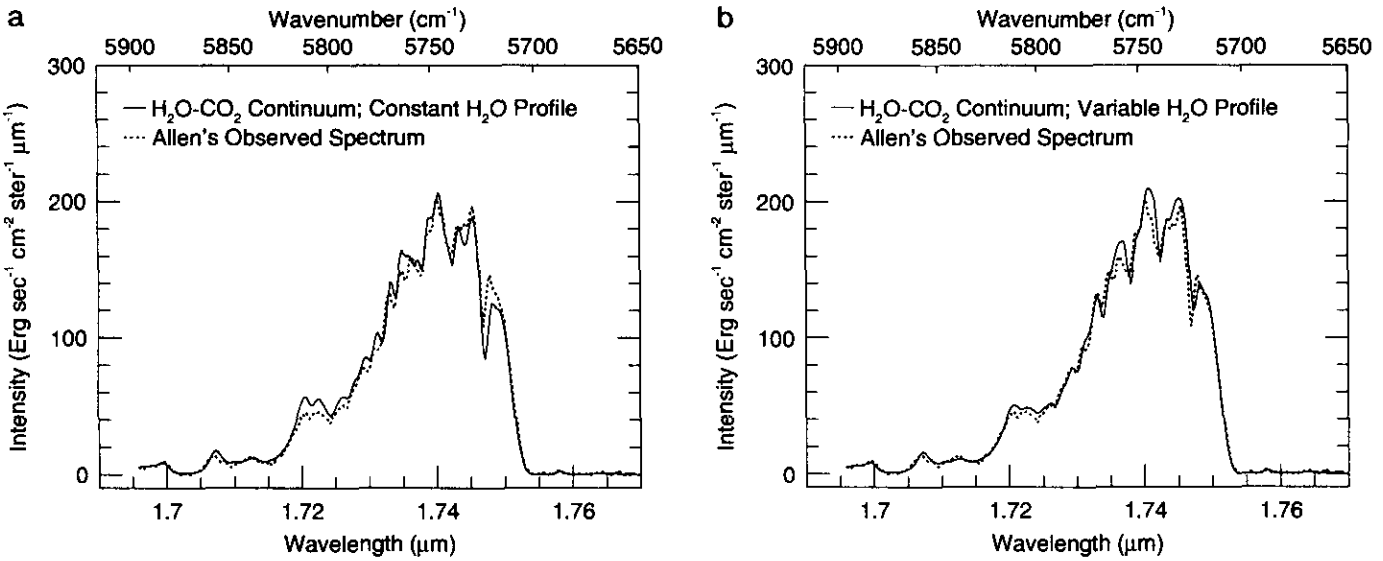

FIG. 22. Comparison of best fit synthetic spectra for the 1.7-μm window with the H_2O–CO_2 continuum turned on and the observed spectrum. (a) The H_2O mixing ratio, α, is assumed to be constant in the sensing region of this window; (b) α is allowed to vary across the sensing region.

databases for them, i.e., to include their hotbands. A likely exception to this statement is H_2O. We have found that a preliminary high-T database for H_2O produces a nonnegligible change to the synthetic spectrum for the 1.7-μm window. Improvements in the accuracy of this new database would be highly desirable. We also need to take into account the hot bands of any gas whose abundance we want to determine precisely, if it has a low-energy vibrational mode (which will give rise to hot bands). This is the case for OCS, which has $v_2 = 521$ cm^{-1} (and to a lesser extent $v_1 = 859\,cm^{-1}$). For example, the transition from v_2 to $2v_3 + v_2$ has an intensity that is not much smaller than that of the $2v_3$ fundamental that begins at the ground state. In deriving the band intensities of this fundamental and its closely associated hot bands, we were forced to assume that they differed simply by Boltzmann factors, since laboratory data were available only for their summed intensity. It would be useful to have measurements of the individual band intensities, something that can easily be done with modern laboratory spectrometers.

In addition, it will be important to include HDO in these calculations, something that can readily be handled by DND theory: Since the abundance of HDO in Venus' atmosphere is about 4% that of H_2O and since its bands are displaced significantly in wavelength from their main isotope counterparts, inclusion of HDO opacity in databases for Venus is important. For example, HDO bands that are centered near 4100 cm^{-1} contribute significant opacity in the 2.3-μm window. However, there are no HDO bands tabulated in the HITRAN database at wavelengths shortward of 2.30 μm, although higher overtone and combination bands of HDO occur at shorter wavelengths and some of these may have strengths and positions that are relevant for the shorter wavelength windows.

Finally, we point out the need to derive from a combination of theory and observation the half-widths of H_2O being broadened by CO_2. Unfortunately, we have had to use half-widths for broadening by N_2 that have been augmented by a scale factor based on old laboraotry measurements. It is possible to substantially improve this situation. A direct knowledge of the half-widths of H_2O being broadened by CO_2 as a function of several quantum mechanical rotational numbers at temperatures ranging from room temperature to 750 K is essential for deriving accurate H_2O abundances from spectra of the various windows.

There is also a paucity of data available on bands of some key gases for window regions aside from the 2.3-μm window. Gases that fall in this category include OCS and SO_2. New laboratory measurements of bands of these molecules that lie in the 1–2-μm region would be highly desirable.

Perhaps the biggest problem with the current database involves continuum sources of opacity. We have had to postulate the presence of a continuum opacity that is independent of wavelength in three of the window regions, 2.3, 1.7, and 1.18 μm, to obtain good fits to the observed spectra in these regions. We suspect that this continuum is produced largely by a combination of the far wings of strong CO_2 lines that lie outside, but adjacent to, the

windows and pressure-induced transitions of CO_2 that lie within the window regions. Observational support for the presence of such opacity has been given by laboratory measurements obtained at room temperature (Brodbeck *et al.*, 1991). Clearly, there is a need for extending such high-pressure measurements to shorter wavelengths and higher temperatures, a difficult, but realizable undertaking.

Inclusion of continuum opacity of H_2O–CO_2, based on the calculations of Ma and Tipping (1992a,b), shows that it can have a major impact on synthetic spectra for the 2.3- and 1.7-μm windows (cf., Figs. 21 and 22). Use of the current set of continuum coefficients for H_2O–CO_2 results in a major reduction in the water vapor mixing ratios deduced from spectra of these two windows. We have argued that these coefficients are likely to be too large. As stated earlier, they could be in error by as much as an order of magnitude. This situation could be improved significantly by obtaining laboratory data on this continuum opacity in the 1–2.5-μm region *or* any other suitable spectral region (e.g., the 7–12-μm region). These data need not be complete in themselves: measurements in limited sections of a spectral region and/or at restricted ranges of temperatures would provide powerful constraints on the theory of Ma and Tipping, permitting them to generate much more accurate coefficients for H_2O–CO_2 continuum opacity for the full set of conditions of interest. In this regard, the theory of Ma and Tipping has an analogous relationship to data that the DND theory of Wattson has.

6.2. *Implications for Cloud Properties and Gas Abundances*

In this subsection, we first briefly discuss the cloud properties that we have derived from the spectra of Crisp *et al.* (1991a) and then discuss at greater length the inferred gas mixing ratios. In fitting the spectra of the three window regions, we derived values for the cloud optical depth at a reference wavelength of 0.63 μm. It is an interesting curiosity that the values for τ are remarkably similar. In particular, we obtained values of 25.8, 25.0, and 25.0 when analyzing spectra for the 2.3-, 1.7-, and 1.2-μm windows. (A low-resolution spectrum of the 2.3-μm window was used to find τ_{ref} in this last case). These values, therefore, may represent typical values for bright spots and conceivably they hint at some lower bound on cloud opacity. However, a much larger number of spatial points needs to be examined before any firm conclusions can be drawn about these matters. These values are comparable to, but slightly smaller than values of τ inferred from analysis of near-infrared spectra of the dayside of Venus (Pollack *et al.* 1978) and from analysis of measurements made from the Pioneer Venus Large Probe (Knollenberg and Hunten 1980, Tomasko 1983, Crisp 1986), as expected since we are sampling places of reduced opacity.

TABLE IV
Gas Mixing Ratios Derived in this Paper

Gas	Mixing ratio (ppm)	Gradient[a] (ppm/km)	Altitude[b] (km)	Pressure (bar)	Temperature (K)	Width[c] (km)
SO_2	180 ± 70		42	2.80	404	37–52
OCS	4.4 ± 1.0	−1.58 ± 0.30	33	7.21	472	26–39
HCl	0.48 ± 0.12		23.5	16.4	548	13–34
HF	0.001–0.005		33.5	6.87	468	25–46
CO	23 ± 5	+1.20 ± 0.45	36	5.35	448	23–46
H_2O	30 ± 6		33	7.21	472	23–47
	30 ± 7.5		23.5	16.4	548	14–35
	30 ± 10		12	41.1	643	5–19
	3.5–15[d]		0	92.1	735	
CH_4	<0.1		30			24–44
	<2.0		24			17–27

[a] The gradient of the mixing ratio, α, is defined as $d\alpha/dz$. Note that we employ mixing ratio profiles for which $\ln(\alpha)$, but *not* α, varies linearly with altitude over the sensing region. The slope of the $\ln(\alpha)$ curve equals $\alpha^{-1} \times d\alpha/dz$, as given in this table.

[b] The altitude, pressure, and temperature values refer to the midpoint of the sensing region, as derived from the average of the peak sensitivities for the maximum and minimum intensities for a given gas species and spectral region. See text.

[c] The width of the sensing region is derived from the altitudes at which the sensitivity is half the peak sensitivity. The low-altitude boundary was found from the sensitivity function for the maximum intensity and the high-altitude boundary was found from the sensitivity function for the minimum intensity. See text.

[d] Profile B of Fig. 18e.

Table IV summarizes the values of the gas mixing ratios that we derived in the sensing regions of the various windows. It is straightforward to assign error bars to these mixing ratios, α, based on our sensitivity studies (e.g., Fig. 12). However, the real errors may be set by inadequacies in our standard database of gas opacities. Estimating these real errors is a much more difficult proposition. However, some good insight into this matter is provided by the simulations we performed when the nominal values for the H_2O–CO_2 continuum opacity were included in our simulations. This continuum opacity produces substantial opacity in both the 2.3- and the 1.7-μm windows (e.g., Fig. 20a). The addition of this opacity source led to little change in the gas mixing ratios inferred for some species and larger changes to others in a way that could be anticipated from both our earlier sensitivity experiments and the nature of the continuum. In particular, no readily discernable change occurred to the OCS and SO_2 mixing ratios (probably because they are located in regions dominated by the permitted transitions of CO_2); α for HCl decreased by 25%; α for CO at the midpoint of the sensing region increased by 20%, whereas its slope decreased by about 45%; α for HF increased by a factor of 3; and α for H_2O decreased substantially—by about a factor of 3 at the midpoint of the sensing region for the 2.3-μm window, with there being a need to have a declining α with declining altitude for this window.

One of the big surprises of our analysis was the ability

to determine the vertical gradient of α for several gas species, in addition to its mean value within the sensing region of a given window. Here, we provide a physical explanation for this result. Consider the situation in which there is a substantial AC component to a spectral region dominated by a given gas species, i.e., there is a significant variation in the brightness temperature in this region, due for example to the rotational structure of one of its bands or to a variation in strength among several closely situated bands of that species. At a given wavelength, the thermal emission arises from a region of the lower atmosphere centered near a slant path optical depth unity, $\tau_g = 1$. When a given gas species, i, dominates the opacity at the wavelength, j, of interest, $\tau_g = k_{ij}\Sigma_{ij}$, where k_{ij} is its monochromatic opacity and Σ_{ij} is the number of molecules of species i along the slant path above slant path optical depth unity. Therefore, the ratio of the column abundances of gas molecules of species i above the centroids of emission for a pair of wavelengths 1 and 2 is simply given by:

$$\Sigma_{i1}/\Sigma_{i2} = k_{i2}/k_{i1}. \quad (6)$$

If α_i increases with decreasing altitude within the sensing region, then the vertical separation needed to achieve a given ratio of Σ_i will be smaller than if α_i is constant across the sensing region. Therefore, a negative value for $d(\ln(\alpha))/dz$ implies that there will be a smaller difference in brightness temperatures and a smaller change in the observed intensities between the pair of wavelengths than if this gradient were zero. We needed to introduce a strong negative slope in the OCS mixing ratio profile to fit the modest AC variations produced by OCS opacity near 2.44 μm, while at the same time fitting the DC amplitude there. (The DC amplitude determines the average value of α in the sensing region.) Conversely, having a positive slope in α leads to larger AC amplitudes. Our fit to the CO-dominated portion of the 2.3-μm window required such a slope.

Table IV summarizes the mixing ratios and their gradients for a variety of gas species that have been derived from our analysis of the spectra of Crisp *et al.* (1991). This table gives the midpoint and the altitudinal width of the sensing region based on the sensitivity functions of Fig. 9 and their minimum intensity counterparts. In particular, the midpoint is based on the location of the peak sensitivity, whereas the width is found from the places where the sensitivity equals half the peak sensitivity. We now compare these results with other estimates of gas abundances, which are summarized in Table III. There is a hint in the ensemble of previous measurements that the CO mixing ratio declines by about a factor of two in the altitude region from the cloud tops (≈65 km) to 10–20 km. However, because different sets of observations need to be compared to infer a gradient, the reality of this gradient cannot be established definitively from these data alone. Our analysis, however, provides strong evidence that the CO mixing ratio declines by about a factor of 2 from 46 to 23 km. There is a sizable uncertainty in our inferred gradient of the CO mixing ratio (≈40%). Nevertheless, we have confidence in its reality in that we derived a gradient having the same sign and similar magnitude when we performed simulations with H_2O–CO_2 continuum opacity included in the opacity database.

The mixing ratio of SO_2 that we derive for the altitude region from 37 to 52 km is in good agreement, within their mutual error bars, with the values found at similar altitudes by gas chromatographs (GC) on the Pioneer Venus (PV) and Venera probes (Oyama *et al.* 1980, Gel'man *et al.* 1979), but is in conflict with the much lower value derived from analysis of UV radiation measured from the VEGA probes (Berto *et al.* 1987). Bezard *et al.* (1993) argue that the similarity in the SO_2 abundances derived from very recent nightside spectra and ones obtained a decade ago imply that there have been no sizeable fluctuations in the SO_2 content of the lower atmosphere of Venus over the past decade, in contrast to the evidence for significant variations in the SO_2 abundance near the cloud tops over this same period (Esposito *et al.* 1984).

Within their uncertainties, the mixing ratios of HCl and HF that we infer at centroid altitudes of 23.5 and 33.5 km, respectively, agree with those obtained by Bezard *et al.* (1990) from their high-resolution nightside spectra. They are similar to the values deduced near the cloud tops from analysis of very high resolution spectra of the dayside taken 25 years ago (Connes *et al.*, 1967, Young 1972). This similarity suggests that little thermochemistry of these halides is occurring in Venus' lower atmosphere. The overall abundance of these gases in the atmosphere may be controlled by buffering reactions with surface minerals (e.g., Fegley and Treiman 1992).

Our best fit H_2O profile is characterized by a constant mixing ratio of 30 ± 10 ppm from about 40 km to about 10 km. It is not possible to constrain the water vapor mixing ratio below 10 km with the spectra analyzed in this paper. These results agree with preliminary analyses of recent high-resolution spectra of the nightside by Bezard *et al.* (1991) and deBergh *et al.* (1993), who conclude that a H_2O mixing ratio of 30 ± 15 ppm provides a good fit to the 2.3-, 1.7-, and 1.18-μm windows. However, the above analyses disagree with much larger values of a few hundred parts per million at altitudes close to the top of this domain that were inferred from simulations of near-infrared spectra of the Venus day sky obtained from several Venera probes (Moroz *et al.* 1980, Young *et al.* 1984).

The spectra of the 1.2-μm window are inconsistent with the water vapor profile deduced from PV mass spectrometer measurements in the lowest 25 km of the atmosphere

by Donahue and Hodges (1992) (profile A of Fig. 18e). However, it is consistent with profile B of Fig. 18e that was obtained by scaling the original profile by 0.45 so that there is 30 ppm at altitudes above 10 km (cf., Fig. 18f). In their last reanalysis of the PV mass spectrometer data, Donahue and Hodges (1993) obtained a constant water vapor mixing ratio of about 30 ppm from the surface to 25 km when they allowed for the transfer of D from HDO to methane.

Our value of 30 ppm for the H_2O mixing ratio in the lower portion of Venus' atmosphere provides important constraints on the source of this water. In particular, it is now less likely that this water represents the last remnants of a much larger amount of water that was initially present on Venus and more likely that it is the result of a quasi-state between loss of water by photolysis and escape to space of H and its gain from degassing from the interior and impacts by volatile-rich bodies (Grinspoon 1987, 1993).

Our analysis indicates that there is a sharp increase in the OCS mixing ratio with decreasing altitude from about 39 to 26 km. This result appears to be very robust in the sense that the inclusion of H_2O–CO_2 continuum opacity caused little change to our inferred OCS profile. Over the above range of altitudes, the OCS mixing ratio increases from several 10s of ppb to almost 10 ppm. Furthermore, the rate at which the OCS mixing ratio is increasing equals within a factor of two the rate at which the CO mixing ratio is decreasing with decreasing altitude over a similar range of altitudes, i.e., the two slopes, $d\alpha/dz$, are the same within the uncertainty of their values. These results are in remarkable agreement with calculations of buffering by surface minerals (Fegley and Treiman 1992) and thermodynamic equilibrium of gases close to Venus' surface (Krasnopolsky and Parshev 1979), both of which predict a sharply increasing OCS mixing ratio toward the surface, with a surface value of several 10s of ppm. In both cases, CO acts as one of the source gases for making OCS. However, we wish to emphasize that our analysis provides no direct information on the OCS mixing ratio below an altitude of 26 km and the extrapolation of our inferred curve at higher altitudes to the surface is a risky proposition.

Bezard *et al.* (1990) first detected the presence of OCS in nightside spectra of Venus and derived an estimate of its mixing ratio under the assumption that it was constant over the sensing region. This ratio is about a factor of 100 smaller than the value of 40 ± 20 ppm inferred from gas chromatograph data taken from the Venera 13 and 14 probes for a sample collected between 29 and 37 km (Moroz 1983). Our inference of a strong vertical gradient in the OCS mixing ratio brings the results from the two data sets into closer agreement. However, the OCS abundance derived for the midpoint of our sampling region—33 km—is still a factor of 10 below the value derived from the GC data, the midpoint of whose sampling altitude is also 33 km. In addition, nowhere within the range of the GC's sampling altitudes does our inferred OCS profile fall within the error bars of the OCS mixing ratio obtained from the GC data.

The very large amounts of methane seen in the PV mass spectrometer data (Donahue and Hodges 1993) are inconsistent by several orders of magnitude with the upper bounds derived here from spectra of the 1.7- and 2.3-μm windows (cf., Fig. 15 and Table IV). Thus, the PV abundances, at least those above 20 km altitude, are not representative of typical conditions in Venus' lower atmosphere. Indeed, Donahue and Hodges (1993) are skeptical of their own results and have arrived at a similar conclusion based on the strong differences between the D/H ratio of methane and that of other H-bearing species, such as water.

7. CONCLUSIONS

Current databases of gas opacity are adequate for simulating the near-infrared emission from Venus' nightside, if one is willing to employ wavelength-independent values for the CO_2 continuum in several windows: namely, 2.3, 1.7, and 1.18 μm. The use of Wattson's high-T database for CO_2 leads to good matches to the observed spectra for the 2.3- and 1.7-μm windows, but its accuracy needs to be improved in the 1.2-μm window complex. H_2O–CO_2 continuum opacity may be important in the 2.3- and 1.7-μm windows, but a combination of laboratory measurements and further theoretical efforts are needed to obtain substantially more accurate estimates of it. Hot bands of H_2O appear to make a difference in the 1.7-μm window, but further development of a high-T database for H_2O is needed.

There are not adequate CO_2-broadening half-widths of the rovibrational lines of nonlinear, polyatomic gases, including H_2O. Unlike their linear counterparts, these half-widths depend on several quantum mechanical rotational numbers, rather than just one. However, theory is capable of making accurate predictions of these half-widths for molecules such as H_2O (R. Gamache, private communication).

There is also the issue of whether gas species other than H_2O and CO_2 provide significant opacity in the shorter wavelength regions, both from the perspective of correctly modeling the windows and from learning about the abundance of these species in the deeper regions of the atmosphere. In view of the large D/H ratio in Venus H_2O (and presumably other hydrogenated gases), it is important to determine line parameters for deuterated gases (especially HDO and DCl) in the shorter wavelength windows. Finally, there is a need to assess whether other absorbers not included in our simulations, such as H_2SO_4

and H_2CO_3 vapor, make important contributions to the opacity in the various window regions. Although the above represents a nontrivial "shopping list" of gaps and limitations in the current gas database, much progress can be made on each item over the next several years through a combination of laboratory studies and theoretical computations; i.e., there is no item that, in principle, we do not know how to address.

A certain degree of caution is needed in how literally to accept the mixing ratios of gases derived from modeling the nightside emission data, given all the work that is still needed on gas opacities, as detailed above. Nevertheless, it is still possible to make meaningful estimates of the abundances of various gas species in the lower atmosphere and even, in some cases, to evaluate the vertical gradient of the mixing ratio. The alternative calculations that we performed when the continuum opacity of H_2O–CO_2 was added to our standard opacity database provide an indication of the robustness of the mixing ratios derived from our standard opacity database alone.

The permitted transitions of water make important contributions to the opacity within portions of four window regions: 1.10, 1.18, 1.7, and 2.3 μm. As a result, it is possible to evaluate its mixing ratio from just below the main clouds all the way to the surface. However, higher spectral resolution observations, in conjunction with certain improvements in the databases, will be needed before we can definitively answer such important questions as whether or not the water vapor mixing ratio decreases toward the surface near the base of the atmosphere.

In summary, near-infrared spectra of Venus' nightside emission contain unique and valuable information about clouds and gases below the main clouds. The current state-of-the-art is such that some of this information content can be extracted now. However, further work is needed to realize the full potential of this key type of measurement.

APPENDIX A: DND THEORY

In this Appendix, we discuss the manner in which Wattson and his associates have constructed high-temperature databases for CO_2 and H_2O by using direct numerical diagonalization (DND) theory (Wattson and Rothman 1992). As in any theoretical calculation of this type, two fundamental quantities need to be determined: the potential energy function, $V(x_i)$, and the dipole moment function, $M(x_i)$, where the independent variables x_i are measures of the relative positions of the various nuclei of the molecule (Goody and Yung 1989). (The number of values of i equals the number of vibrational degrees of freedom of the molecule.) The function V provides a measure of the net electrostatic attraction among the nuclei and electrons that constitute the molecule as a function of the positions of its component nuclei. It is used to determine line positions (see below). The function M provides a measure of the strength with which a molecule can interact with electromagnetic radiation. It is used to evaluate line intensities (see below). V and M are constrained by accurate laboratory measurements of the central wavenumbers and intensities of a subset of the total number of lines of interest, respectively.

Given $V(x_i)$, the appropriate Schrödinger equation is solved to determine vibrational–rotational wavefunctions (eigenfunctions) and energy levels (eigenvalues). The line positions are then simply obtained by taking the difference of the energy levels of the final and initial states of the transition. To obtain line intensities, one first calculates dipole moment matrices by evaluating the spatial integral of the product of the wavefunction of the final state, the dipole moment function, and the wavefunction of the initial state. Finally, the line strengths are obtained by combining the dipole moment matrices with appropriate Boltzmann factors, statistical weights, and the partition function (a normalization factor for the Boltzmann factors).

Figure A1 outlines the DND technique in a flow diagram. One initially generates independent coordinate solutions by choosing a particular molecular coordinate system and suitable basis functions, which are solutions of appropriate Schrödinger equations. An analytical form is selected for the potential energy function and coordinate matrices are generated. This function is expressed in terms of the chosen molecular coordinates, whose free parameters, the potential coefficients, are determined from laboratory data (see below). Using an initial set of potential coefficients, one then constructs the multidimensional Hamiltonian matrix, energy ordering the product Hilbert spaces. The Hamiltonian matrix is diagonalized to produce eigenvalues and associated eigenvectors. In turn, the eigenvectors are used to produce a new set of potential coefficients that are constrained so that their eigenvalues represent a least squares fit to the observed energies, as defined by the observed line positions.

In a similar vein, a dipole moment matrix is constructed by using the coordinate matrices and constraining the dipolar coefficients to provide a least squares fit to the observed line intensities. A similarity transformation is applied to the dipole moment matrix with the previously calculated eigenvectors to produce the transition moment matrix. The final line positions for all transitions of interest are obtained by taking the wavenumber differences of the eigenvalues for the upper and lower energy levels and their associated intensities are found from the squares of the transition moments multiplied by Boltzmann and partition functions.

For the current high-T CO_2 database, the standard di-

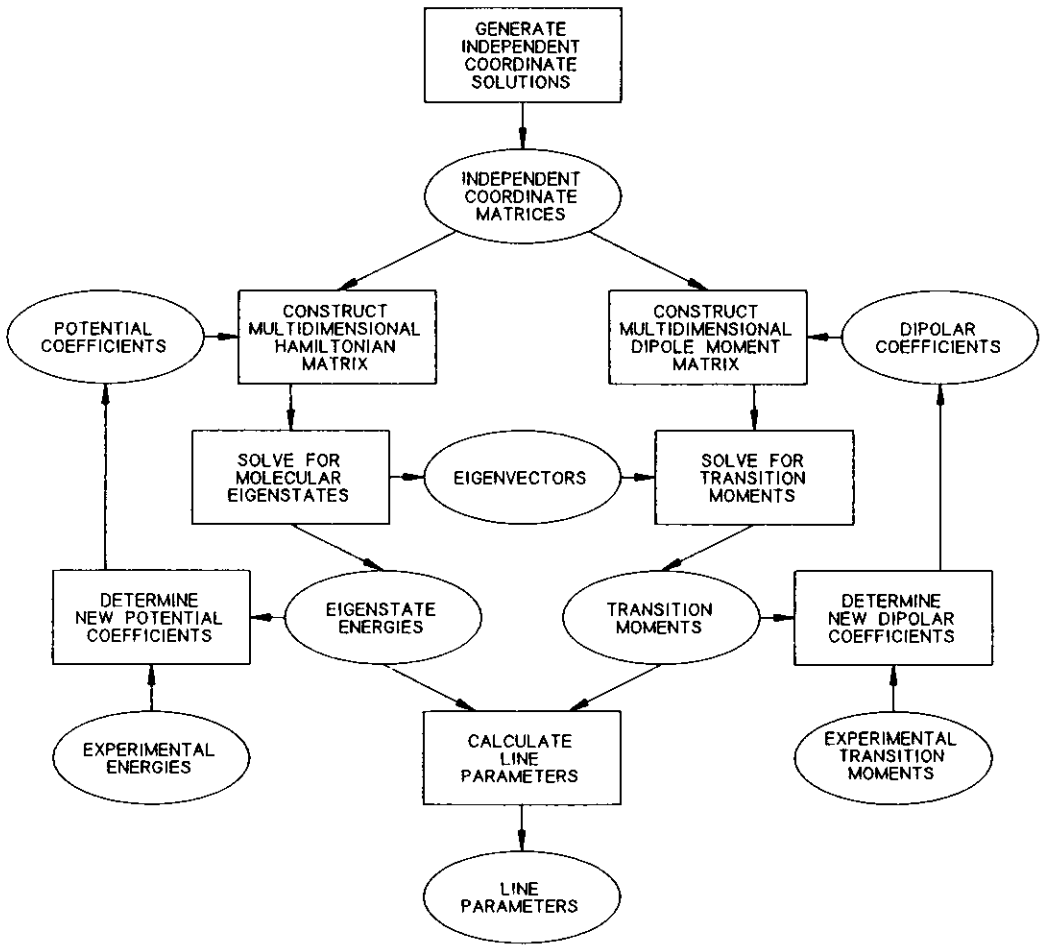

FIG. A1. Flow diagram of the direct numerical diagonalization technique used by Wattson and Rothman (1992) to construct the high-T database for CO_2.

mensionless normal coordinate system was used to represent the three vibrational modes. (In this system, a rectangular coordinate system is used, with the coordinates representing orthogonal displacements of the C and O nuclei from the linear equilibrium configuration of the molecule.) The basis functions were obtained from solutions to the harmonic oscillator-rigid rotor problem; the potential function was expressed as a multidimensional power series expansion in normal coordinates; and the Hamiltonian included operators for vibration, rotation, and Coriolis interactions. (The Coriolis operator was not included in the previous study of Wattson and Rothman (1986).)

Due to limitations on computer time, individual numerical diagonalizations were performed only at four rotational quantum numbers: J = 0, 60, 120, and 180. These results were interpolated to other J quantum numbers. This compromise may represent a major limitation on the accuracy of the high-T database for CO_2. With the availability of much more powerful computers at AFGL than were present at the time the current database was assembled, it will be possible to perform diagonalizations at all J of interest. It is hoped that this will be done in the near future.

In constructing the preliminary high-T database for H_2O, valence coordinates were used (coordinates aligned with the bonds between atoms of the molecule). Unbounded Morse functions for the vibrational stretch basis allowed calculations of continuum states and Jacobi polynomials for the vibrational bend basis alleviated the need for prediagonalization. The rotational eigenstate calculation included Coriolis terms as well as diagonal and off-diagonal asymmetric, pure rotator terms. Finally, *ab initio* calculations were employed to define dipole moment derivatives. However, these derivatives were adjusted so that Q1 lines with frequencies below 10,000 cm^{-1} had intensities that were reasonably close to their counterparts on the HITRAN database.

APPENDIX B: QUANTUM THEORY FOR DIATOMIC MOLECULES

Here, we describe briefly the way in which Tipping (1990) calculated a high-temperature database for the hydrogen halides and CO by using quantum mechanical theory for diatomic molecules. The primary theoretical quantities are the Dunham parameters, Y_{kl}, and the dipole–moment function parameters. The Dunham parameters relate the vibrational and rotational quantum numbers, v and J, respectively, to the vibration–rotational energy levels, E_{vJ}, according to the following equation:

$$E_{vJ} = \sum_{k,l} Y_{kl}(v + 1/2)^k(J(J + 1))^l. \quad (7)$$

The Dunham parameters were found by fitting experimental frequency data. The transition frequencies were obtained by differencing the energy levels given by the above equation.

The Dunham parameters were also used to compute an accurate potential-energy function, $V(r)$, as a function of internuclear distance r (Tipping 1990). The dipole moment function was expressed in terms of a Pade approximant, which was chosen to have correct asymptotic dependence on r, i.e., at both the dissociation and equilibrium positions (Ogilvie *et al.* 1980). Therefore, it could be used for high-J lines, high overtones, and hot bands, even though it was constrained by laboratory data having lower energy levels. Line strengths were then found in the manner outlined in Appendix A.

APPENDIX C: WATER VAPOR CONTINUUM

Here, we describe the basic assumptions used to calculate H_2O continuum opacity due to the far wings of pressure-broadened lines, the computational protocol, and the parameters chosen for these calculations. A much more detailed discussion is contained in Ma and Tipping (1991,1992a,b). We are interested in determining the opacity resulting from both H_2O and CO_2 broadening for application to the Venus atmosphere. We denote these two types of opacity as H_2O–H_2O and H_2O–CO_2 opacities.

Formulae for calculating the shapes of rotational lines can be obtained readily for two limiting cases of the durations of collisions between pairs of molecules. On the one hand, the collision may be considered to be instantaneous (the "impact" approximation). This approximation is valid close to the line center and results in the Lorentz line shape for pressure-broadened lines. On the other hand, the duration may be assumed to be infinite (the "quasi-static" approximation). This assumption is valid in the far wings of lines and is the one used for calculating the H_2O continuum opacity. The boundary between these two regimes occurs at the point where $\delta\nu = 1/\tau$, where $\delta\nu$ is the difference between the frequency of interest and the frequency of the line center and τ is the duration of the collision. For most molecules $\tau \simeq 10^{-12}$ sec and, hence, the transition between these two regimes occurs at several 10s of wavenumbers from the line center.

Ma and Tipping (1991) also assumed that the frequencies of interest differ from those at the centers of the strong rotational lines that produce the continuum by amounts that are large compared to the differences in central frequencies among lines that are strongly coupled by the interaction of the two colliding molecules. This approximation is well met within the window regions of the Venus atmosphere.

A third approximation is that no collisions of complexity higher than binary need be considered. The laboratory experiments of Burch (1969) suggest that this binary collision approximation is valid to densities in excess of 10 amagat and thus should be appropriate for essentially the entire Venus atmosphere, although it may start to break down at altitudes very close to the surface.

Finally, Ma and Tipping (1991) adopted Rosenkranz's (1985, 1987) boxcar approximation. States with total angular momentum quantum numbers, $J \leq J_{max}$ are assumed to be equally populated, whereas states having higher J are assumed to be completely unoccupied. Although this approximation, at first glance, might seem to be a very crude one, in reality it is good so long as rotational lines belonging to a given band lie much closer to one another than $\delta\nu$. Numerical experiments in which J_{max} was varied show that this approximation does not substantially degrade the accuracy of the calculations. For the calculations used in this paper, J_{max} was set equal to 4 and 12 for the states of the water and carbon dioxide molecules, respectively.

Using the above approximations, Ma and Tipping (1991) expressed the spectral line shape in the far wings of pressure-broadened water lines in terms of the ensemble average of the resolvent operator (an inverse operator), whose denominator contains the interaction Hamiltonian. In evaluating this ensemble average, they assigned a statistical weight, $\rho(r)$ to the pair of colliding molecules being separated by a distance r that was given by

$$\rho(r) = e^{-V(r)/kT}/U, \quad (8)$$

where V is the interaction potential energy between the absorbing and colliding molecule, k is Boltzmann's constant, T is temperature, and U is a normalization factor. As mentioned in the main text, Ma and Tipping (1991) obtained values for the H_2O–H_2O continuum in the 300–1100-cm^{-1} region that agreed quite well with the laboratory measurements of Burch and Gryvnak (1979).

In applying this theory developed for the rotational band of H_2O to its vibrational bands at higher wavenumbers, Ma and Tipping (1992a,b) assumed that the total absorption coefficient could be expressed as the superposition of components resulting separately from each vibrational band and that a common band-independent lineshape function could be used. The former assumption is in good accord with the matrix elements of the dipole moment between different vibrational states of H_2O being much less than those between the same vibrational states. The latter assumption is consistent with the matrix elements between the same vibrational states depending only weakly on the vibrational quantum numbers. Since the line shape function is common for all bands and since the above approximations should be good ones, we suspect that the accuracy of the continuum calculations at the high wavenumbers of interest to this paper is not much worse than the accuracy of those carried out in the 300–1100-cm^{-1} region. However, it is essential that laboratory measurements be made of the H_2O–CO_2 continuum that occurs in window regions adjacent to strong H_2O bands to provide a check on the theory and to permit refinements to be made if necessary.

For calculating the H_2O–H_2O self-broadening continuum absorption, the interaction potential was written as the sum of an anisotropic component and an isotropic component (Ma and Tipping, 1992a). The anisotropic component was approximated by the leading dipole–dipole potential, whereas the isotropic part was approximated by a simple Lennard–Jones type model:

$$V_{iso}(r) = C\sigma^{-6}[(\sigma/r)^s + (\sigma/r)^6]. \quad (9)$$

For the calculations shown in this paper, the following parameters were used for the H_2O–H_2O continuum: the magnitude of the dipole moment of H_2O = 1.8546 Debye, $C/k = 8 \times 10^5$ Å^6 K, $s = 48$, and $\sigma = 3.13$ Å (Rosenkranz 1985, 1987).

In the case of the H_2O–CO_2 foreign broadening continuum, the anisotropic interaction was represented by the leading dipole–quadrupole potential, while a Lennard–Jones model was used to describe the isotropic part (Ma and Tipping 1992b). The following input parameters were used to evaluate this continuum: the magnitude of the quadrupole moment of CO_2 = 4.3 Debye Å (P. Varanasi, private communication), $C/k = 10.434 \times 10^5$ Å^6 K, $s = 12$, and $\sigma = 3.57$ Å (Rosenmann *et al.* 1988).

ACKNOWLEDGMENTS

We are very grateful to Brad Sitton for preparing the final versions of almost all the figures and for participating in the simulations of the impact of methane on the spectra. This work was supported by NASA's Planetary Atmospheres Program.

REFERENCES

ALLEN, D. A. 1987. The dark side of Venus. *Icarus* **69,** 221–229.

ALLEN, D. A. 1992. Venus. *IAU Circular* 4962.

ALLEN, D. A., AND J. W. CRAWFORD 1984. Cloud structure on the dark side of Venus. *Nature* **307,** 222–224.

ALLEN, D. A., D. CRISP, AND V. S. MEADOWS 1992. Variable oxygen air glow on Venus: A probe of atmospheric dynamics. *Nature* **359,** 516–519.

BAILEY, J., J. R. BARTON, P. CONROY, H. DAVIES, D. J. HILLIER, A. R. HYLAND, T. J. JONES, K. SHORTRIDGE, AND D. WHITTARD 1988. *Publ. Astron. Soc. Pac.* **100,** 1178–1185.

BELL, J. F. III, D. CRISP, P. G. LUCY, T. A. OZOROWSKI, W. M. SINTON, S. C. WILLIS, AND B. A. CAMPBELL 1991. Spectroscopic observations of bright and dark emission features on the night side of Venus. *Science* **252,** 1293–1296.

BERTO, ZH. L., A. P. EKONOMOV, B. MEZH, V. I. MOROZ, A. ABERZHAL', V. I. GNEDYKH, A. V. GRIGOR'EV, B. E. MOSHKIN, A. OSHKORN, ZH. P. POMMERO, AND S. B. SERGEEVA 1987. Study of the absorption of ultraviolet radiation in the atmosphere of Venus on the descending spacecraft Vega-1 and Vega-2. *Cosmic Res.* **25,** 528–541.

BEZARD, B., C. DE BERGH, D. CRISP, AND J.-P. MAILLARD 1990. The deep atmosphere of Venus revealed by high-resolution night-side spectra. *Nature* **345,** 508–511.

BEZARD, B., C. DEBERGH, J.-P. MAILLARD, D. CRISP, J. POLLACK, AND D. GRINSPOON 1991. High-resolution spectroscopy of Venus' nightside in the 2.3, 1.7, and 1.1–1.3 μm windows. *Bull. Am. Astron. Soc.* **23,** 1192.

BEZARD, B., C. DEBERGH, B. FEGLEY, J.-P. MAILLARD, D. CRISP, T. OWEN, J. POLLACK, AND D. GRINSPOON 1993. The abundance of sulfur dioxide below the clouds of Venus. *Geophys. Res. Lett.*, in press.

BRODBECK, C., NGUYEN-VAN-THANH, J.-P. BOUANICH, C. BOULET, A. JEAN-LOUIS, B., BEZARD, AND C. DE BERGH 1991. Measurements of pure CO_2 absorption at high densities near 2.3 μm. *J. Geophys. Res.* **96,** 17497–17500.

BURCH, D. E., AND D. A. GRYVNAK 1978. *Infrared Absorption by CO_2 and H_2O.* Report No. AFGL-TR-79-0054.

BURCH, D. E., D. A. GRYVNAK, R. R. PATTY, AND C. E. BARTKY (1969). Absorption of infrared radiant energy by CO_2 and H_2O. IV. Shapes of collision broadened lines. *J. Opt. Soc. Am.* **59,** 267–280.

CARLSON, R. W., K. H. BAINES, TH. ENCRENAZ, F. W. TAYLOR, P. DROSSART, L. W. KAMP, J. B. POLLACK, E. LELLOUCH, A. D. COLLARD, S. B. CALCUTT, D. GRINSPOON, P. R. WEISSMAN, W. D. SMYTHE, A. C. OCAMPO, G. E. DANIELSON, F. P. FANALE, T. V. JOHNSON, H. H. KIEFFER, D. L. MATSON, T. B. MCCORD, AND L. A. SODERBLOM 1991. Galileo infrared imaging spectroscopy measurements at Venus. *Science* **253,** 1541–1548.

CLANCY, R. T., AND D. O. MUHLEMAN 1985. Diurnal variations in the Venus mesosphere from CO microwave spectra. *Icarus* **64,** 157–182.

CLOUGH, S. A., F. X. KNEIZYS, E. P. SHETTLE, AND G. P. ANDERSON 1986. Atmospheric radiance and transmission: FASCOD2. *Sixth Conference on Atmospheric Radiation,* pp. 141–144. American Meteorological Society, Boston.

CONNES, P., J. CONNES, W. S. BENEDICT, AND L. D. KAPLAN 1967. Traces of HCl and HF in the atmosphere of Venus. *Astrophys. J.* **147,** 1230–1237.

CONNES, P., J. CONNES, L. D. KAPLAN, AND W. S. BENEDIT 1968. Carbon monoxide in the Venus atmosphere. *Astrophys. J.* **152,** 731–743.

CRISP, D. 1986. Radiative forcing of the Venus mesosphere. I. Solar fluxes and heating rates. *Icarus* **67,** 484–514.

CRISP, D., *et al.* 1989. The nature of the near-infrared features on the Venus night side. *Science* **246,** 506–509.

CRISP, D., D. A. ALLEN, D. H. GRINSPOON, AND J. B. POLLACK 1991a. The dark side of Venus: Near-infrared images and spectra from the Anglo-Australian Observatory. *Science* **253,** 1263–1266.

CRISP, D., S. MCMULDROCH, S. K. STEPHENS, W. M. SINTON, B. RAGENT, K.-W. HODAPP, R. G. PROBST, L. R. DOYLE, D. A. ALLEN, AND J. ELIAS 1991b. Ground based near-infrared observations of Venus during the Galileo encounter. *Science* **253,** 1538–1541.

DE BERGH, C., B. BEZARD, T. OWEN, D. CRISP, J.-P. MAILLARD, AND B. L. LUTZ 1991. Deuterium on Venus: observations from Earth. *Science* **251,** 547–549.

DE BERGH, C., B. BEZARD, D. CRISP, J.-P. MAILLARD, T. OWEN, J. POLLACK, AND D. GRINSPOON 1993. The H_2O abundance in the deep atmosphere of Venus from near-infrared spectroscopy of the night side. *Adv. Space Res.*, in press.

DONAHUE, T. M., AND R. R. HODGES, JR. 1993. Venus methane and hydrogen. *Geophys. Res. Lett.*, in press.

DONAHUE, T. M., AND R. R. HODGES, JR. 1992. The past and present water budget of Venus. *J. Geophys. Res. Planets* **97,** 6083–6092.

DONAHUE, T. M., J. H. HOFFMAN, R. R. HODGES, JR., AND A. J. WATSON 1982. Venus was wet: A measurement of the ratio of deuterium to hydrogen. *Science* **216,** 630–633.

ELSASSER, W. M. 1938. Far infrared absorption of atmospheric water vapor. *Astrophys. J.* **87,** 497–507.

ESPLIN, M. P., R. B. WATTSON, M. L. HOKE, R. L. HAWKINS, AND L. S. ROTHMAN 1989. Observation and calculation of carbon dioxide bands with high vibrational angular momentum. *Appl. Opt.* **28,** 409–410.

ESPOSITO, L. W. 1984. Sulfur dioxide: Episodic injection shows evidence for active Venus volcanism. *Science* **223,** 1072–1074.

ESPOSITO, L. W., R. KNOLLENBERG, M. MAROV, O. TOON, AND R. TURCO 1983. The clouds and hazes of Venus. In *Venus* (D. M. Hunten, L. Colin, T. M. Donahue, and V. I. Moroz, Eds.), pp. 484–564. Univ. of Arizona Press, Tucson.

FAYT, A. 1970. Spectres infrarouges de l'oxysulfure de carbone entre 2400 et 7000 cm^{-1}. *Ann. Soc. Sci. Bruxelles* **84**(I) 69–106.

FAYT, A., R. VANDENHAUTE, AND J. G. LAHAYE 1986. Global rovibrational analysis of carbonyl sulfide. *J. Mol. Spectrosc.* **119,** 233–266.

FEGLEY, B., JR., AND A. H. TREIMAN 1992. Chemistry of atmosphere–surface interactions on Venus and Mars. In *Venus and Mars: Atmospheres, Ionospheres, and Solar Wind Interaction* (J. Luhnmann and R. O. Pepin, Eds.), AGU Chapman Conference volume, pp. 7–71.

GEL'MAN, B. G., V. G. ZOLOTUKHIN, N. I. LAMONOV, B. V. LEVCHUK, A. N. LIPATOV, L.M., MUKHIN, D. F. NENAROKOV, V. A. ROTIN, AND B. P. OKHOTNIKOV 1979. Analysis of chemical composition of Venus atmosphere by gas chromatography on Venera 12. *Cosmic Res.* **17,** 585–589.

GIVER, L. P., AND C. CHACKERIAN JR. 1991a. Rovibrational intensities for the $(31^10)_{IV}$–(00^00) band of $^{12}C^{16}O_2$ at 4416 cm^{-1}. *J. Mol. Spectrosc.* **148,** 80–85.

GIVER, L. P., AND C. CHACKERIAN, JR. 1991b. *Intensity and position measurements of carbon dioxide lines in the 4370 to 4640 cm^{-1} region.* 46th International Symposium on Molecular Spectroscopy, Columbus, OH.

GOODY, R. M., AND Y. L. YUNG 1989. *Atmospheric Radiation: Theoretical Basis.* Oxford Univ. Press, NY.

GRINSPOON, D. 1987. Was Venus wet: Deuterium reconsidered. *Science* **238,** 1702–1704.

GRINSPOON, D. H. 1993. Evolutionary implications of a steady state water abundance on Venus. *Nature,* in press.

GRINSPOON, D. H., AND J. S. LEWIS 1988. Cometary water on Venus: Implications of stochastic impacts. *Icarus* **74,** 21–35.

HANSEN, J. E., AND L. D. TRAVIS 1974. Light scattering in planetary atmospheres. *Space Sci. Rev.* **16,** 527–610.

HOWARD, T. N., D. E. BURCH, AND D. WILLIAMS 1956. Infrared transmission of synthetic atmospheres. *J. Opt. Soc. Am.* **46,** 186–190, 237–245, 334–338, 452–455.

KAGANN, R. H. 1982. Infrared absorption intensities for OCS. *J. Mol. Spectros.* **94,** 192–198.

KAMP, L. W., AND F. W. TAYLOR 1990. Radiative-transfer models of the night side of Venus. *Icarus* **86,** 510–529.

KAMP, L. W., F. W. TAYLOR, AND S. B. CALCUTT 1988. Structure of Venus' atmosphere from modeling of night-side infrared spectra. *Nature* **336,** 360–362.

KAWABATA, K. D., D. L. COFFEEN, J. E. HANSEN, W. A. LANE, M. SATO, AND L. D. TRAVIS 1980. Cloud and haze properties from Pioneer Venus polarimetry. *J. Geophys. Res.* **85,** 8129–8140.

KNOLLENBERG, R. G., AND D. M. HUNTEN 1980. The microphysics of the clouds of Venus: Results of the Pioneer Venus particle size spectrometer experiment. *J. Geophys. Res.* **85,** 8039–8058.

KRASNOPOLSKY, V. A., AND V. A. PARSHEV 1979. Chemical composition of Venus' troposphere and cloud layer based on Venera 11, Venera 12, and Pioneer-Venus measurements. *Cosmic Res.* **17,** 630–637.

LAFFERTY, W. J., G. T. FRASER, A. S. PINE, J.-M. FLAUD, C. CAMY-PEYRET, V. DANA, J.-Y. MANDIN, A. BARBE, J. J. PLATEAUX, AND S. BOUAZZA 1992. The 3-ν_3 band of $^{32}S^{16}O_2$: Line positions and intensities. *J. Mol. Spectr.* **154,** 51–60.

LEVY, A., N. LACOME, AND C. CHACKERIAN, JR. 1992. Collisional line mixing. In *Spectroscopy of the Earth's Atmosphere and Interstellar Molecules* (K. Narahari Rao and A. Weber, Eds.), Chapter V. Academic Press, NY.

LEWIS, J. S., AND D. H. GRINSPOON 1990. Vertical distribution of water in the atmosphere of Venus: A simple thermochemical explanation. *Science* **249,** 1273–1275.

MA, Q., AND R. H. TIPPING 1990. The atmospheric water continuum in the infrared: Extension of the statistical theory of Rosenkranz. *J. Chem. Phys.* **93,** 7066–7075.

MA, Q., AND R. H. TIPPING 1991. A far wing line shape theory and its application to the water continuum absorption in the infrared region I. *J. Chem. Phys.* **95,** 6290–6301.

MA, Q., AND R. H. TIPPING 1992a. A far wing line shape theory and its application to the water vibrational bands II. *J. Chem. Phys.* **96,** 8655–8663.

MA, Q., AND R. H. TIPPING 1992b. A far wing line shape theory and its application to the foreign-broadened water continuum absorption. III. *J. Chem. Phys.* **97,** in press.

MAROV, M. YA, V. P. VOLKOV, YU. A SURKOV, AND M. L. RYVKIN 1989. Lower atmosphere. In *Venus, Atmosphere, Surface, Interior Structure* (V. L. Barsukov and V. P. Volkov, Eds.), pp. 25–67, Nauka, Moscow.

MOORE, J. F. (1971). *Infrared Absorption of Carbon Dioxide at High Densities with Application to the Atmosphere of Venus.* Ph.D. thesis, Goddard Institute for Space Studies, Columbia University.

MOROZ, V. K. 1983. Summary of preliminary results of the Venera 13 and Venera 14 missions. In *Venus* (D. M. Hunten, L. Colin, T. M. Donahue, and V. I. Moroz, Eds.), pp. 45–68. Univ. Arizona Press, Tucson.

MOROZ, V. I., N. A. PARFENT'EV, AND N. F. SAN'KO 1979. Spectrophotomeric experiment on the Venera 11 and 12 descent modules. 2. Analysis of Venera 11 spectra by layer-addition method. *Cosmic Res.* **17,** 601–614.

MOROZ, V. I., YU. M. GOLOVIN, A. P. EKONOMOV, B. E. MOSHKIN, N. A. PARFENT'EV, AND N. F. SAN'KO 1980. Spectrum of the Venus day sky. *Nature* **284,** 243–244.

MOSKALENKO, N. I., YU. A. IL'IN, S. N. PARZHIN, AND L. V. RODINOVON 1979. Pressure-induced IR radiation absorption in atmospheres. *Bull. Acad. Sci. USSR, Atmos. Oceanic Phys.* **15,** 632–637.

NAKAZAWA, T., AND M. TANAKA 1982. Intensities, half-widths and shapes of spectral lines in the fundamental band of CO at low temperatures. *J. Quant. Spectrosc. Rad. Transfer* **28,** 471–480.

OGILVIE, J. F., W. R. RODWELL, AND R. H. TIPPING 1980. Dipole moment functions of the hydrogen halides. *J. Chem. Phys.* **73,** 5221–5229.

OYAMA, V. I., G. C. CARLE, F. WOELLER, J. B. POLLACK, R. T. REYNOLDS, AND R. A. CRAIG 1980. Pioneer Venus gas chromatography of the lower atmosphere of Venus. *J. Geophys. Res.* **85,** 7891–7902.

PALMER, K. F., AND D. WILLIAMS 1975. Optical constants of sulfuric acid: application to the clouds of Venus? *Appl. Opt.* **14,** 208–219.

POLLACK, J. B., D. W . STRECKER, F. C. WITTEBORN, E. F. ERICKSON, AND B. J. BALDWIN 1978. Properties of the clouds of Venus, as inferred from airborne observations of its near-infrared reflectivity spectrum. *Icarus* **34,** 28–45.

POLLACK, J. B., O. B. TOON, R. C. WHITTEN, R. BOESE, B. RAGENT, M. TOMASKO, L. ESPOSITO, L. TRAVIS, AND D. WIEDMAN 1980. Distribution and source of the UV absorption in Venus' atmosphere. *J. Geophys. Res.* **85,** 8141–8150.

ROSENKRANZ, P. W. 1985. Pressure broadening of rotational bands I. A statistical theory. *J. Chem. Phys.* **83,** 6139–6144.

ROSENKRANZ, P. W. 1987. Pressure broadening of rotational bands. II. Water vapor from 300 to 1100 cm^{-1}. *J. Chem. Phys.* **87,** 163–170.

ROSENMANN, L., M. Y. PERRIN, J. M. HARTMANN, AND J. TAINE 1988. Diode-laser measurements and calculations of CO_2-line broadening by H_2O from 416 to 805 K and by N_2 from 296 to 803 K. *J. Quant. Spectrosc. Rad. Transfer* **40,** 569–576.

ROTHMAN, L. S. 1986. Infrared energy levels and intensities of carbon dioxide. *Appl. Opt.* **25,** 1795.

ROTHMAN, L. S., R. R. GAMACHE, A. GOLDMAN, L. R. BROWN, R. A. TOTH, H. M. PICKETT, R. L. POYNTER, J.-M. FLAUD, C. CAMY-PEYRET, A. BARBE, N. HUSSON, C. P. RINSLAND, AND M. A. H. SMITH 1987. The HITRAN database: 1986 Edition. *Appl. Opt.* **26,** 4058–4097.

ROTHMAN, L. S., *et al.* 1992. The HITRAN database: Editions of 1991 and 1992. *J. Quant. Spectrosc. Rad. Transfer* **48,** 469–507.

SEIFF, A. 1983. Thermal structure of the atmosphere of Venus. In *Venus* (D. M. Hunten, L. Colin, T. M. Donahue, and V. I. Moroz, Eds.), pp. 215–279. Univ. Arizona Press, Tucson.

SEIFF, A., J. T. SCHOFIELD, A. J. KLIORE, F. W. TAYLOR, S. S. LIMAYE, H. E. RIVERCOMB, L. A. SROMOVSKY, V. V. KERZHANOVICH, V. I. MOROZ, AND M. YA. MAROV 1986. Models of the structure of the atmosphere of Venus from the surface to 100 kilometer altitude. In *The Venus International Reference Atmosphere* (A. J. Kliore, V. I. Moroz, and G. M. Keating, Eds.), pp. 3–58. Pergamon Journals, Oxford.

SHAW, B. M., AND R. J. LOVELL 1969. Foreign gas broadening of HF by CO_2. *J. Opt. Soc. Am.* **59,** 1598–1601.

TIPPING, R. H. 1990. *Calculation of the Spectroscopic Parameters for Diatomic Molecules of Atmospheric Interest.* Air Force Geophysical Laboratory Report GL-TR-90-0127.

TOMASKO, M. 1983. Thermal balance of the lower atmosphere of Venus. In *Venus* (D. M. Hunten, L. Colin, T. M. Donahue, and V. I. Moroz, Eds.), pp. 604–631. Univ. Arizona Press, Tucson.

TOON, O. B., C. P. MCKAY, C. P. ACKERMAN, AND K. SANTHANAM 1989. Rapid calculations of radiative heating rates and photodissociation rates in inhomogeneous, multiple scattering atmospheres. *J. Geophys. Res.* **94,** 16,287–16,301.

TOTH, R. A., AND L. A. DARNTON 1974. Linewidths of HCl broadened by CO_2 and N_2 and CO broadened by CO_2. *J. Mol. Spectrosc.* **49,** 100–105.

VON ZAHN, U., S., KUMAR, H. NIEMANN, AND R. PRINN 1983. Composition of the Venus atmosphere. *In Venus* (D. M. Hunten, L. Colin, T. M. Donahue, and V. I. Moroz, Eds.), pp. 299–430. Univ. Arizona Press, Tucson.

WATSON, J. K. G. 1967. The determination of the centrifugal distortion coefficients of asymmetric top molecules. *J. Chem. Phys.* **46,** 1935–1949.

WATTSON, R. B., AND L. S. ROTHMAN 1986. Determination of vibrational energy levels and parallel band intensities of $^{12}C^{16}O_2$ by direct numerical diagonalization. *J. Mol. Spectrosc.* **119,** 83–100.

WATTSON, R. B., AND L. S. ROTHMAN 1992. Direct numerical diagonalization: Wave of the future. *J. Quant. Spectrosc. Rad. Transfer* **48,** 763–780.

YOUNG, A. T. 1973. Are the clouds of Venus made of sulfuric acid? *Icarus* **18,** 564–582.

YOUNG, L. D. G. 1972. High resolution spectra of Venus—a review. *Icarus* **17,** 632–658.

YOUNG, L. D. G., A. T. YOUNG, AND L. V. ZASOVA 1984. A new interpretation of the Venera 11 spectra of Venus. *Icarus* **60,** 138–151.